Efficient high energy laser-driven multicycle terahertz generation for accelerators

Dissertation

zur Erlangung des Doktorgrades des Fachbereichs Physik
der Universität Hamburg

vorgelegt von

Halil Tarik Olgun

Hamburg
2020

GUTACHTER DER DISSERTATION:
Prof. Franz X. Kärtner
Dr. Nicholas H. Matlis

ZUSAMMENSETZUNG DER PRÜFUNGSKOMMISSION:
Prof. Franz X. Kärtner
Dr. Nicholas H. Matlis
Prof. Dr. Daniela Pfannkuche
Jun. Prof. Dr. Ulrike Frühling
Dr. Mark J. Prandolini

DATUM DER DISPUTATION:
18. December 2020

VORSITZENDER DER PRÜFUNGSKOMMISSION:
Prof. Dr. Daniela Pfannkuche

VORSITZENDER DES PROMOTIONSAUSSCHUSSES:
Prof. Dr. Wolfgang Hansen

DEKAN DER FAKULTÄT FÜR MATHEMATIK, INFORMATIK UND NATURWISSENSCHAFTEN:
Prof. Dr. Heinrich Graener

DECLARATION

Ich versichere hiermit, dass ich die vorliegende Arbeit selbständig verfasst und keine anderen als die im Literaturverzeichnis angegebenen Quellen benutzt habe.

Alle Stellen, die wörtlich oder sinngemäß aus veröffentlichten oder noch nicht veröffentlichten Quellen entnommen sind, sind als solche kenntlich gemacht.

Die Zeichnungen oder Abbildungen in dieser Arbeit sind von mir selbst erstellt worden oder mit einem entsprechenden Quellennachweis versehen.

Diese Arbeit ist in gleicher oder ähnlicher Form noch bei keiner anderen Prüfungsbehörde eingereicht worden.

Hamburg, 18. December 2020

Halil Tarik Olgun

ABSTRACT

Optically generated, narrowband multi-cycle terahertz (MC-THz) radiation has the potential to revolutionize electron acceleration, X-ray free-electron lasers, advanced electron beam diagnostics and related research areas. However, the currently demonstrated THz generation efficiencies are too low to reach the requirements for many of these applications.

In this project, a MC-THz generation approach via difference frequency generation (DFG) driven by a laser with a multi-line optical spectrum was investigated with the aim of increasing the conversion efficiency. For this purpose, a home-built, Yb-based laser source with a multi-line optical spectrum was developed. This laser source was amplified to tens-of-millijoule using a regenerative and a four-pass amplifier; it was used to generate MC-THz in magnesiumoxid-doped periodically poled lithium niobate (MgO:PPLN) and rubidium-doped periodically poled potassium titanyl phosphate (Rb:PPKTP). With this laser system, the highest optical-to-THz conversion efficiencies (CE) of 0.49% with a pulse energy of 30 μJ at 0.29 THz, and 0.89% with a pulse energy of 45 μJ at 0.53 THz in MgO:PPLN were achieved. These results compare well with 2-dimensional numerical simulations. In addition, Rb:PPKTP, which has a promising figure-of-merit compared to MgO:PPLN, achieved a CE of 0.16% with a pulse energy of 3 μJ at 0.5 THz. Next, to scale this laser system to tens of millijoule MC-THz output, large aperture crystals for both MgO:PPLN and Rb:PPKTP were investigated using a commercial laser, producing 200 mJ with a pulse duration of 500 fs at 1030 nm; although in this case an older method of optical rectification (OR) was used, achieving less efficiency than the multi-line source. With MgO:PPLN crystals of aperture size $10 \times 15\,\mathrm{mm}^2$, a CE of 0.29% at 0.35 THz was achieved with a pulse energy of 260 μJ. This is the highest known CE value using OR. In addition, wafer-stacks with alternating crystal-axis orientation of aperture size of 1″ for LN and $10 \times 10\,\mathrm{mm}^2$ for KTP were successfully tested. Two novel experiments were performed with LN wafers: multi-stage wafer-stacks in a serial configuration with multi-output THz radiation and back-reflected seeded MC-THz generation. Both methods improved the efficiency of the MC-THz generation, compared to a single stack. In particular, for the back-reflected seeded MC-THz generation, pulse energies of 280 μJ with a CE of 0.29% was achieved; thus demonstrating the potential of seeded MC-THz generation. These achievements are an important step for the realization of next-generation, THz-driven electron accelerators.

ZUSAMMENFASSUNG

Optisch erzeugte Multi-Cycle-Terahertz-Strahlung (MC-THz) hat das Potenzial, konventionelle Elektronenbeschleuniger und damit verbundene Forschungsgebiete zu revolutionieren. Bisherige Umwandlungseffizienzen von optischer zu THz-Strahlung sind derzeit zu niedrig, um ausreichend hohe Feldgradienten zur Beschleunigung von Elektronen auf hohe Energien zu erreichen.

In dieser Arbeit wurde die MC-THz-Erzeugung durch Differenzfrequenzerzeugung (DFG) in Magnesiumoxid-dotiertem, periodisch gepolten Lithiumniobat (MgO:PPLN) und Rubidium-dotiertem, periodisch gepolten Kaliumtitanylphosphat(Rb:PPKTP) mittels eines Yb-basierten, speziell entwickelten Multilinienlasers untersucht. Dieser Ansatz erweist sich als vielversprechend, denn es konnte eine Steigerung der Konversionseffizienz auf 0,49% mit einer Pulsenergie von 30 µJ bei 0,29 THz und 0,89% mit einer Pulsenergie von 45 µJ bei 0,53 THz in MgO:PPLN sowie 0,16% mit einer Pulsenergie von 3 µJ bei 0,5 THz in Rb:PPKTP nachgewiesen werden. Diese Werte stellen die zum heutigen Stand höchsten je gemessenen Werte dar. Die Ergebnisse sind in sehr guter Übereinstimmung mit zweidimensionalen numerischen Simulationen. Desweiteren wurden Skalierungsexperimente mit einem kommerziellen Yb-basierten Laser (200 mJ, 500 fs, 50 Hz) durchgeführt. Eine Effizienz von 0,29% mit Pulsenergien von 260 µJ bei 0,35 THz in MgO:PPLN-Kristallen mit großer Apertur ($10\times15\,\mathrm{mm}^2$) konnte demonstriert werden, obwohl dabei eine bekannterweise weniger effiziente THz-Erzeugungsmethode, die optische Gleichrichtung, benutzt wurde. Dies ist die höchste nachgewiesene Effizienz basierend auf optischer Gleichrichtung für MC-THz Strahlung. Darüber hinaus wurde die periodische Polung des nichtlinearen Mediums auch über ein Wafer-Konzept erfolgreich realisiert. Dadurch war es möglich KTP- und LN-Wafer mit Aperturgrößen von 1″ und $10\times15\,\mathrm{mm}^2$ zu verwenden, um so die Pumpenergie im Vergleich zu herkömmlichen Kristallen hoch zu skalieren. Dabei wurden zwei Methoden für die effiziente Benutzung des Pumplasers untersucht: Einerseits wurden Wafer-Stapel hintereinander gereiht und vermessen, andererseits eine Methode zur geseedeten MC-THz-Erzeugung über einen rückreflektierten THz-Strahl getestet. In beiden Fällen konnte eine erhöhte Effizienz beobachtet werden. Besonders im zweiten Fall konnte eine Effizienz von 0,29% mit einer Pulsenergie von 280 µJ bei 0,16 THz erreicht werden, dreimal mehr als im Vergleich zum ungeseedeten Fall. Diese Ergebnisse sind entscheidend für die Realisierung kompakter, auf THz-Strahlung basierender Elektronenbeschleuniger der nächsten Generation.

Bizim elleden neyimiz eksik?

— Hulusi Dönmez (Dedem)

ACKNOWLEDGMENTS

I remember one winter from my childhood, when it was snowing in my small village and I had a lot of fun playing in the snow. Next year, my mother decided to send me to school although I wasn't yet at school-age. She somehow convinced the teacher and got me into the school. I had a deal with my mum that I would go to school till it snows again. However, the next five years, it did not snow again. My mother had tricked me and I didn't know that it only rarely snows in my region. Years later, it was my turn to trick them. Especially, my grandmother always asked me: "When will your finish your school?" (Nine, okul bitti). So finally, I am finishing my "school". In all these years, it was not clear to them what I was doing. The confusion was big: physics or music?

I want to thank many people in more or less chronological order and I am sorry if I forgot anyone. I was always very lucky and met lots of nice people along my way.

I want to start with thanking my parents. For several years, I gave private lessons to younger students when I was in school and at the university, and I often realized the pressure students are receiving from their parents. At that time, I was sort of jealous of them, but nowadays, if I look back, I can say I had a great childhood and never felt any pressure from my parents. Also, I had a nice brother who could explain to me the things illustratively when I was a child (Anney, buba, abe - gecirdigim o güzel cocukluk yillarim icin, cok sagolun!).

After coming home from my cleaning job, I sat in the kitchen during high school time, listening my grandpa's stories that had a big influence on me. I learned many things from him while I was living and working with him. (Dede - bana anlattigin hikayeller, bilhassa senin yasadigin olaylar beni hep azimlendirdi!)

Leaving home during high school time and deciding to finish my school and go to university was a very critical step in my life. Without the help of my teachers Füsun and Gert, this would have been much more painful and maybe it would have never happened. (Tesekkürler Füsun! - Ich bin sehr froh, euch getroffen zu haben.. Vielen Dank für alles Rena und Gert.)

From university years, I would like to thank my friend Simon. I wish you were here! Of course, how could we play "DoKo" without Arne and Lukas. Danke euch!

From early DESY times, I want to thank Jens, Charlie, Alberto, Timon, Christopher, Eugen, Marc, Sebastian, Carlos and Johann. Wackeldackel, danke schön!

Someone has to fight against darkness and ignorance, and Mark Hoca, you are doing it very well! Thank you! Hauke and Takanori, two very different personalities with a common enemy in the office!

UFOX time, special thanks to my supervisor Prof. Franz X. Kärtner for giving me the chance for being a part of a big project and letting me gain invaluable experience in labor. And, a big thanks to Dr. Nicholas H. Matlis for encouraging me to join his team, for trusting me and believing in me! He is a great motivator! Over the duration of my thesis, I had the pleasure to work directly with Giovanni - you are welcome - Michael, Damian and Wenlong. I really benefit from various colleagues in the AXSIS team and I want to thank to Luis, Kelly, Arya, Wenchao, Lu, Timm, Tobi, Moein, Dongfang, Mikahil, Simon, Martin, Jelto and Javier! In coffee time, I always had very interesting discussions about various topics with colleagues: Hong, Fabian, Stefano, Giulio, Roland, Miguel, Neetesh, Elias, Felix, Guangjin, Faisal, Salah and Nico - cheers mate! Thank you! Additionally, I want to thank my lokum mates: Huseyin, Ümit, Hakan, Kemal, Umut and Ersin.

Final thank goes to Selen (Sonunda bitti mi yoksa?).

CONTENTS

I THESIS

II APPENDIX

Part I

THESIS

1

INTRODUCTION

"X" was used to indicate an unknown type of radiation discovered by Wilhelm Röntgen in 1895. As if it was a quirk of fate, these x-rays are used to investigate a range of unknown chemical, biological and physical structures. Starting from simple Crookes tubes to today's complex, large accelerator facilities; high brilliance x-rays are generated with synchrotrons and free-electron lasers (FELs). It is currently the most used method to determine the structure of matter.

Nowadays, FELs, such as the European XFEL, provide high intensity, femtosecond x-ray pulses, enabling the usage of the "diffraction before-destruction" principle to investigate the ultrafast biochemical processes with atomic resolution. These x-rays are generated from highly energetic electrons (tens of GeV) by passing them through an alternating magnetic module, called undulator. The state-of-art radio frequency (RF) driven conventional acceleration in copper or superconductivity cavities was utilized to reach these electron energies. However, this technique is limited to field strengths of tens of MeV/m, due to the field emission from the cavity walls and pulsed magnetic heating of the metallic inclusions. Therefore, the acceleration lengths to reach high energies (for example, 1.7 km by XFEL) result in costly, large facilities, which unfortunately means limited accessibility for users.

The empirical studies show that these limitations scale with $1/\tau^{1/6}$, where τ is the pulse duration of the accelerating field [47]. Thus using terahertz radiation in the 0.1-0.6 GHz region with picosecond pulse duration, instead of RF (1-3 GHz, S-band frequency) with pulse durations in the millisecond range, the breakdown field gradients could increase to the GeV/m range, enabling a large reduction in the size of the accelerator. Besides shortening the acceleration lengths, higher field gradients would also lower the electron emittance with reasonable charge values of a few pC, leading to an x-ray pulse compression in the attosecond range. Therefore, THz accelerator units enable the next generation of x-ray experiments, namely "probe before destruction" in the attosecond range. This is crucial for investigating the dynamics of biochemical processes before destroying the electronic structure of the atoms.

The AXSIS (Frontiers in Attosecond X-ray Science: Imaging and Spectroscopy) project arose to develop and build a THz-driven compact electron accelerator [22]. The current goal of this project is to accelerate electrons up to the $\sim 20\,\mathrm{MeV}$ level, which then will generate $\sim 10\,\mathrm{keV}$ x-rays by inverse Compton scattering with a 1 μm laser. These x-rays will then be used to investigate the dynamics of light reactions, electron transfer, and protein structure in photosynthesis. One of the main challenges in this project is fulfilling the terahertz requirements for the accelerator, namely: narrowband, multicycle

(MC) THz radiation centered at $\sim 0.3\,\text{THz}$ with a sub-percent level bandwidth and pulse energies of $\sim 20\,\text{mJ}$, with hundreds of picosecond pulse duration [44]. These MC-THz generation parameters are far beyond the current technology.

There are many methods to generate THz (a review is given in [16]). However, for high field gradient multicycle (MC) THz generation, the most promising methods revolve around optical laser-driven sources, using periodically poled, second-order nonlinear materials, such as Mg-doped periodically poled lithium niobate (MgO:PPLN) [41]. Previously, using a method of optical rectification (OR), where the MC-THz radiation is generated via difference-frequency mixing between Fourier components of the same optical pulse, a conversion efficiency (CE) of 0.13% was achieved [6]. Currently, the highest CE was achieved using a chirp and delay (C&D) technique, where a broadband pulse is chirped, divided into two pulses and one pulse is delayed. If the relative spectral phase of the optical pulses can be tuned, a maximum CE of 0.24% was reached [21].

The key to all these techniques is difference frequency generation (DFG): $\Omega_{THz} = \omega_1 - \omega_2$, where Ω_{THz} is the angular THz frequency and $\omega_{1,2}$ are the closely spaced optical angular frequencies. Based on the Manley-Rowe relations [30], a maximum CE of 0.1% could be expected, with values based on the current parameters needed for the AXSIS project ($\Omega_{THz}/(2\pi) = 0.3\,\text{THz}$ and $\omega_{1,2}/(2\pi) \sim 300\,\text{THz}$). However, already with the OR and C&D techniques, parametric cascading effects are active, where optical pump photons are repeatedly reused in two processes: down conversion (creating THz photons), as well as, up-conversion (annihilating THz photons). If down-conversion is preferred, quantum efficiencies of greater than 100% can be achieved, allowing the Manley-Rowe limit to be surpassed (see Section 2.5).

Another key development in MC-THz generation is the use of the quasi-phase-matching (QPM) mechanism using periodically poled (PP) crystals. Because of the large difference in phase velocity between the THz and optical frequencies, conventional phase matching techniques produce very short coherence lengths. QPM provides phase matching over the length of the crystal; thus greatly increasing the interaction length (see Section 2.2). In this work, two periodically poled crystals are investigated: MgO:PPLN and rubidium-doped periodically poled potassium titanyl phosphate (Rb:PPKTP). The critical material properties of these nonlinear materials are compared in Section 2.7; included in this comparison are figure-of-merit values for THz generation.

Recently, in numerical simulations, conversion efficiencies (CE) around the 1% level were predicted using an optical pump pulse consisting of two spectral lines (around 1 μm) separated by the THz frequency [42]. Thus, in this work, a pump laser with a spectrum of two spectral lines will be developed (Chapter 4), achieving 20 mJ with a two-line spectrum around 1 μm. Thereafter, in Chapter 5, high CE will be experimentally researched using the nonlinear materials: MgO:PPLN and Rb:PPKTP.

Although new world records in CE were experimentally achieved (0.49% at 0.3 THz and 0.89% at 0.53 THz) with this new laser system using MgO:PPLN (see Chapter 5), the final MC-THz energy still needs to be scale to 20 mJ, required by the AXSIS project. Therefore, the input laser energy must be increased, as well as the size of the aperture of the crystals. Currently, the largest commercially available crystal aperture for MgO:PPLN is $4 \times 4\,\mathrm{mm}^2$. In special development and collaboration with the group of Prof. Kärtner, the group of Prof. Taira have made MgO:PPLN crystals with an aperture size of $10 \times 15\,\mathrm{mm}^2$ [19]. These crystals were tested using a commercial laser with 200 mJ of pulse energy, 500 fs at 1030 nm using OR as the THz conversion mechanism (Chapter 6). Although OR has a lower CE compared to the new results, the larger pump energies are required to test the larger apertures. Additionally, larger MC-THz energies produced by this laser system can now be used to drive the next generation of THz-based electron accelerators, while improvements to the CE of the MC-THz generation can continue in parallel.

The production method to created PPLN or PPKTP from single crystals has limitations both in the aperture size and the poling thickness. Note: The largest known PPLN crystals are produced by the group of Prof. Taira, described above. Therefore, to further increase the aperture size of single crystal wafers are stacked with the *c*-axis alternatively reversed. Each wafer has an anti-reflective coating at 1030 nm. Therefore, in Chapter 7, large wafers of LN and KTP were investigated as an alternative approach to the normally produced periodically poled crystals.

Finally, with the LN wafers, two novel experiments were carried out: multi-stage wafer-stacks in a serial configuration (Chapter 7, Section 7.2.1), and back-reflected seeded MC-THz generation (Chapter 7, Section 7.2.2). Both methods improve the efficiency of the MC-THz generation, compared to a single stack. In the case of the serial configuration, the results compare well with numerical simulations [42]. However, the results of the back-reflected seeded MC-THz generation are very promising. It is shown that the seeded MC-THz generation can increase the efficiency by three times compared to the non-seeded case.

In Chapter 8, the main results are summarized and discussed. Additionally, a roadmap is presented describing how to reach the THz requirements of the AXSIS project, including new methods to increase the CE of the MC-THz generation further.

2

THEORY AND CRITICAL MATERIAL PROPERTIES

2.1 NONLINEAR OPTICS

Shortly after the demonstration of the laser in 1960 using a ruby crystal [28], the first, nonlinear light-matter interaction (second harmonic generation) was observed in 1961 in a quartz crystal [11]. The efficiency was in the range of 10^{-12} due to the lack of phase-matching, which would increase the efficiency.

Physically, when an external oscillating electric field is applied to a material, the material becomes polarized, given by

$$\mathbf{P}(\omega) = \varepsilon_0 \chi^{(1)}(\omega)\mathbf{E}(\omega) \tag{2.1}$$

where $\chi^{(1)}$ is the linear optical susceptibility and ε_0 is the permittivity of free space. The linear susceptibility defines the refractive index of the material as follows $\chi^{(1)} = n^2 - 1$, which is responsible for the effects such as dispersion.

After the lasers was discovered, which provide sufficient intense light to modify the matter in a nonlinear manner, the expression in Eq. (2.1) must be modified as

$$\mathbf{P} = \varepsilon_0 (\chi^{(1)}\mathbf{E} + \chi^{(2)}\mathbf{E}^2 + \chi^{(3)}\mathbf{E}^3 + ...) \tag{2.2}$$

where $\chi^{(2)}$ and $\chi^{(3)}$ are second and third order nonlinear susceptibilities and for simplicity are represented at scalar quantities.

2.1.1 *Second order nonlinear processes*

When a material has noncentrosymmetry, second order nonlinear effects can occur. By putting the electric field $\mathbf{E}(t) = E_1 e^{-i\omega_1 t} + E_2 e^{-i\omega_2 t} + c.c.$ into the equation

$$\mathbf{P} = \varepsilon_0 \chi^{(2)}\mathbf{E}^2, \tag{2.3}$$

the polarization becomes

$$\begin{aligned}\mathbf{P}^{(2)}(t) = \varepsilon_0 \chi^{(2)} \Big[& E_1^2 e^{-2i\omega_1 t} + E_2^2 e^{-2i\omega_2 t} + 2E_1E_2 e^{-i(\omega_1+\omega_2)t} + \\ & 2E_1E_2^* e^{-i(\omega_1-\omega_2)t} + c \cdot c \cdot \Big] + 2\varepsilon_0 \chi^{(2)} \left[E_1E_1^* + E_2E_2^*\right].\end{aligned} \tag{2.4}$$

Each term in Eq. (2.4) describes a different 2^{nd}-order nonlinear effect, which can be rewritten as:

$$\begin{aligned} P\left(2\omega_1\right) &= \varepsilon_0\chi^{(2)}E_1^2 \quad \text{(SHG)} \\ P\left(2\omega_2\right) &= \varepsilon_0\chi^{(2)}E_2^2 \quad \text{(SHG)} \\ P\left(\omega_1+\omega_2\right) &= 2\varepsilon_0\chi^{(2)}E_1E_2 \quad \text{(SFG)} \\ P\left(\omega_1-\omega_2\right) &= 2\varepsilon_0\chi^{(2)}E_1E_2^* \quad \text{(DFG)} \\ P(0) &= 2\varepsilon_0\chi^{(2)}\left(E_1E_1^*+E_2E_2^*\right) \quad \text{(OR)} \end{aligned} \tag{2.5}$$

The terms in Eq. (2.5) describe second harmonic generation (SHG), sum frequency generation (SFG), difference frequency generation (DFG) or optical parametric amplification (OPA), and optical rectification (OR), respectively.

2.1.1.1 *Second order tensor components*

For simplicity in Section 2.1.1, $\chi^{(2)}$ was written as a scalar, but should be considered as a third rank tensor $\chi^{(2)}_{ijk}$, which has 27 elements (for more details see Ref. [5]). Generally, this tensor can be contracted by introducing a contracted matrix d_{ij}, written as

$$\begin{bmatrix} P_x^{(2)} \\ P_y^{(2)} \\ P_z^{(2)} \end{bmatrix} = 2\varepsilon_0 \begin{bmatrix} d_{11} & d_{12} & d_{13} & d_{14} & d_{15} & d_{16} \\ d_{21} & d_{22} & d_{23} & d_{24} & d_{25} & d_{26} \\ d_{31} & d_{32} & d_{33} & d_{34} & d_{35} & d_{36} \end{bmatrix} \begin{bmatrix} |E_x|^2 \\ |E_y|^2 \\ |E_z|^2 \\ E_yE_z^*+E_y^*E_z \\ E_xE_z^*+E_x^*E_z \\ E_xE_y^*+E_x^*E_y \end{bmatrix}. \tag{2.6}$$

2.1.2 *Third order nonlinear processes*

Third-order effects, described by a tensor of rank 4 ($\chi^{(3)}_{ijkl}$), include four-wave mixing, and high-intensity effects, such as the nonlinear refractive index ($n = n_0 + n_2 I$). This produces self-focusing and self-phase modulation at high intensities in the spatial and temporal domains, respectively (for more details see Ref. [5]).

2.2 PHASE MATCHING SECOND ORDER NONLINEAR PROCESSES

For effective energy conversion, using the nonlinear processes listed in Eq. (2.5), two conditions are required: energy and momentum conservation. For example, the second order DFG process, illustrated in Fig. 2.1, must satisfy energy conservation:

$$\hbar\omega_3 = \hbar\omega_1 - \hbar\omega_2, \tag{2.7}$$

where $\omega_{1,2,3}$ the angular frequencies of the three waves. Momentum conversion must be fulfilled also, which is generally called the phase-matching condition:

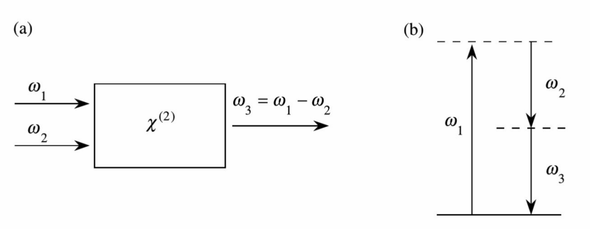

Figure 2.1: Difference frequency generation: a) Two waves ($\omega_{1,2}$) interact in a $\chi^{(2)}$ material and generate a new wave at ω_3, where b) the energy conservation ($\omega_3 = \omega_1 - \omega_2$) must be fulfilled.

$$\mathbf{k}_3 = \mathbf{k}_1 - \mathbf{k}_2, \tag{2.8}$$

where $\mathbf{k}_{1,2,3} = n(\omega_{1,2,3})\omega_{1,2,3}/c_0$ are the wave vectors, with n the refractive index and c_0 the speed of light in vacuum. If this condition is fulfilled, *perfect phase-matching* ($\Delta\mathbf{k} = \mathbf{k}_1 - \mathbf{k}_2 - \mathbf{k}_3 = 0$) is achieved. However, it is often difficult to achieve, due to the differences in the frequency-dependent refractive indices. Different tricks can be played to fulfilled the phase matching condition, such as *temperature-controlled phase-matching* by tuning the temperature of the nonlinear crystal; and *angle phase-matching* by tuning the angle dependence of the refractive index of the nonlinear crystals (for more details see Ref. [5]).

Another approach is the *quasi-phase matching (QPM)*, in which the sign of nonlinear optical coefficient is alternated along the propagation direction of waves. The periodically poling of the nonlinear coefficient acts as a wave vector ($\mathbf{k}_\Lambda$), which can compensate the wave vector mismatch ($\Delta\mathbf{k}$), an example is illustrated in Fig. 2.2.

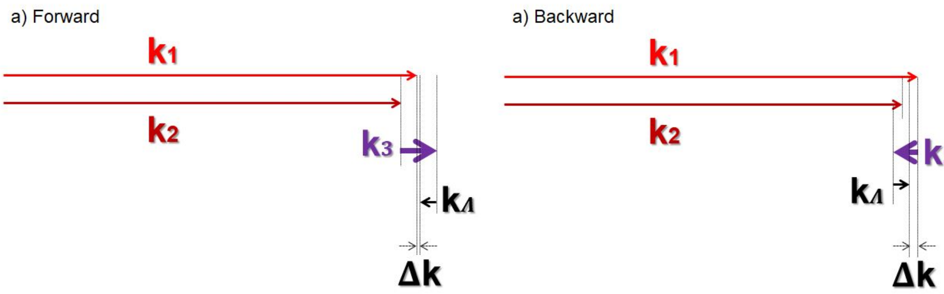

Figure 2.2: An example of quasi-phase matching (QPM) in a periodically poled nonlinear $\chi^{(2)}$-material with a poling period of Λ for the case of DFG: a) forward-direction and b) backward-direction phase matched.

Fig. 2.2 illustrates QPM for DFG generation. In the case of THz generation, $k_3 = k_{THz}$ is very small compared to the wave vectors $k_{1,2}$. Therefore, in the case of THz generation, it is often possible to phase-match both the forward and backward propagating wave vector k_3. Thus, QPM phase matching (Δk) in the forward direction is given by

$$\Delta \mathbf{k} = \mathbf{k}_2 + \mathbf{k}_3 - \mathbf{k}_1 - \mathbf{k}_\Lambda, \tag{2.9}$$

where $\mathbf{k}_\Lambda = 2\pi/\Lambda$, with Λ the poling period of the crystal (Fig. 2.2).

2.3 THZ GENERATION

Terahertz (THz) radiation roughly covers the spectral range from 0.1 THz to 30 THz. An extensive review of THz generation methods can be found elsewhere [16]; such methods include photoconductive antenna, air-plasma generation, undulator-based generation, and various methods using nonlinear crystals such as OR and DFG (see Eq. (2.5)).

2.3.1 *Optical Rectification (OR)*

In optical rectification, THz radiation is generated in a nonlinear medium via difference-frequency mixing between Fourier components of the same optical pulse. In single $\chi^{(2)}$ crystals, phase mismatch limits the effective length of the crystal and therefore produces limited conversion efficiency. In order to improve the efficiency of the conversion by increasing the interaction length between the THz and optical waves, QPM in nonlinear materials can be utilized.

In the case of QPM, the phase mismatch Δk for the THz generation in forward direction (Fig. 2.2) is given by

$$\Delta k = k(\Omega) + k(\omega) - k(\omega + \Omega) - \frac{2\pi}{\Lambda}, \tag{2.10}$$

where Λ is the poling period of the QPM-crystal, ω is the angular frequency of the optical pulse and Ω is the angular frequency of the THz. Especially for THz, using the fact that $\Omega << \omega$, the Eq. (2.10) can approximated by

$$\Delta k \approx \frac{\Omega}{c_0}\left(n_{THz} - n_o^{gr}\right) - \frac{2\pi}{\Lambda}, \tag{2.11}$$

where n_{THz} is the refractive index at THz frequencies and n_o^{gr} is the optical group velocity refractive index. Thus, the center frequency of the THz is given by

$$\Omega_0 = \frac{2\pi c_0}{\Lambda \Delta n}, \tag{2.12}$$

where

$$\Delta n = n_{THz} - n_o^{gr} \tag{2.13}$$

is the index mismatch. By differentiating Eq. (2.11), we get $\frac{d(\Delta k)}{d\Omega} = \Delta n / c_0$ and the phase-matching acceptance bandwidth based on the condition $\Delta k L/2 = \pi$ with crystal length L is

$$\Delta\Omega^{accept} = \frac{c_0}{\Delta n}\Delta k^{accept} = \frac{2\pi c_0}{L\Delta n}. \tag{2.14}$$

Combination of Eq. (2.12) and Eq. (2.14), determines the relative phase matching acceptance

$$\frac{\Delta\Omega^{accept}}{\Omega_0} = \frac{1}{N}, \tag{2.15}$$

where N is the number of periods over a crystal length L.

Note: In the absence of QPM, the interaction between the optical and THz waves is limited to the coherence length

$$l_c = \pi c / \Omega \Delta n. \tag{2.16}$$

Here, the length of the polarized domain ($\Lambda/2$) contributes to one half-wave of the THz pulse; thus the THz wave packet has as many oscillation cycles as the number of QPM periods over the length of the crystal [26], as illustrated in Fig. 2.3.

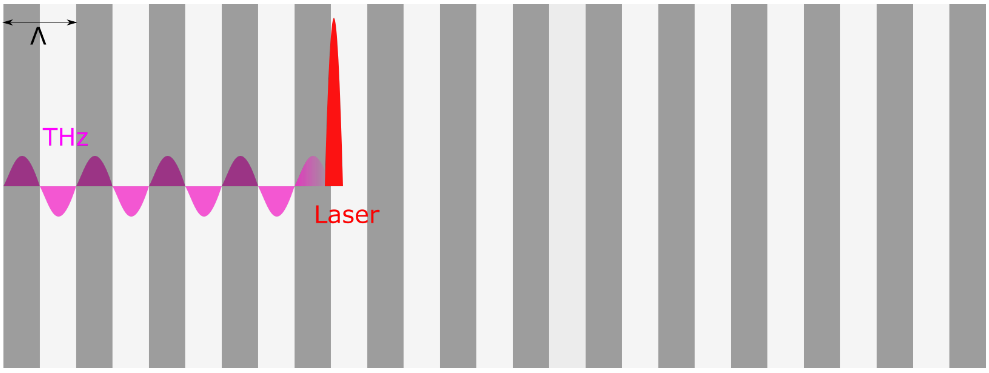

Figure 2.3: Schematic drawing of narrowband MC-THz generation. The optical pulse generates a half-wave of the THz in each domain ($\Lambda/2$) of the periodically poled crystal.

The the conversion efficiency (CE) was derived for the case of plane waves [40]. In this analytical derivation, THz absorption, pump depletion, cascading effects and third order nonlinear effects are neglected. Thus optical-to-THz fluence efficiency $\eta_{THz} = F_{THz}/F_o$ for OR was derived [40]

$$\eta_{THz} = g_1 \frac{2\Omega_0^2 d_{\text{eff}}^2 L}{\varepsilon_0 c_0^2 n_{THz} n_o^2 \Delta n} F_o, \tag{2.17}$$

where ε_0 is the vacuum permittivity, n_o is the optical refractive index, n_{THz} is the THz refractive index, $d_{\text{eff}} = \chi^{(2)}/2$ is the effective nonlinear coefficient, and

$$g_1 = \exp\left(-\left(\tau\Omega_0/2\right)^2\right), \tag{2.18}$$

the reduction factor, where τ is the pulse duration of the optical laser pulse. In OR, g_1 reflects the fact that the optical bandwidth must be larger than the THz frequency. If, $\tau\Omega_0 < 1$, thus $g_1 \approx 1$ and the conversion efficiency (CE) does not depend on pulse duration. Finally, for OR, the value of d_{eff} is derived from the electro-optic coefficient, using the relation $d_{ij} = -r_{ij}n_o^4/4$ [50]. In this thesis, for potassium titanyl phosphate (KTP) and lithium niobate (LN) crystals, where the polarization of the optical and THz waves are aligned along the optical z-axis, the coefficient r_{33} is used (see Table 2.1). In the analytical expression, Eq. (2.17), the value of $d_{\text{eff}} = (2/\pi)d_{33}$ [40].

2.3.2 *Difference Frequency Generation (DFG)*

The optical-to-THz conversion efficiency can be improved by using DFG ($\Omega_0 = \omega_3 = \omega_1 - \omega_2$) with longer picosecond pulses, such that $\Omega_0\tau > 2\pi$ [41]. Here, it is assumed that the optical pulses (ω_1, ω_2) are Gaussian with equal pulse duration τ. The temporal walk-off length between the optical and THz pulses can be introduced

$$l_w = \frac{\sqrt{\pi}c_0\tau}{\Delta n}. \tag{2.19}$$

In the absence of the THz absorption, pump depletion, third order nonlinear effects and cascade effects, the optical-to-THz conversion efficiency (CE) can be approximated for two cases [40]:

- In the limit of long pulses, $l_w >> L$, the CE is given by

  $$\eta_{THz} = \frac{2\Omega_0^2 d_{\text{eff}}^2 L^2}{\varepsilon_0 c_0^3 n_{THz} n_o^2}\frac{I_o}{\sqrt{2}} \tag{2.20}$$

  where I_o is the intensity of the optical pulse. Note, the CE depends on the intensity of the optical pulse and the length squared.

- In the limit of short pulses, $l_w << L$, the CE is given by

  $$\eta_{THz} = g_2\frac{2\Omega_0^2 d_{\text{eff}}^2 L}{\varepsilon_0 c_0^2 n_{THz} n_o^2 \Delta n}F_o, \tag{2.21}$$

  where

  $$g_2(l_w/L) = \frac{1}{\pi}\int_{-\infty}^{\infty}\exp\left(-(l_w/L)^2\mu^2/\pi\right)\operatorname{sinc}^2(\mu)d\mu, \tag{2.22}$$

is the reduction factor. Note: the CE depends only on the fluence, as in the case of OR (see Eq. (2.17)). Provided the same optical fluence, F_o, in both cases (DGF ps-pulses and OR fs-pulses), the same CE can be achieved (compare Eq. (2.17) and Eq. (2.21)).

In Chapter 5, long optical pulses are used ($l_w >> L$) and according to Eq. (2.20), the CE is proportional to the intensity of the optical pulse, which is typical for χ^2 processes. It might be expected to improve the CE by decreasing the pulse duration, which in turn increases the intensity; however, below a certain pulse duration, the long pulse duration assumption might not be valid. This can be explained by the correlation between the pulse duration and temporal walk-off length (Eq. (2.19)). Reducing the pulse duration decreases the temporal walk-off length in which the optical and THz can interact coherently. Additionally, in this case, efficiency scales as L^2, similar to standard SHG.

2.3.3 *Chirp and Delay Technique*

Another possibility to increase the efficiency of narrowband MC-THz generation is using the so-called chirp and delay mechanism [35]. This approach was first used to generate narrowband MC-THz from photoconducting antennas [43]. Recently, using this technique for optical DFG in cryogenically cooled PPLN, efficiencies of ∼0.1% were demonstrated [2], which could be increased up to 0.24% by tuning the relative spectral phase of the optical pulses [21].

In this method, a broadband pulse is chirped, divided into two pulses, and one of the pulses is delayed. Fig. 2.4 illustrates, in a Wigner distribution, the two pulses for two cases: the first case (a) has a purely linear chirp and the second case (b) has the more realistic chirp with 3rd order dispersion included. The highest efficiency can be achieved in case (a). However, in a more realistic situation, the phase of the pulses has to be compensated for increasing the efficiency, as was attempted in Ref. [21].

2.4 THZ ABSORPTION AND EFFECTIVE CRYSTAL LENGTH

So far, in the simple wave analysis, the absorption of the THz in the crystal is neglected, and the CE grows with crystal length (Eq. (2.17) and Eq. (2.21)) and with crystal length squared (Eq. (2.20)). However, in reality, the absorption limits the MC-THz generation. This is the reason why the PPLN must be cooled down cryogenically to reduce the THz absorption.

Wang et al. [42] introduced two critical length parameters for the optimization of the MC-THz generation. In order to define these lengths, δ is introduced: $\delta = \Delta n/(c_0\tau)$. The two critical lengths, with α_{THz} the THz absorption coefficient, are now defined as follows:

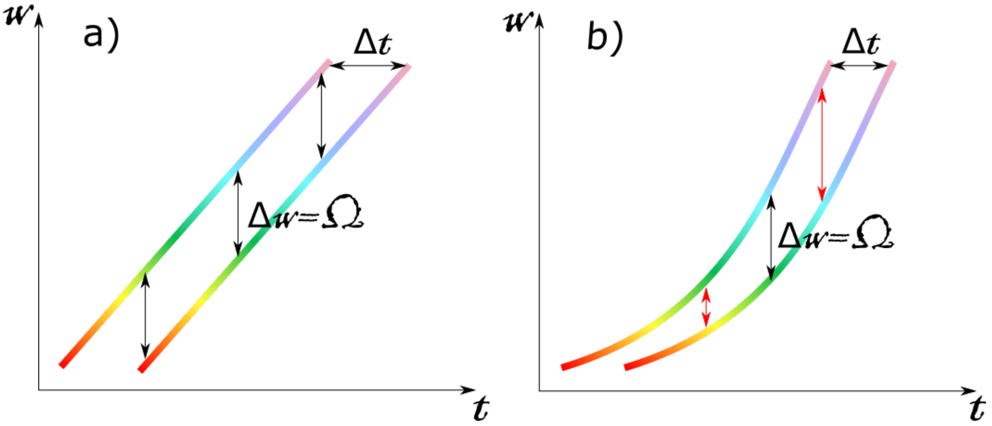

Figure 2.4: Chirp and delay mechanism demonstrated in a Wigner distribution (y-axis - frequency, x-axis - time domain): a) ideal two pulses, which are purely linearly chirped; at a certain delay the required frequency difference is achieved. b) Two pulses having higher-order dispersion (3rd order and higher); for a given time delay, the pulses have partly the right frequency difference.

- For short pump pulses, $\frac{\delta}{\alpha_{THz}} \gg 1$,

$$L_0 = \frac{\tan^{-1}(\delta/\alpha_{THz})}{\delta}. \tag{2.23}$$

- For long pump pulses, $\frac{\delta}{\alpha_{THz}} \ll 1$

$$L_0 = \frac{2\ln(2)}{\alpha_{THz}}, \tag{2.24}$$

$$L_{\text{eff}} = \frac{2}{\alpha_{THz}} \ln\left(\frac{2}{1-\sqrt{1-e^{-1}}}\right). \tag{2.25}$$

The length parameter L_0 is where the efficiency increase is most rapid and L_{eff} is where the efficiency reaches a plateau. For example, in the long pulse limit, for a THz pulse centered at 0.3 THz in a cryogenically cooled lithium niobate with $\alpha_{THz} \approx 1.4\,\text{cm}^{-1}$: $L_0 \approx 1\,\text{cm}$ and $L_{\text{eff}} \approx 3.3\,\text{cm}$.

2.5 MANLEY-ROWE RELATION AND PARAMETRIC CASCADING EFFECTS

Manley-Rowe relations are a set of relations for a lossless material, which conserve photon quantities within three-wave mixing. Thus using DFG, the quantum efficiency of the process limits the maximum optical-to-THz conversion efficiency by the Manley-Rowe relations [30]:

$$\eta_{THz}(max.) = \frac{\Omega_{THz}}{\omega_o}. \tag{2.26}$$

As an example, the maximum conversion efficiency of an optical pulse at 1 μm to 0.3 THz is $\eta_{THz} = 10^{-3}$.

The limit set by the Manley-Rowe relations can be broken in MC-THz generation through a process called cascaded parametric generation [35, 36, 42]. Essentially, a pump photon can be reused to produce a phase-matched THz-photon in a repeated down-conversion process, as illustrated in Fig. 2.5. Up-conversion consuming a THz-photon is also possible (Fig. 2.5). These processes broaden the bandwidth of the pump pulse until it is stopped when the corresponding frequencies are not phased-matched. Thus, the Manley-Rowe conversion limit is surpassed.

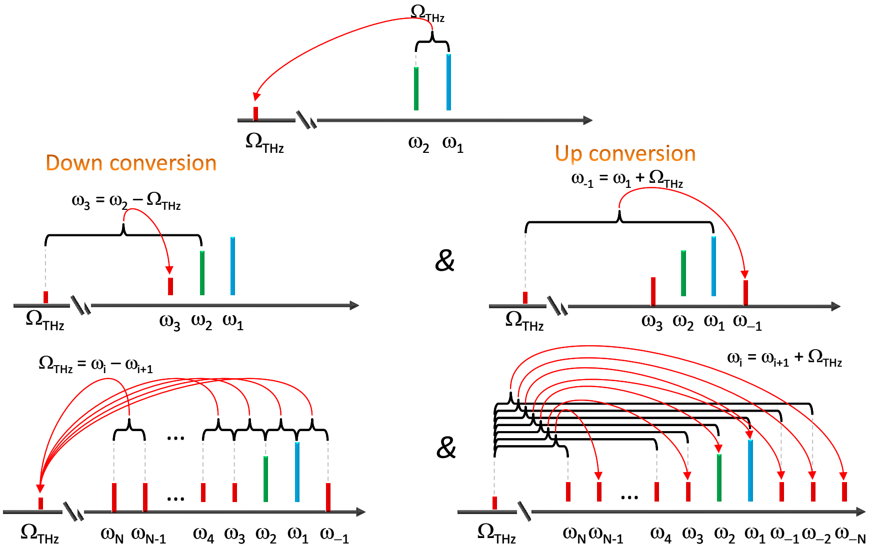

Figure 2.5: Cascading optical-THz interactions: the first row shows the single DFG process for the generation of a single THz photon. Thereafter, both down-conversion (left) and up-conversion (right) are possible. The generated THz can interact back with the optical beam and broaden the optical spectrum.

Now, the cascaded process, ultimately limited by phase-matching condition, can be remedied by re-phasing the optical and/or THz pulse [42], or by varying the PPLN period along the crystal length [36].

It would appear that the possibility of up-conversion and down-conversion are symmetric (Fig. 2.5); however the dispersion properties of the material breaks this symmetry and prefers down-conversion [33]. As an example, the phase mismatch (Eq. (2.10)) as a function of detuning the seed frequency in lithium niobate is shown in Fig. 2.6. Additionally, the preference for down-conversion can be further manipulated by careful choice of optical pump phase and spectral distribution, as well as, phase matching manipulation through aperiodic poling (see Ref. [32] and references therein).

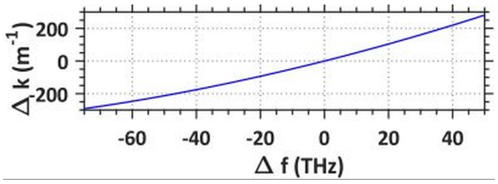

Figure 2.6: The phase-mismatch as a function of detuning the signal frequency for lithium niobate (LN) is plotted (taken from Ref. [33]).

2.6 NUMERICAL SIMULATIONS OF MC-THZ GENERATION USING A SPECTRAL TWO-LINE OPTICAL LASER SOURCE

Quasi-3-dimensional (2-dimensional with cylindrical symmetry) numerical simulations for MC-THz generation at 0.3 THz were carried out on periodically poled lithium niobate (PPLN) using a two-spectral-line pump source [42]. Both spectral lines had equal magnitude centered at 1 μm and the simulations were carried out with parameters close to liquid nitrogen. THz absorption, 3rd order nonlinear effects, pump depletion, and cascading effects are all included. Additionally, self-focusing and diffraction effects are included because spatial effects with cylindrical symmetry are also simulated. As a result, the simulated pump source is close to the constructed laser source described in Chapter 4 with one important difference; the simulations used a spatial flat-top (super-Gaussian with $m = 5$) compared to the Gaussian shape of the experimental pump pulse. Thus the expected efficiencies should be higher than the experiment. Finally, except for the spatial profile of the pump pulse, the results of the simulation can be compared to the experimental results given in Chapters 5 and 7.

In addition to simulating a single stage PPLN, simulations were performed also on a multi-stage PPLN in series [42], illustrated in Fig. 2.7. The main results of the numerical simulations for four stages are depicted in Fig. 2.8. Two cases are considered: in the first case (Fig. 2.8(a)), the optical beam is directly injected into each stage in series without any pump phase (disper-

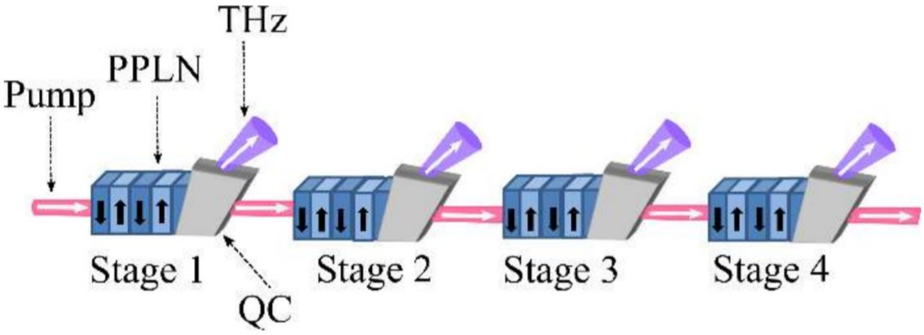

Figure 2.7: Simulation of a multi-stage PPLN crystals in a serial arrangement. The pump is a two-line optical laser source and the quartz couplers (QC) are utilized to separate the optical and the THz beam (taken from Ref. [42]).

sion) manipulation; in the second case (Fig. 2.8(b)), after the first stage, the pump pulse is phase (dispersion) compensated after each stage to maximise the efficiency in the next stage (see details in [42]).

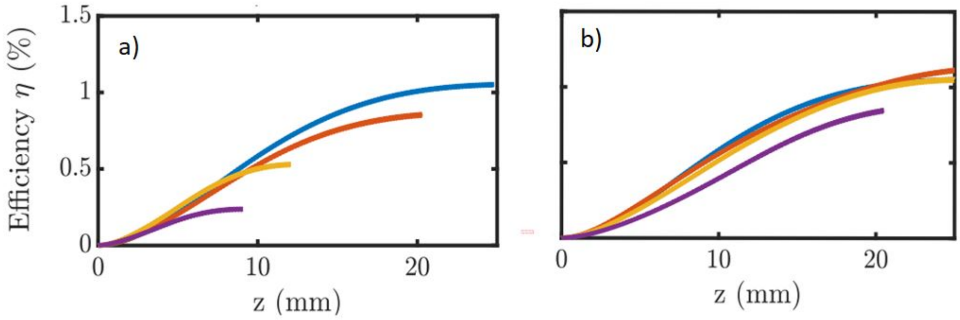

Figure 2.8: Output THz conversion efficiency as a function of crystal distance for a four stage PPLN arrangement (Fig. 2.7): output stage 1 (blue), output stage 2 (red), output stage 3 (yellow), output stage 4 (purple). a) Without dispersion compensation, b) with dispersion compensation, see text for details (taken from Ref. [42]).

As shown in Fig. 2.8(a), the maximum efficiency of 1.05% is reached after the first stage. The optimal crystal length and the efficiency decrease in the next stages with increasing stage number. The reason for this reduction in the efficiency is due to the change of the spectral phase caused by SPM and cascading effects. By compensating these nonlinear effects after each stage, the interaction length and efficiencies can be increased (Fig. 2.8(b)).

2.7 COMPARISON OF MATERIAL PROPERTIES OF NONLINEAR CRYSTALS

In this thesis, the MC-THz generation will be investigated with two nonlinear optical materials: lithium niobate (LN) and Potassium titanyl phosphate (KTP). In order to compare the crystals for MC-THz generation, three figure-of-merits (FOM) were introduced by Vodopyanov [41]. They are defined for the following cases:

- The long optical pump pulse case

$$FOM_1 = \frac{d_{\text{eff}}^2}{n_o^2 \alpha_{THz}}, \tag{2.27}$$

- The short optical pump pulse case

$$FOM_2 = \frac{d_{\text{eff}}^2}{n_o^2 \Delta n}, \tag{2.28}$$

- Kerr-limited interactions

$$FOM_3 = \frac{\lambda_o d_{\text{eff}}^2}{n_o^2 n_{THz} \alpha_{THz} n_2}. \tag{2.29}$$

A summary of the main optical properties of these crystals are summarized in Table 2.1, together with FOM values and effective crystal lengths defined in Section 2.4.

Table 2.1: Comparison between the optical crystal parameters of KTP and LN (* at CT). The notation is defined in the text of this chapter. FOM – figure-of-merit – is defined in Section 2.7 and are normalized to the crystal LN. The absorption coefficients (α_{THz}) are measured using a commercial THz time-domain spectrometer at CT (see Section A.2).

Parameter	KTP	LN
crystal type	biaxial	uniaxial
λ_o [nm]	1030	1030
$n_o(\omega_o)$	1.83* [24]	2.16* [51]
$n_o^{gr}(\omega_o)$	1.87	2.21
Δn (Eq. (2.13))	1.9	2.68
$n_{THz}(\Omega_0)$	3.78* [29]	4.9* [46]
r_{33} [pm/V]	36.3 [4]	28 [9]
d_{33} [pm/V]	101.7	152.4
α_{THz} [cm^{-1}]	0.25*	1.4*
FOM$_1$	3.47	1
FOM$_2$	0.88	1
FOM$_3$	2.4	1
E_{gap} [eV]	3.52 [49]	4
n_2 [$\times 10^{-19}\,\text{m}^2/\text{W}$]	2.3 [1]	1.25 [7]

3

CHIRP AND DELAY WITH NARROWBAND PULSES

Even though optical rectification with compressed pulses in lithium niobate is the most commonly used method for optical THz generation, it has two main limitations: intensity-related damage of the crystal and temporal walk-off between optical and THz beams. The latter is more critical for the narrowband, multicycle MC-THz than in SC-THz generation.

Numerical simulations show that using an optical pulse sequence instead of a single compressed pulse could be a game-changer in narrowband MC-THz generation [35, 42]. This method enables high conversion efficiencies up to a few percent, which targets both aforementioned limitations, namely by lowering the peak intensity by stretching the optical pulses and having optical and THz radiation in phase over a longer interaction length, enabling buildup of the THz coherently. One of the possibilities to create a pulse sequence is the so-called chirp and delay (C&D) approach, in which two replicas of a linearly chirp pulse are generated, delayed relative to each other, and recombined again [43]. The frequency difference between the two pulses can be set exactly to the THz frequency by choosing the right delay between the two replicas. Conversion efficiencies of up to 0.24% have been demonstrated previously using this technique [21], which are presently the highest yet to be achieved. However, these experiments were performed with a joule-class, broadband Ti:sapphire laser, which is a drawback when the repetition rate should be increased as needed in the AXSIS project. In the future, the AXSIS-project should operate at a kilohertz repetition rate. Presently, joule-class Ti:sapphire lasers cannot operate at kHz repetition rate, which is instead possible using narrowband Yb-based lasers [3]. Only such a laser source with high energy and repetition rate the predicted several percent of optical-to-THz efficiencies [35] could reach the MC-THz requirements of the AXSIS-project. Therefore, the C&D concept is tested for the first time using a narrowband Yb-based laser source.

In this chapter, the THz generation by the C&D technique using a narrowband, home-built, cryogenically cooled Yb:YLF laser is investigated. PPLN-crystals phase-matched for 0.3 and 0.5 THz were utilized.

3.1 EXPERIMENTAL SETUP

The laser system was a home-built laser, which consists of three parts: a fiber-based front-end [18], a cryogenically cooled Yb:YLF regenerative amplifier [15] and a cryogenically cooled Yb:YLF four-pass amplifier. The system provided pulses centered at 1020 nm with a bandwidth of 2.2 nm (Fig. 3.1) and pulse energies of up to 50 mJ at a repetition rate of 10 Hz. This laser is still in development; the pulse energy and repetition will be further increased. Recently, the repetition rate was successfully increased to 3.5 kHz with a pulse energy of 20 mJ [8].

For these experiments shown in this chapter, the output of the laser was taken before the grating-compressor and sent to the experimental setup shown in Fig. 3.1.

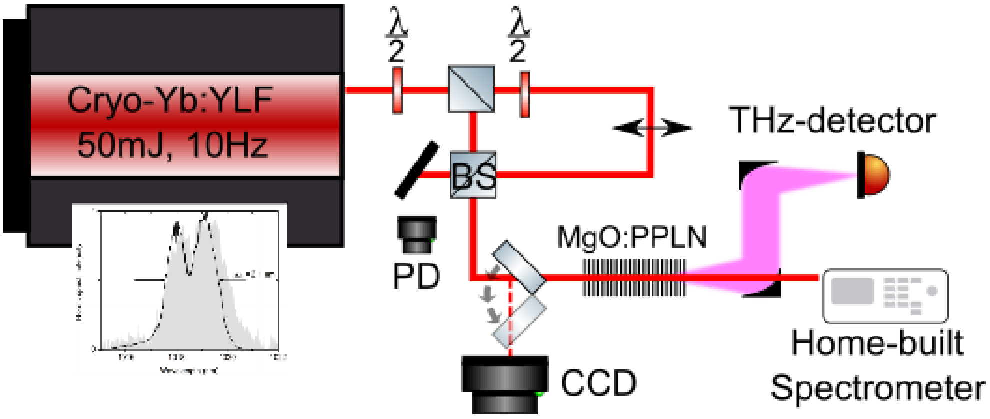

Figure 3.1: Chirp and Delay experimental setup for narrowband MC-THz generation.

The laser pulse energy can be adjusted using a half-wave plate (HWP) and a thin-film polarizer (TFP). The HWP was mounted in a motorized rotation stage, which enables automatized energy scans. First, the laser beam was split into two arms using another HWP and TFP. The second HWP can be used to adjust the ratio between both arms. The MC-THz generation was most efficient when the ratio between the two pulses was equal. The transmitted arm is p-polarized, which was converted to s-polarized using another HWP. It is important to note that the mechanism behind the phase matching was the type-0 quasi-phase-matching (QPM), which means that both pump photons must have the same polarization. The transmitted arm was delayed using a translation stage, and then both arms were recombined using a non-polarizing 50:50 beam splitter (BS). The motorized translation enables automatized delay scans, which measures the delay-dependent THz yield for a given laser pulse energy. After recombining in a non-polarizing BS, there were two outputs with the same power: one of them was used to monitor the shot-to-shot laser energy by a photodiode, and the other one was demagnified by a telescope and sent into the PPLN crystal.

Two off-axis parabolic (OAP) mirrors were utilized to detect the MC-THz signal: the first OAP mirror had a 3 mm hole in the middle, which was used to separate the laser and the THz beam, given the fact that the THz has a stronger divergence due to its thousandfold bigger wavelength. The transmitted laser beam was monitored by a home-built spectrometer to observe the spectral changes due to the MC-THz generation and annihilation.

3.2 DELAY AND FLUENCE DEPENDENT MC-THZ GENERATION

Before starting the delay scans, the delay stage was first aligned, ensuring that both arms were spatially overlapping throughout the travel range of the translation stage (150 mm). The spatial overlap was tested with the spatial fringes at the crystal position given the fact that provided temporal overlap; the spatial fringes appear only when both beams overlap at an angle, so complete constructive or destructive interference was accomplished. After aligning the translation stage, the maximum temporal overlap (Δt_0) position on the stage was determined, which is when optical paths in both arms are the same. To determine Δt_0, the position-dependent spectra of the combined beam were observed.

Analogical to the spatial domain, the fringes appear in the spectral domain when both beams have a temporal delay relative to each other. An example of such a measurement is shown in Fig. 3.2a, the fringe density grows with the increasing delay between the two pulses. In Fig. 3.2b, Fourier transforms of each spectrum from different stage positions, i.e. relative delays, are shown. As expected, the side peaks separate more with increasing delay between the pulses. The zero temporal overlap position (Δt_0) of the pulses ($\Delta t_0 \approx$ 142.5 mm) is determined, where the side peaks in Fig. 3.2b converge to main peak in the middle.

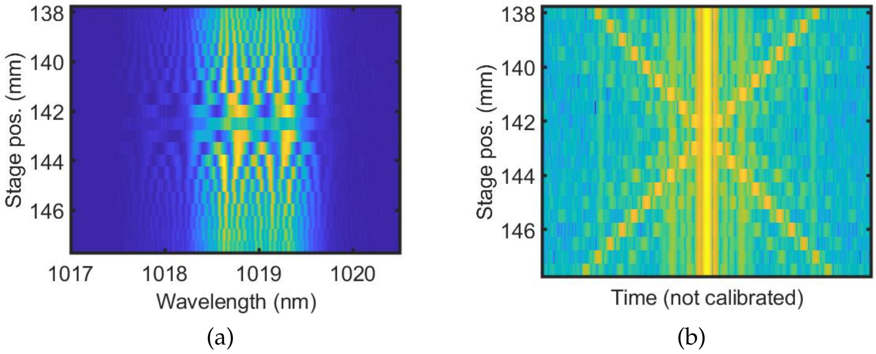

(a) (b)

Figure 3.2: a) Optical spectra measured by the home-built spectrometer after recombination of two beams for different delays (Stage pos.) and b) their Fourier transform.)

After determining the Δt_0 position, the first MC-THz generation experiments were performed at room temperature (RT) in a 5% MgO doped PPLN with dimensions $4 \times 4 \times 40\,\text{mm}^3$. Its poling periodicity was 400 µm, which is phase-matched for ~0.3 THz. Firstly, in order to determine the optimal delay between two pulses, where the frequency separation is equal to the phase-matched frequency of the crystal, a delay scan has been performed. Before starting the scan, the delay was set approximately to the theoretical excepted value, which can be calculated based on the chirp rate from the fiber stretcher in front-end of the laser system and the expected phase-matching frequency. Once the MC-THz signal was detected, automatized pulse energy-dependent delay scans were performed. The input laser energy was set using the rotation stage and measured in front of the crystal with a calibrated powermeter, which was then kept the same during the delay scan. The MC-THz signals and the laser spectra were automatically read out by the oscilloscope (Tektronix) and the spectrometer simultaneously. The results of these delay scans for different input energies are plotted in Fig. 3.3a. The x- and y-axis show the delay between pulses and generated internal THz energy, respectively. Different colors indicate different input energies. The internal MC-THz energy was computed by considering the MC-THz losses (see Tab. 3.1) and its Fresnel's losses by transmission from crystal to air (44.4%).

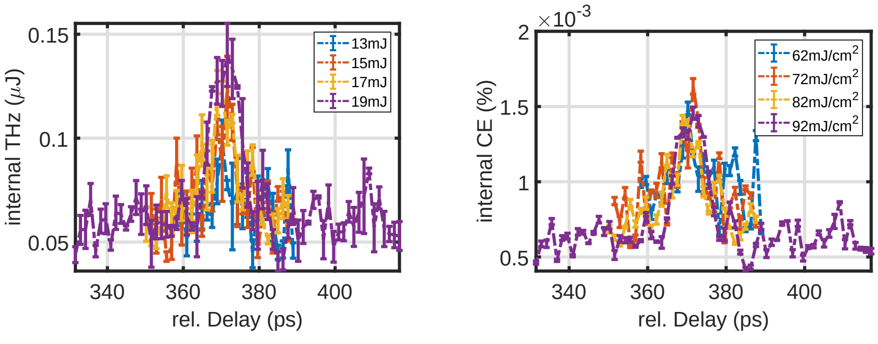

(a) (b)

Figure 3.3: Delay-dependent a) MC-THz yield and b) corresponding conversion efficiencies for different input energies in 5% MgO:PPLN with poling period 400 µm at RT.

Table 3.1: MC-THz losses in different materials at 300 & 500 GHz.

Frequency (GHz)	Teflon(%)	Vacuum window (%)	Polyethylene(%)
300	8	35	34
500	6	46	43

After considering geometrical (∼40%) and Fresenel losses (13.3%) of the laser beam, the internal optical-to-THz conversion efficiencies were calculated depending on the laser peak fluence (see Fig. 3.3b). The maximum internal MC-THz energy of 0.14 µJ was obtained at a relative delay of ∼372 ps, which corresponds to an internal efficiency of 1.6×10^{-5}% at the maximum peak fluence of 92 mJ/cm^2.

The same experiment was repeated under the same conditions after the cryogenically cooling of the crystal with liquid nitrogen. Results for both internal MC-THz yields and efficiencies are plotted in Figs. 3.4a & 3.4b. As can be seen, the optimal relative delay is shifted to ∼405 ps. This is because of the change of the phase matched frequency, which is related to temperature-dependent refractive indices. Cooling down the crystal increased the THz yield up to 3.7 μJ level, which corresponds to an internal efficiency of 0.037%

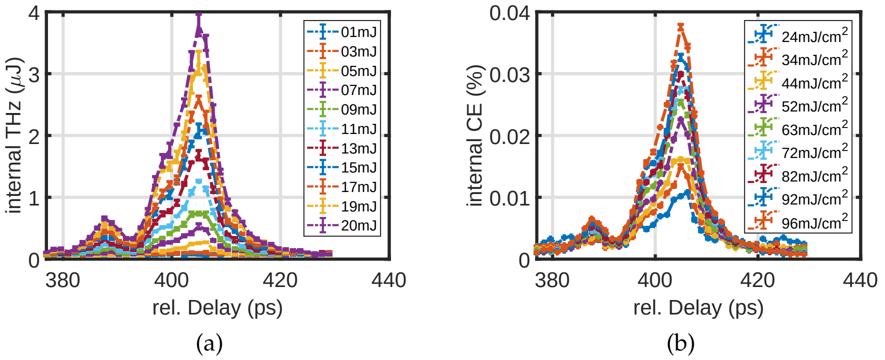

(a) (b)

Figure 3.4: Delay-dependent a) THz yield and b) corresponding conversion efficiencies for different input energies in MgO:PPLN with poling period 400 μm (cryogenically cooled with liquid nitrogen).

at a maximum laser peak fluence of 96 mJ/cm^2. The second peak in delay-dependent MC-THz yield can be understood with the help of the spectral profile of lasers (see Fig. 3.1). In a linearly chirp pulse, the frequency (wavelength) and the time can be replaced; in other words, different colors come in at different times. Hence, the temporal profile has two peaks, which show up in the intensity-dependent MC-THz generation process.

Simultaneously, with the delay-dependent MC-THz yields, the spectra were captured by a home-built spectrometer after the interaction. This spectrometer is cross-calibrated with an optical spectral analyzer. In order to retrace MC-THz dependent energy transfer in the spectral domain of the optical pulse, the reference spectrum, which was measured before the MC-THz generation, is subtracted from each delay-dependent spectrum and normalized. This means the energy is transferred from negative to positive parts of the spectra. A red or blue shift in the spectrum indicates the MC-THz generation or annihilation, respectively. The delay dependent, reference subtracted, normalized spectra are depicted in Fig. 3.5a and Fig. 3.5b for the same input energy of 19 mJ at RT and cryogenically cooled, respectively. The y- and x-axis show the relative delay between optical pulses and wavelength, respectively.

In both Fig. 3.5a,Fig. 3.5b, oblique lines are visible indicating that different parts of the spectra were contributing to the MC-THz generation for different relative delays, which is an indicator of a nonlinear chirp in the optical pulses. According to the MC-THz results, the spectral broadening is strongest when the MC-THz yield is maximized. At cryogenic temperatures, a clear cascaded usage of optical photons is visible in both directions, whereas at RT, no cascading effects are visible. The lines are narrower at cryogenically cooled temperatures compared to RT, which is related to the length-dependent phase-matching bandwidth. Indicating that the crystal length is effectively shorter for the MC-THz at RT; in other words, only the MC-THz generated in the last part of the crystal is not completely absorb.

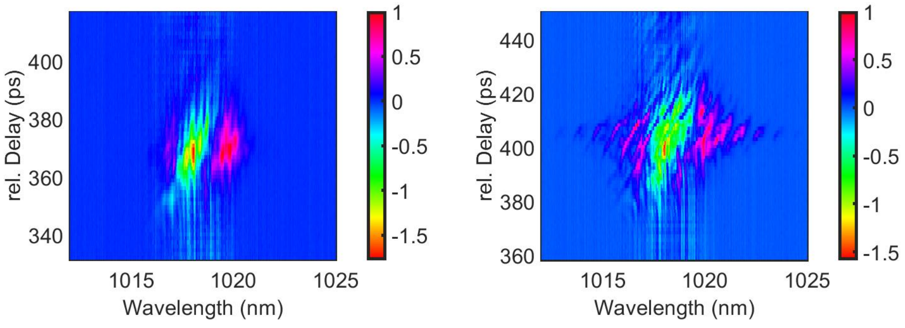

(a) (b)

Figure 3.5: Delay dependent spectral behaviour in MgO:PPLN with poling period 400 µm with a input energy of 19 mJ a) at RT and b) cryogenically cooled with liquid nitrogen.

The next round of scans was performed using another crystal with the same dimensions: 4×4×40 mm^3. However, with a different poling period of 212 µm. This crystal is phase-matched for ∼0.5 THz. Therefore, the required wavelength separation, as well as the required relative delay, are larger than in the previous case. The first scan was performed at RT where the fluence was increased up to 17 mJ and the MC-THz signal remained at noise levels. As shown in Fig. 3.6a a small indication of energy transfer is visible, which suggest that for MC-THz generation crystal absorption dominates.

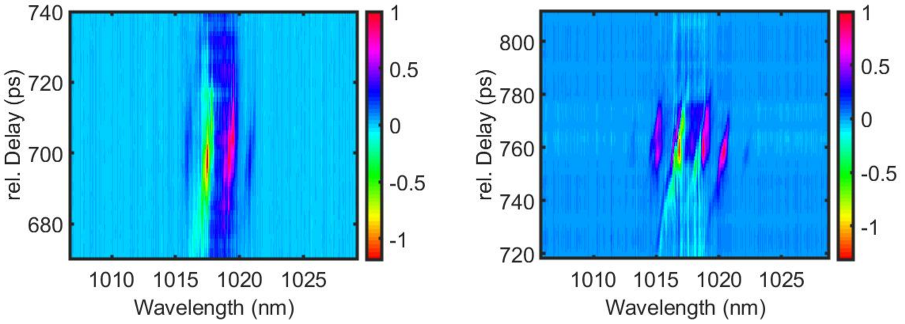

(a) (b)

Figure 3.6: Delay dependent spectral behaviour in MgO:PPLN with poling period 212 μm with a input energy of 17 mJ a) at RT and b) cryogenically cooled with liquid nitrogen.

After cryogenically cooling the crystal, the MC-THz signal increased to 1.7 µJ, corresponding an internal efficiency of 0.02% (Fig. 3.7a) at a peak fluence of 88 $\mathrm{mJ/cm}^2$ (Fig. 3.7b). The required relative delay between the two optical pulses increased to 760 ps, meaning that only roughly 20% of the pulses overlapped. The delay-dependent, reference spectrum subtracted spectral evolution is shown in Fig. 3.6b. As in the previous scans at cryogenic temperatures, spectral cascading is present.

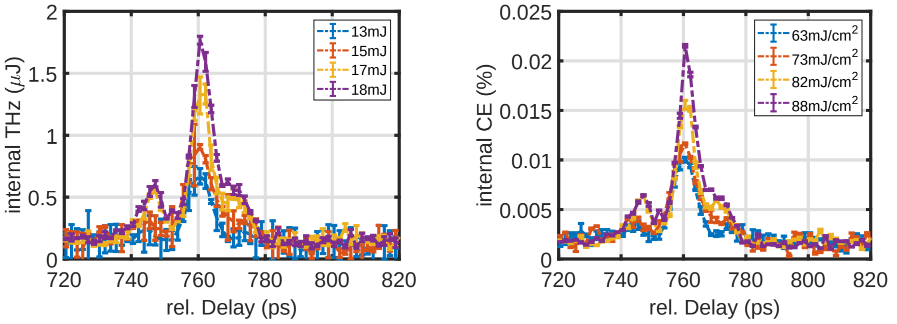

(a) (b)

Figure 3.7: Delay dependent a) THz yield and b) corresponding conversion efficiencies for different input energies in MgO:PPLN with poling period 212 μm (cryogenically cooled with liquid nitrogen).

3.3 DISCUSSION OF RESULTS

The results of both measurements at cryogenic temperatures are summarized at optimal relative delays (see Fig. 3.8a and Fig. 3.8b) for 400 µm and 212 µm poling periods, respectively.

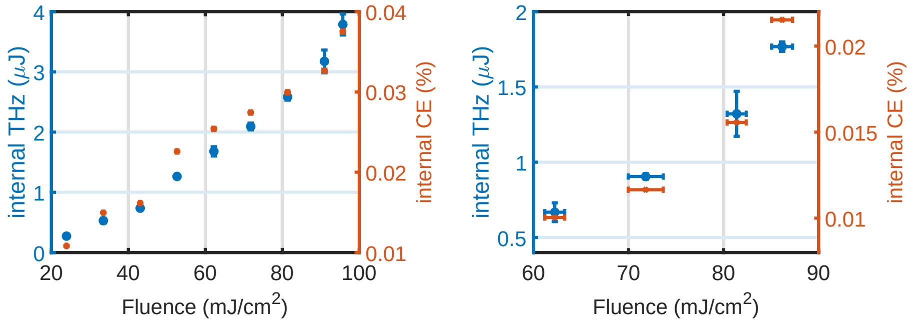

(a) $\Lambda = 400\,\mu$m (b) $\Lambda = 212\,\mu$m

Figure 3.8: Internal efficiency as a function of laser peak fluence in 5% MgO:PPLN with the poling period of a) 400 µm and b) 212 µm.

In both cases, the laser peak fluence was increased up to $\sim$100 mJ/cm^2. Although there is no clear indication of saturation in the efficiency curves, the spectral measurements show clearly for a given relative delay that only small fraction of spectral components of the pulses contribute to MC-THz generation, which is due to the residual nonlinear chirp in the optical pulses. In order to increase efficiency further for the same laser peak fluences, either the nonlinear chirp must be compensated before sending them into the crystal, or as demonstrated by Spencer et al. before [21], the spectral phase of one of the pulses must be adjusted so that more spectral parts could contribute to the MC-THz generation.

However, this approach's biggest drawback for narrowband optical pulses is the lack of temporal overlap between the two interacting pulses. As the delay scans have shown, the required optimal relative delays were around 405 ps and 760 ps for the poling periods of 400 μm and 212 μm, respectively, which is equal to a relative shift compared to the pulse duration of around 45% and 75%, respectively. In addition, the temporal profile is varying, which reduces efficiency as well. The highest part of the temporal profile contributes to the MC-THz generation only in a limited manner due to the delaying process, which risks damaging the crystal. Considering the low damage threshold of the lithium niobate at cryogenic temperatures, and generally low efficiencies of the optical MC-THz generation process, this method is not suitable for the AXSIS project.

Therefore, it was decided to build a laser specifically developed for efficient MC-THz generation (see Chapter 4) instead of trying to optimize the C&D process.

4

MULTI-LINE LASER SOURCE FOR EFFICIENT NARROW-BAND MULTI-CYCLE (MC) THZ GENERATION

To date, the optical DFG is one of the most promising candidates to reach the required high field (hundreds of MV/m), high peak energy (tens-of-millijoules), narrowband MC-THz (0.1-0.6 THz) to drive the compact THz driven electron accelerator.

Initial works in optical THz generation have been performed using optical rectification (OR) from compressed pulses. Efficiencies of ~0.1% level were achieved using this approach in a cryogenically cooled PPLN [6], which was strongly limited by intensity related damage threshold of the crystals.

Vodopyanov et al. have been shown analytically mixing two narrowband optical pulses for DFG produces the same efficiency as using OR from a compressed pulse [40]. Furthermore, Ravi et al. has shown having a long driving pulse sequence could increase the efficiency up to several percent level [35].

Ahr et al. has utilized the chirp and delay (C&D) technique to generate pulse sequences from stretched pulses from a joule-level Ti:sapphire laser. Similar efficiencies of ~0.1% as in OR has been demonstrated [2]. Stretching the pulse allows reducing the optical peak intensity and increase the optical input energy, which improved the THz yield by over an order of magnitude to ~40μJ. The investigation of delay-dependent MC-THz generation in C&D technique has shown that the residual nonlinear chirp in optical pulses limits the efficiency of the MC-THz generation. Spencer et al. could increase MC-THz by over an order of magnitude to ~450 μJ and reached an internal efficiency of 0.24% by tuning the relative spectral phase of the pulses from the same Ti:sapphire laser and increasing the crystal aperture size using the large aperture PPLN. This efficiency is still too low to reach the narrowband THz source requirements for the AXSIS project with the available joule-level laser sources. Besides, the repetition rate should be increased to the kHz-level to increase the x-ray flux. So far, reaching this repetition rate using the Ti:sapphire-based lasers is not possible, mainly due to heat loading. Therefore, we decided to use Yb-based sources, where already ~kW [3] average powers have been demonstrated. The results from the previous chapter 3 show MC-THz generation with a narrowband laser source is even more challenging. Besides the nonlinear chirp, the poor temporal overlap between the delayed pulses became an important limitation.

Therefore, it was decided to build a new laser source which consists of only narrow spectral lines repeated by the THz frequency. These spectral lines generate a pulse sequence in the temporal domain. Efficiencies up to the several percent levels have been predicted by optical DFG in cryogenic cooled PPLN [35]. Therefore, it should be possible to fulfill the requirements on the THz source using the joule-level optical pulses available today.

The simplest method to generate the narrowband THz by an optical DFG via quasi-phase-matching (QPM) is sending a compressed laser source with enough spectral bandwidth into a periodically poled (PP) crystal. The crystal then converts the spectral components that fulfill both the energy and phase-matching conditions for the THz frequency, determined by the poling periodicity of the crystal. Using this approach, THz has been generated with ∼1 µJ using compressed Ti:sapphire laser pulses in a cryogenically cooled PPLN CE of 0.1% [6], which was mainly limited by the damage threshold of the crystal due to high peak laser intensity.

By stretching the pulses temporally from a joule-level Ti:sapphire laser, the optical input energies could be scaled up, and the THz pulse energy could be increased to ∼40 µJ using the so-called chirp and delay (C&D) technique [2]. In the C&D technique, two replicas of linear chirp pulses, delayed relative to each other and then recombined, are sending it into the PPLN. The residual nonlinear temporal chirp in these pulses limits fully the contribution of available pump photons to the THz generation, which leads to low efficiencies around 0.06%.

By tuning the relative spectral phase of the pulses from the same Ti:sapphire laser and increasing the crystal aperture size using the large aperture PPLN, the THz energy could be improved by over an order of magnitude to ∼450 µJ with total internal efficiency of 0.24%. This efficiency is still too low to reach the narrowband THz source requirements for the AXSIS project with the available joule-level laser sources. Besides, the repetition rate should be increased to the kHz-level to increase the x-ray flux. So far, reaching this repetition rate using the Ti:sapphire-based lasers is not possible due to the heat load. Therefore, we decided to use Yb-based sources, where already ∼kW [3] average powers have been demonstrated.

The results from the C&D experiments with a narrowband Yb:YLF (Chapter 3) demonstrated that the THz efficiency suffers from residual nonlinear chirp and from the poor temporal overlap between the delayed pulses.

Taking all previously mentioned experiences into account and the supporting evidence from numerical simulations [32, 34–36, 42], it is decided to build a Yb:based laser source, especially for efficient narrowband THz generation, which will be integrated into the front-end laser of the AXSIS project that can power up all parts of the laser system. This ensures an optical synchronization of all components, which is critical for a working x-ray source. The chosen basal laser parameters are as follows:

- Yb based laser at 1μm: These sources provide low heat load due to the small quantum defect, and are cost-efficient using pump diodes with high-brightness. From the THz side, the parasitic multi-photon absorption in PPLN is more unlikely compared to the Ti:sapphire.

- Two-line spectral-domain: The laser consists of at least two narrow spectral lines, whose wavelength separation can be tuned. Ideally, with a course tuning to change the phase-matching frequencies and fine-tuning to optimize it, which is more crucial for the narrower phase-matching.

- Temporal domain: A pulse duration of hundreds of picosecond with a flat-top profile. One of the most limiting factors in THz generation is the damage threshold of the crystal, therefore to maximize the pulse energy by staying below the damage peak intensity, a flat-top is required. Ideally, tunability is needed to optimize the efficiency and the temporal profile of the THz.
- Pulse energy: Considering the low conversion efficiencies from optical-to-THz, joule level energies are required to fulfill a THz source's requirements.
- Repetition rate: In order to have the necessary x-ray flux at the experimental setup, planned to have a kHz repetition.
- Timing: The phase of THz must be controlled relative to the electron bunch's injection time into the Linac, so that into Linac injected electrons experiences the same acceleration.

In this chapter, a specially designed laser source for efficient narrowband THz generation is introduced, which fulfills the above requirements.

4.1 THE FRONT-END OF THE MULTI-LINE LASER

In order to develop the front-end part of the laser source for efficient MC-THz generation, two single-frequency, continuous-wave (CW) lasers are employed. Their outputs are combined in a polarization-maintaining (PM) fiber and chopped sequentially in a fiber-pigtailed acousto-optic modulator (AOM) and an electro-optic modulator (EOM) to chop it down to hundreds of picosecond pulses. These choppers are placed between ytterbium-doped fiber amplifiers (YDFA) to amplify the pulses to nanojoule-level pulse energies. Each YDFA has a fiber pump diode and each Yb-doped gain fiber has different lengths and an optical isolator. The isolators are inserted to protect the chopper and amplification stages from unwanted back-propagating pulses. A schematic of the front-end part is visualized in Fig. 4.1.

One of the two CW lasers is a stable, single-frequency laser (from *Stable Laser Systems*). It is stabilized by locking to an ultra-stable reference cavity [10], which ensures a frequency drift of less than a few kHz per day. The other CW laser is an external cavity laser diode (from *Toptica DL Pro*) with a tunable wavelength from approximately 1000 nm to 1080 nm. The outputs of both CW lasers are combined and split into two parts; one part is used for the locking mechanism (described in Section 4.4), and the other part is used as a seed for the multi-line laser. This combination creates a beat signal in the temporal domain, whose modulation is determined by the frequency difference of the CW-lasers ($\omega_{1,2}$). The frequency difference is set to the desired

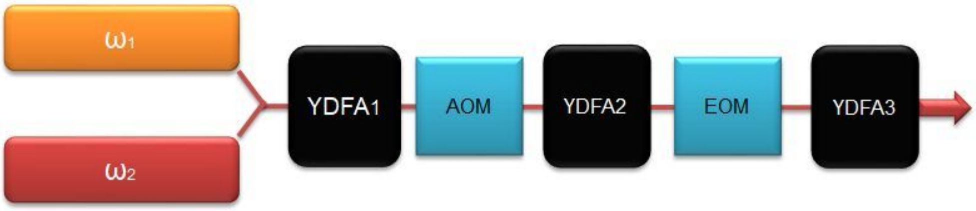

Figure 4.1: The chosen configuration for the multi-line front-end: Two CW-lasers at angular frequencies ω_1 and ω_2 are combined, chopped successively in an AOM and an EOM, which are sandwiched between ytterbium-doped fiber amplifiers (YDFA).

terahertz frequency ($\Omega_{THz} = \omega_2 - \omega_1$). This temporal modulation, generated by combining both lasers, drives the coherent THz generation. The output power of both lasers is set approximately equal to 6 mW to enhance the contrast of the temporal modulation. The spectrum of combined lasers is measured using the optical spectral analyzer (*OSA- AQ-6315A, YOKOGAWA*), see Fig. 4.2a. The spectrometer wavelengths of both lasers are set roughly to 1 nm (see Fig. 4.2*b*), which is the required wavelength-separation for the desired THz frequency of 0.3 THz. The spectral contrast of both lines is around 60 dB.

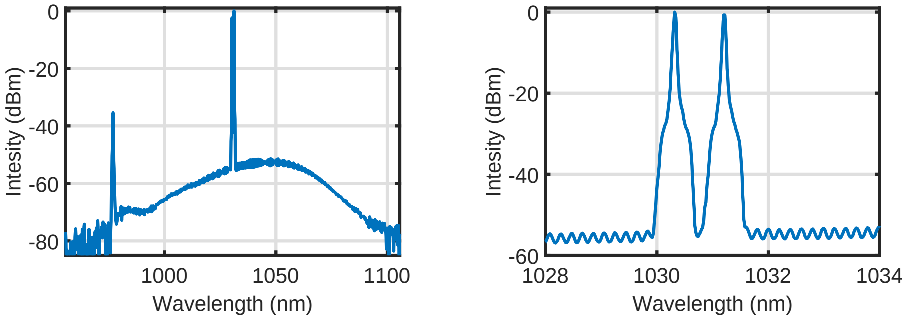

(a) seed: zoomed out

(b) seed: zoomed in

Figure 4.2: Spectra of the combined output of both CW seed lasers: Stable laser and tunable laser. a) zoomed out: both seed lasers around 1030 nm with the residual pump at approximately 980 nm b) zoomed in: both seed lasers.

Two different configurations are tested for the chopping of the pulses from the CW seed source.

- Case 1: In contrast to Fig. 4.1, the EOM is placed before the the AOM (YDFA, EOM, YDFA2, AOM). The EOM has high insertion losses, and compared to the AOM, a low acceptance power of about 200 mW makes it challenging to amplify the weak input signal. Additionally, since all fiber amplifiers must run in continuous mode, amplified spontaneous emission (ASE) is amplified, as shown in Fig. 4.3. The spectral contrast of the lines gets worse with amplification.

  In a modification to Case 1, a bandpass filter could be placed behind the 2nd amplifier while using a 3rd amplifier to boost the signal before

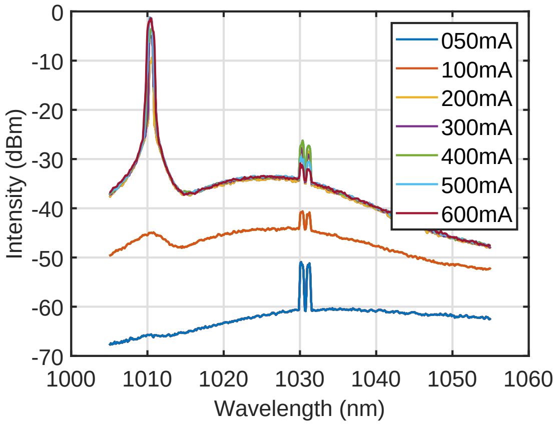

Figure 4.3: Case 1 chopping configuration: first EOM then AOM. The spectral evolution after the second amplifier is shown. The signal of the AOM output is so weak that mainly the ASE gets amplified.

entering the AOM with input energy of 1 W, and finally amplifying the post-AOM again to get the required seed energies for the regenerative-amplifier.

- Case 2: The AOM is preceding the EOM as used in the final setup (see Fig. 4.1). The AOM has lower inertial losses and accepts a higher input power. Firstly the seed is amplified up to 450 mW in a polarization maintained (PM) ytterbium-doped-fiber amplifier (YDFA1) before sending it into AOM. A 5 nm bandpass-filter is inserted behind the amplifier to eliminate any ASE and ensure that mainly the wanted seed is fed into the chopper (see Fig. 4.4a). A closer look shows that in the lower range of the spectrum, there are the sidebands generated from the two main peaks. Spectral sidebands are generated in the single-mode fiber (SMF) by the four-wave-mixing (FWM) of two CW-laser.

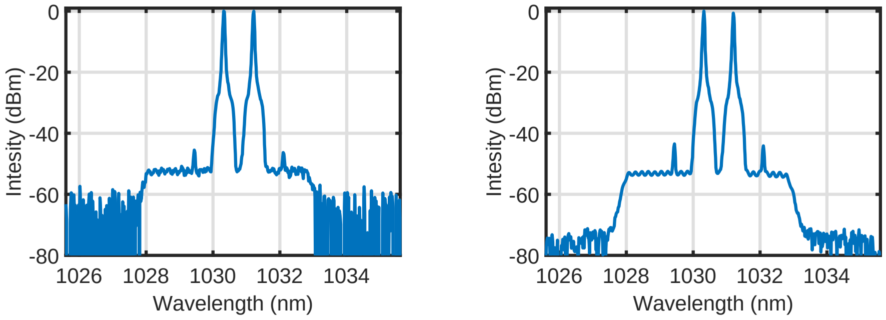

(a) after YDFA1

(b) after AOM

Figure 4.4: a) Spectral profile of both CW lasers after first amplifier YDFA1; a band-pass filter (BPF) is used to improve the signal to noise ratio. Two sidebands are generated by four-wave-mixing (FWM) in single-mode-fiber (SMF). b) Spectra after the chopping the CW laser using the acousto-optic modulator (AOM).

The following text now describes Case 2 in detail (see Fig. 4.1). The output of the YDFA1 is approximately half the maximum acceptance power of the AOM (1 W). This fiber-coupled AOM operates at 200 MHz, using a TeO$_2$ crystal with a rise time of around six nanoseconds. Pulses around 15 ns are chopped at 2 MHz. This repetition rate is the maximum chopping rate of the EOM. Both optical modulators: AOM and EOM are triggered by the same delay generator (*DG645*), which in turn, is externally triggered by a reference clock from an oven-controlled crystal oscillator (*InWave B-110*) at 10 MHz.

An additional measurement was performed to characterize the performance of the AOM. Both the AOM and the sampling scope (*Agilent DCA-X86100D*) are connected to the DG645. The pulse shapes for different TTL signal widths are acquired. Fig. 4.5 shows the resulting traces. As can be seen, pulses shorter than 10 ns drop in intensity. Above 20 ns, the pulses remain the same. Additionally, the rising time of the device is faster than its falling time, therefore for a chopping time of 15 ns was decided (see Fig. 4.7a). Taking the insertion loss of 3.5 dB from the AOM, and a duty cycle of 3% into account, the measured average output energy of 6 mW aligns well with the expected value. The insertion loss includes optical transmission through the crystal, diffraction efficiency, and coupling losses. The spectral profile after AOM is shown in Fig. 4.4b. The spectral contrast of the lines remains as before.

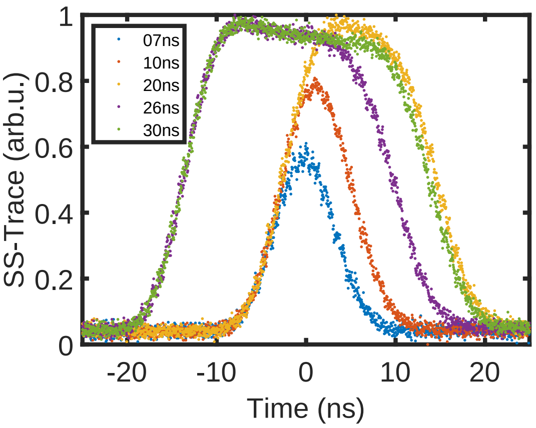

Figure 4.5: Chopped time traces from the AOM output: pulses with different pulse durations: 7, 10, 20, 25, 30 ns are compared.

The second Yb-amplifier (YDFA2, see Fig.4.1) further amplifies this signal to 180 mW, which is slightly below the EOM's maximum input power (200 mW). In this amplification and filtering out process, new sidebands are generated by the FWM, as shown in Fig. 4.6a. This amplified signal is sent into the EOM for final chopping.

The EOM (*IXblue modbox*) offers computer-programmable pulse shaping using an arbitrary waveform generator (AWG). The EOM is PM-fiber pigtailed and exhibits a high extinction ratio greater than 55 dB (at 1030 nm). The AWG offers a maximum frequency of 2 MHz, 12 bits resolution, a maximum D/A rate of 4 GS/s, the maximum memory size of 4 MS (1 ms). The

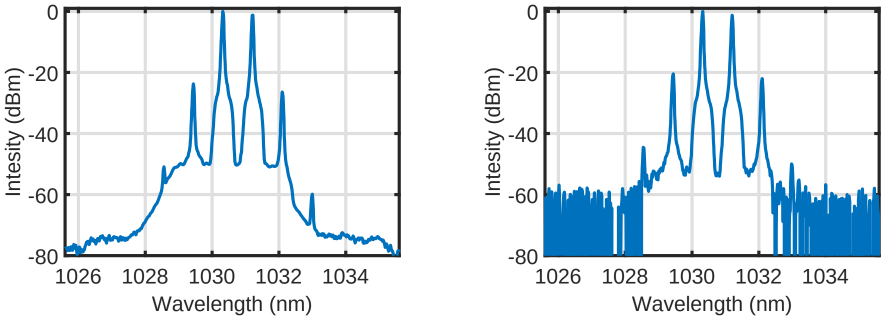

(a) after YDFA2

(b) after EOM

Figure 4.6: (a) Spectrum after amplification process by YFDFA2 and output of AOM: more sidebands are generated in the amplification process due to the FWM. (b) Spectrum after EOM giving the highest spectral contrast, the sidebands are getting more dominant because of FWM.

temporal jitter is 30 ps and rise time is 60 ps. This allows chopping pulses down to 250 ps pulse duration.

The timing of the chopping process is optimized using the sampling scope. The relative delay between EOM and AOM is changed using the DG645, and simultaneously, the temporal profile is monitored by the sampling scope (see Fig. 4.7b). After finding the temporal overlap between the EOM and the AOM and shaping the pulse profile to a flat-top using the AWG of the EOM, the output power of EOM and spectrum were measured (see Fig. 4.6b). The measured low average power of 500 µW can be explained due to the high insertion loss of approximately 12 dB of the EOM and 0.05% duty cycle.

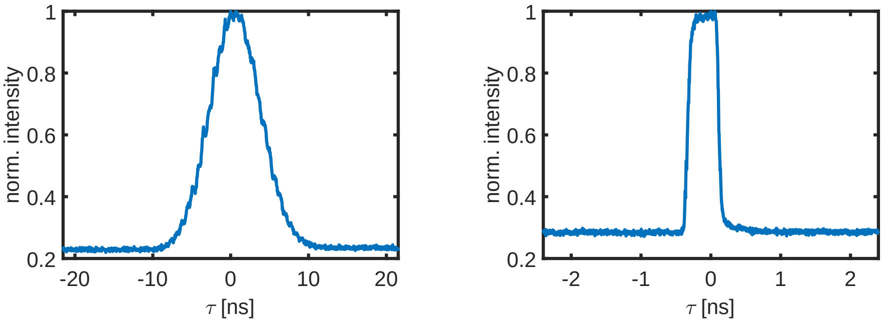

(a) after AOM

(b) after EOM

Figure 4.7: The chopped pulse shapes at the output of (a) the AOM using a setting around 15 ns from the DG645; and (b) the EOM set to 500 ps flat-top using the AWG of EOM.

After achieving the desired pulse duration of several hundreds of picoseconds, the weak signal at the EOM output is boosted by the third fiber amplifier to the nanojoule level to seed the regenerative amplifier in the next boosting stage (YDFA3, see Fig .4.1). By considering the low average power at the output of the EOM and continuously operating pump, it would be expected that a strong amplified spontaneous emission (ASE) would be generated. Therefore, this amplifier must be designed specially. It has the shortest gain fiber length within the amplifiers. The output power of YDFA3 is plotted as a function of the diode pump current (see Fig. 4.8a). After this amplification stage, pulse energies up to 25 nJ at a repetition rate of 2 MHz were demonstrated, which is in the acceptance range (few nanojoules) of the commercial regenerative amplifier. Besides, pump current dependent spectra are acquired, summarized in Fig. 4.8b, the number of spectral lines increases with increasing diode pump current, generated by the FWM in the single-mode fiber (SMF).

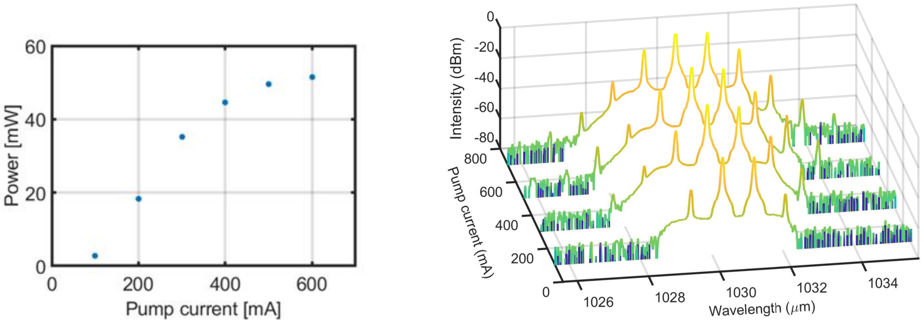

(a) Pump current vs. output power.

(b) Spectra for different pump current

Figure 4.8: a) Output power as a function of pump current, with 2 MHz repetition rate and up to 25 nJ pulse energies are achieved. b) Correlated spectra for different pump current.

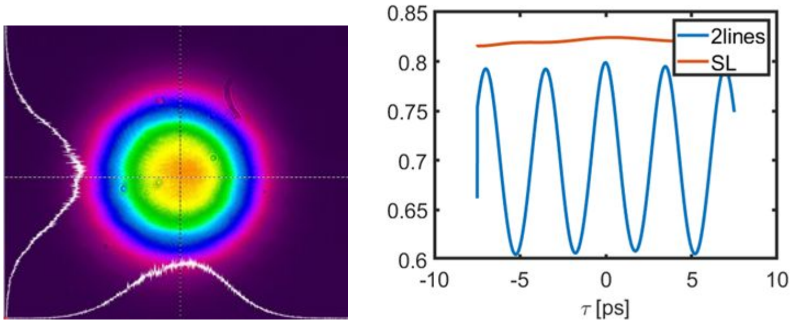

(a) Beam Profile.

(b) Beat Signal.

Figure 4.9: Output of front-end (after YDFA3) a) beam profile: 1.66×1.66 mm^2 at e^{-}2-radius. b) Beat signal: measured by the autocorrelator (AC).

Both controlling the number of spectral lines and investigating the THz generation relationship are critical for optimal THz output. The contribution of the spectral lines to THz generation can be explained in a temporal domain more illustratively. The spectral lines generate a modulation in the temporal domain at the difference frequency of both spectral lines, which coherently drives the THz generation. Since the THz generation is a second-order effect, the process is proportional to the contrast and intensity of the modulation. Putting more spectral lines with the right phase, ideally compressed, increases the modulation's intensity and steepness in the temporal domain and makes it more efficient. The final output (beam profile and beat signal) of the system is shown in Fig .4.9a.

In order to check the beat frequency which is actually derived from the two initial CW seed lasers, the autocorrelation traces with and without tunable CW laser were measured (Fig.4.9b). Clearly, no beating is present when the tunable CW laser was switched off. In addition, the spectral behavior at different positions along the amplifier chain was measured. The results are shown in Fig. 4.10, where no sidebands are visible when the tunable CW laser was switched off. This result supports the hypothesis that FWM in an SMF is present.

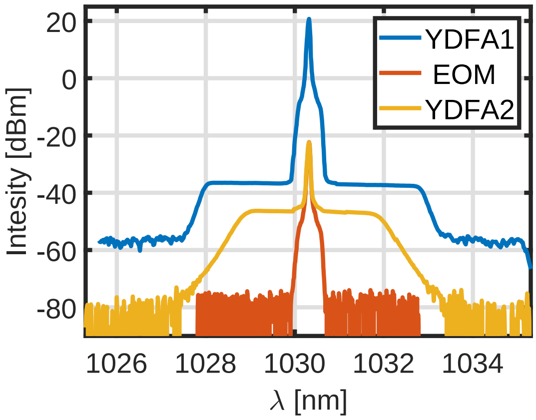

Figure 4.10: One of two CW-lasers (tunable laser) is turned off. The spectral profile after the first amplifier (YDFA1), AOM and second amplifier (YDFA2).

To characterize the pulse shape, two different methods have been utilized. The first method is a straight forward method, namely using a fast sampling scope. The output of the front-end is connected to the device, which is triggered by the DG645, and the pulse shape trace is measured (see Fig. 4.7b).

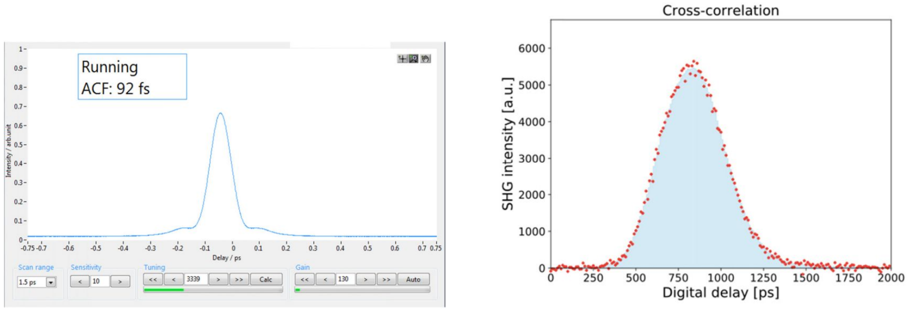
Running
ACF: 92 fs

Scan range 1.5 ps
Sensitivity 10
Tuning 3339
Gain 130

(a) Compressed output of MLL.

(b) X-correlation signal

Figure 4.11: a) The autocorrelation trace of the mode-locked laser after the compressor. b) The cross-correlation signal between the compressed output of the modelocked laser and the front-end.

Another approach has been used besides this simple method, namely the cross(x)-correlation between the front-end and the compressed output of the mode-locked laser (MLL). The MLL pulses are compressed down to ∼64 fs (Fig. 4.11a). These pulses are overlapped (noncollinear) with the output of the front-end in a nonlinear crystal (BBO), and a photodiode is used to detect the generated second harmonic signal. The temporal envelope of the front-end laser is delayed electronically with respect to MLL-laser. Using the fact that both choppers: AOM and EOM are triggered by the same DG645, which is externally triggered by the repetition rate of MLL-laser (70 MHz see. Section 4.4.1). By changing the trigger times of both choppers, the pulses are delayed relative to each other. The minimum delay step can be set as small as 1 ps. An example of this cross-correlation method is given in Fig. 4.11b. In a final check of the system presented in Fig. 4.1, another amplifier (YDFA4, not shown) is added into the amplifier chain to investigate the effect between the number of spectral lines and pump current. As shown in Fig. 4.12b, the spectrum is broadened from 1017-1045 nm. However, the contrast between the main lines decreases since most of the energy is transferred to the sidebands. After demonstrating the possibility of further spectral broadening using YDFA4, this amplifier is removed. Note: the next amplifier stages (regenerative and four-pass amplifier) cannot support the bandwidth generated by the YDFA4. Therefore it is not helpful for the THz experiments.

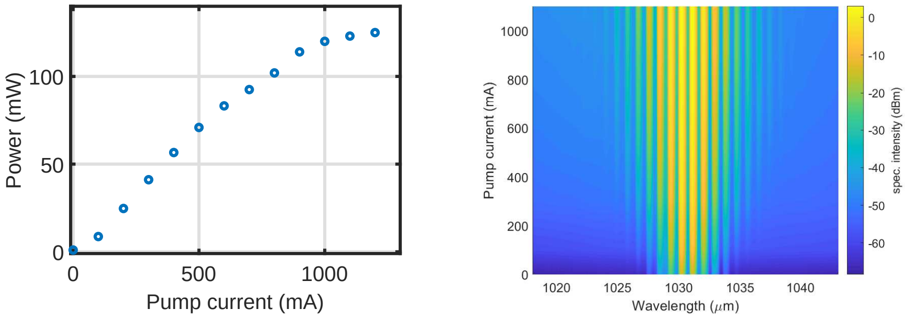

(a) Pump current vs. output power.

(b) Spectra for different pump current

Figure 4.12: a) The output power of YDFA4 as a function of pump current: up to 60 nJ pulse energies achieved. b) The spectral profile for different pump currents. The number of lines increases with the pump current.

In summary, a laser front-end was specially developed for narrowband THz generation, which has the following specifications:

- It consists of narrow spectral lines, whose number can be varied by the pump current, and whose separation can be varied continuously.
- Pulse durations down to 250 ps can be adjusted, with a possibility to shape the temporal profile.
- Pulse energy of several nanojoules is generated at the repetition rate of 2 MHz.

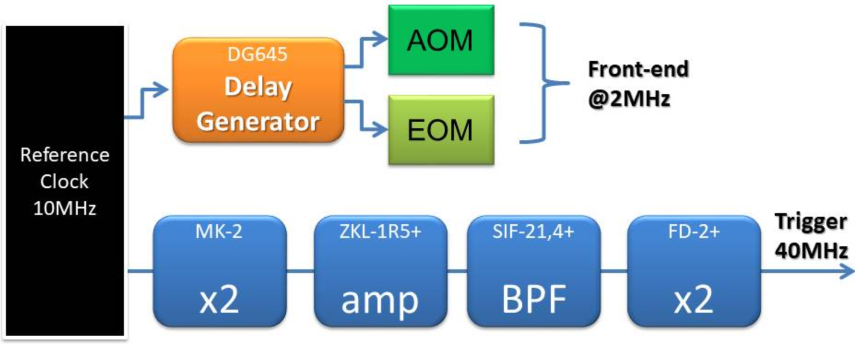

Figure 4.13: Generating of the trigger signal for both the front-end and the regenerative amplifier.

4.2 REGENERATIVE AMPLIFIER (RA)

The complete amplifier chain consists of the front-end (Section 4.1), then a regenerative amplifier (RA), and finally, a home build four-pass amplifier. In this section, the RA is discussed, which boosts the pulse energies, from several nanojoules with hundreds of picosecond pulse duration at 2 MHz repetition rate, to a few millijoules. For this purpose, a commercial RA (*Amplitude*) is utilized, which can be seeded at 1030 nm with a bandwidth of 6 nm and a repetition rate of 42.5 MHz. Since the amplifier is a commercial system, it will not be discussed in detail here. However, this laser needs to be integrated into the timing system of the complete laser.

The RA is designed to be seeded between 30 and 50 MHz. Under normal operation mode, it would receive this signal from a photodiode at the entrance, which detects some leakages of the seed laser, so that the RA is synchronized to the seed laser. However, in the current configuration, the home-built multi-line front-end needs to seed the RA, which can be operated maximal at 2 MHz given by the maximum chopping rate of the EOM (see Section 4.1) and therefore, another trigger signal must be found. The new trigger signal must be in the RA expected range of between 30 and 50 MHz and synchronized to the front-end laser.

An overview of the timing (trigger signals) system is shown in Fig. 4.13. The new RA trigger signal is generated by the same 10 MHz reference clock, which triggers both optical modulators (AOM & EOM) in the front-end. In this way, the timing between the front-end and the RA is guaranteed. The 10 MHz output of the reference clock is multiplied to 40 MHz using two 2 x-RF-multipliers and an RF-bandpass filter (Fig. 4.13).

After providing the trigger signal, the timing of the Pockel-cell (PC) and the pump diode inside the RA are optimized using an oscilloscope. In this way, the pulses from the 2 MHz-front-end are selected by the change of polarization via activating the PC. The selected pulses undergo several resonator

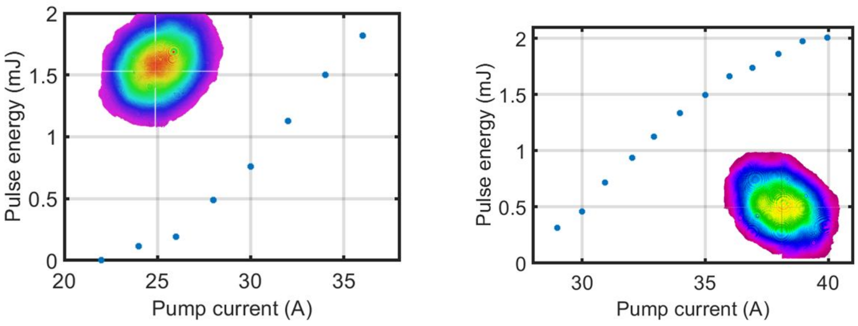

(a) Q-switched

(b) Seeded amplification

Figure 4.14: The laser output energy with respect to the current of the pump diodes for a) Q-switched: unseeded mode and b) seeded amplification. In each diagram, the beam profile of the output pulses are presented.

round trips, pass through the laser crystal and get amplified. The amplified pulse train is observed by a photodiode, which detects leakage in the cavity.

Now, the output pulse energy of the RA was measured as a function of the diode pump current. The pump current was increased in 2 A steps from 22 to 36 A, for two cases. In the first case, the input seed pulses were blocked, and the maximum pulse energy reached was 1.8 mJ at 1 kHz with a shown beam profile at the left, upper corner of Fig. 4.14a. In the second case, the pulse output was measured for fixed seed energy of 6.2 nJ (Fig. 4.14b). Starting with 29 A, the pump current increased to 40 A and the maximum pulse energy of 2 mJ reached at 1 kHz. The pulse width of the PC's trigger signal defines the number of round trips in the cavity. It is chosen in such a way that the photodiode signal is just saturated, and in this way, the output of the RA stays stable even when the seed energy fluctuates.

4.3 FOUR-PASS AMPLIFIER

After the front-end (Section 4.1) and the RA (Section 4.2), the final amplitier stage is a four-pass amplifier (FPA), employed to amplify the pulses up to 20 mJ.

The general layout of this home-built FPA is shown in Fig .4.15. The RA's output is first beam-shaped by a telescope and then sent to a pulse picking Pockel-cell (PC) to reduce the repetition rate from 1 kHz down to 10 Hz. The first half-wave plate (HWP1) and cubic polarizer (PBS1) enable, on the one hand, to vary the input energy and on the other hand, the combination with the Faraday rotator (FR1) protects the RA from any unwanted back-propagating beam. The second polarizer (PBS2) makes sure that the beam, which goes to the PC, is p-polarized (p-pol). When an external electrical field (5.5 kV) is applied on the PC's crystal, the beam's polarization is changed due to the electro-optic effect. When the PC is activated, the polarization of the beam changes to s-pol, which is then reflected by the PBS2. Otherwise, it stays the same and after passing twice through FR1 sent to the beam block.

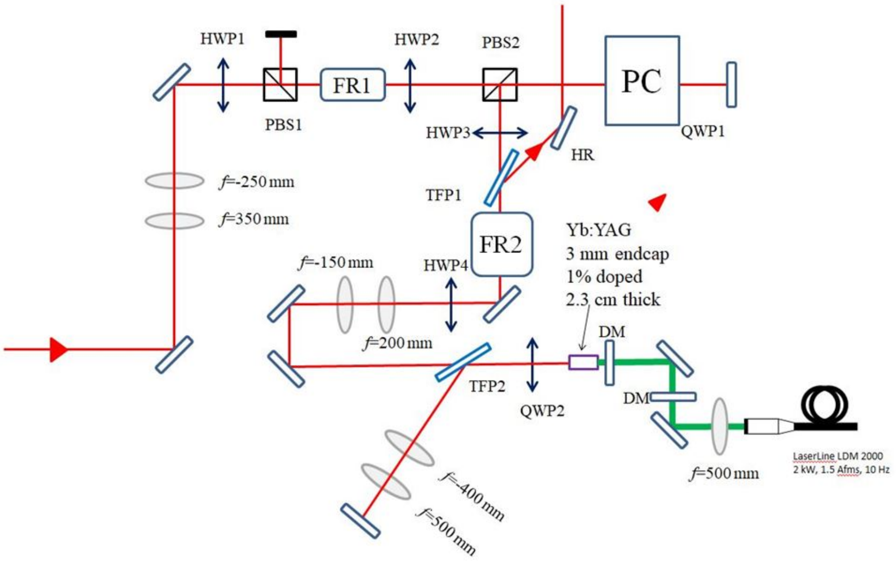

Figure 4.15: The layout of the polarization switched four-pass amplifier.

Using a fast photodiode, which can resolve each pulse in a 1 kHz pulse train, the PC's extraction ratio is optimized by adjusting the trigger timing and the high current. In this way, every hundredth pulse is sent into the amplification, and the rest of the pulses are dumped to a beam block. The polarization of selected pulses is changed to p-pol using HWP3 and go through the thin-film polarizer (TFP1) and FR3, acting as an output coupler for amplified pulses.

Thereafter the pulse rate is reduced from 1 kHz to 10 Hz, the beam size is matched again to the aperture size of the amplification crystal using a demagnification telescope. The pulses make the first pass through the QWP2 and amplifier crystal then are reflected back for a second pass, after which the polarization changes to s-pol and reflected using TFP2. Before the pulses are reflected back for a third and fourth pass, they are sent through a telescope, which compensates for the thermal lensing. After the fourth pass, the polarization is again p-pol. The amplified pulses see a magnification telescope that helps to protect the FR2 by reducing the peak intensity. After the second pass through FR2, the polarization changes to s-pol, and the amplified pulses are coupled out from TFP1.

The gain medium is a 23 mm thick, and 1%-doped Yb:YAG crystal mounted in a water-cooled mount to improve the extraction efficiency by cooling it down. A fiber-coupled diode array provides pumping with center wavelength at 940 nm and up to 2 kW of average power. The pump laser is pulsed at a duty cycle of 1.5%. Pumping optics are adjusted to achieve a 2.5 mm diameter pump size in the gain medium. The maximum pulse energy of 21 mJ has been achieved at a pump voltage of 4.1 V (max. 5 V). The voltage is not increased further to avoid any damage.

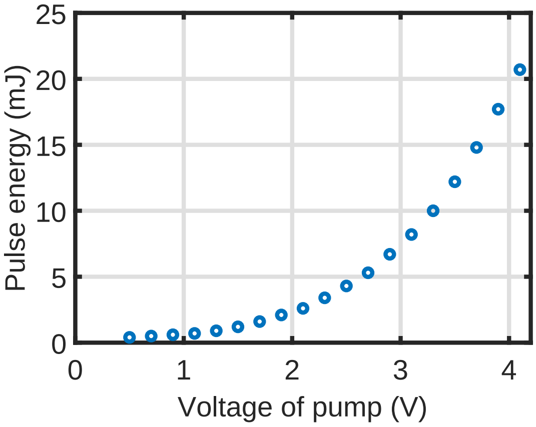

Figure 4.16: Amplified laser pulse energy as a function of the pump voltage of the pump diode.

Finally, a DG645 is externally triggered by the RA at 1 kHz, and is divided down to 10 Hz to provide the trigger pulse for the PC module and the pump-diode. In this way, the timing is guaranteed between the RA and the FPA.

4.4 LOCKING OF LINE SOURCE FOR THE ACCELERATION EXPERIMENTS

Since the generated MC-THz radiation should be used to accelerate the electrons in the LINAC part of the AXSIS project [23], controlling the timing between electron bunches and the MC-THz radiation is very crucial. In this section, improvements to the timing of the line sources used in the front-end (Section 4.1) are discussed in detail.

A highly stabilized, single-frequency CW laser (SL) is employed as a reference for the timing. SL is locked to an ultra-stable reference cavity, which ensures a frequency drift as low as kHz per day [10]. The output of the SL is split into two parts; one arm is sent to seed the multi-line laser source (see Section 4.1), the other arm is used for timing. The aimed THz frequencies range spans from 100 to 600 GHz, mainly 300 GHz, which will be driven coherently by temporal beat modulation of SL and tunable laser(TL). Since this frequency separation is too large to be locked both lasers directly, a frequency comb of a home-built mode-locked laser (MLL) [17] is utilized to ensure the locking of both lasers.

As summarized in Fig. 4.17, the following steps need to be accomplished for the timing:

- stabilization of MLL's repetition rate
- stabilization of MLL's carrier-envelope offset frequency f_{CEO} by locking MLL with SL, and making frequency comb (FC) from MLL.
- locking TL to FC

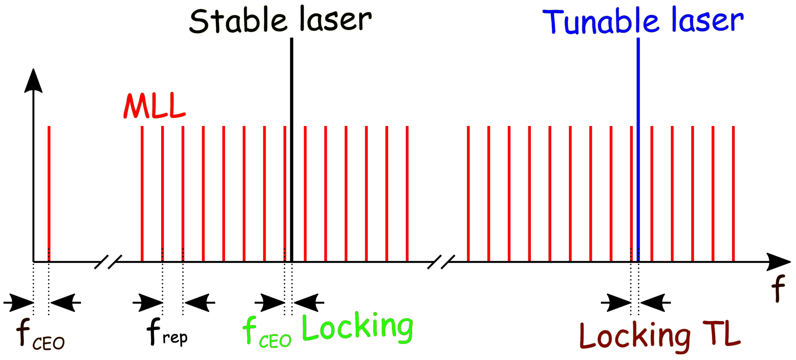

Figure 4.17: The basic concept for the locking mechanism: first, the repetition rate (f_{rep}) of the MLL is stabilized, then it is locked to the stable laser which ensures its carrier-envelope offset frequency (f_{CEO}) stabilization, finally the tunable laser (TL) is locked to the f_{rep}- and f_{CEO}-stabilized MLL.

4.4.1 *Repetition Rate Locking of MLL*

In this section, it is explained how the f_{rep} of the MLL is realized.

The output of a mode-locked laser is a train of ultra-short pulses corresponding to a phase-stable superposition of multiple longitudinal modes of the laser resonator. The frequencies of the longitudinal modes of a diffraction-limited laser are equidistantly separated by the laser's repetition rate (f_{rep}). In order to use this mode-lock laser for locking, it must be elevated to a frequency comb. This requires a stable repetition rate (f_{rep}) and carrier-envelope offset frequency (f_{CEO}).

The laser's repetition rate is determined by the optical path length of the cavity, which is in this particular case 70 MHz. This value can vary depending on thermal changes and vibrations. To minimize such effects, the MLL is put in a laser box in a temperature-stabilized lab environment. The last mirror of the cavity is mounted on a piezoelectric stage (PZT; *Piezosystems Jena PX38*) to actively control the optical path by applying a voltage on PZT. It has a travel range of 38 μm, which allows path-length changes that are double of this amount since it is used in combination with a reflecting mirror. Thus, a frequency drift of up to 1.2 kHz can be actively compensated.

The repetition rate locking mechanism is illustrated in Fig. 4.18.

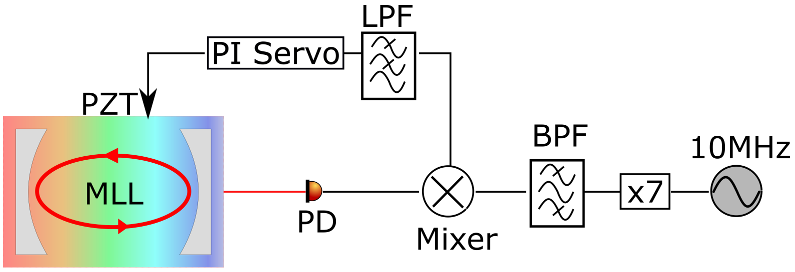

Figure 4.18: Schematic of the feedback loop for repetition rate locking.

The stabilization of the MLL's f_{rep} is realized by actively changing the cavity-length using the PZT. The PZT is controlled by a proportional-integral

(PI)-servo controller (*Newfocus LB1005*) with an error signal generated by mixing MLL's f_{rep} and a reference signal at 70 MHz.

A small leakage of the MLL is detected by a photodiode, which converts the optical into RF-signal. This is filtered by a bandpass filter (RF-BPF) and amplified to feed a phase detector. The reference signal is provided by an oven-controlled crystal oscillator (OCXO; *InWave B-110*), which runs at 10 MHz. Using an RF-multiplier, it is increased to 70 MHz, and fed to the phase detector. The error signal is generated by filtering the phase detector's output using a lowpass filter (RF-LPF).

A frequency counter (*K+K+FXE*) is used to quantify the performance of f_{rep}-locking; a long term stability measurement has been performed above 24 hours. The maximum acceptance frequency of this counter is 65 MHz, which is just below the repetition rate. Consequently, the detected signal from the photodiode is divided down to 2 MHz by DG645 and fed into the frequency counter. The measurement is shown schematically in Fig. 4.19

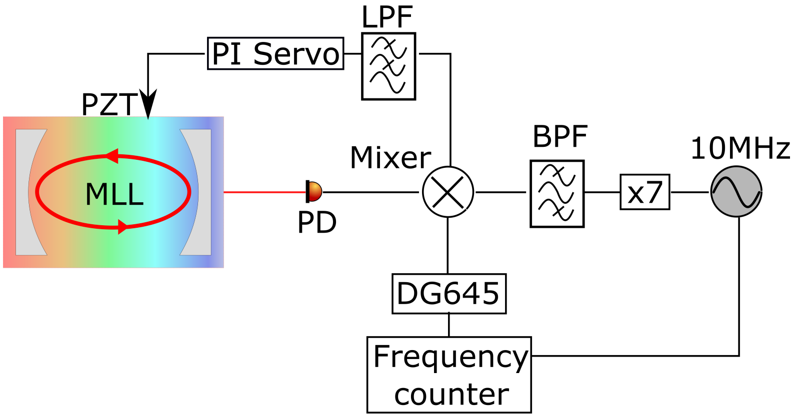

Figure 4.19: Experimental setup for determining residual repetition rate drifts using a frequency counter.

As shown in Fig. 4.20, if the locking is not activated, the value is drifting over time. After activation of the locking, it stays stable. The repetition rate signal is used as an external trigger signal for the delay generator (DG645), which triggers all the components in the laser line source and operates over several months.

The stability can be assessed via the normal distribution over all counts from the 24 hours measurement, which gives a mean value at 70 MHz with a standard deviation of 6.2 mHz.

Additionally, the phase noises for both cases are measured using a signal source analyzer, which indicates roughly a 25 Hz locking bandwidth (see Fig. 4.21).

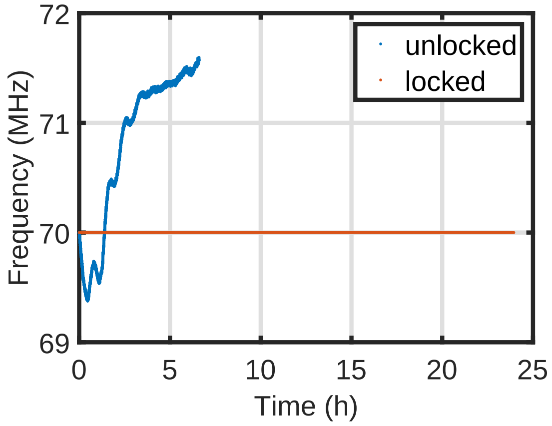

Figure 4.20: Long-term repetition rate stability results for stabilized (red) and not stabilized (blue).

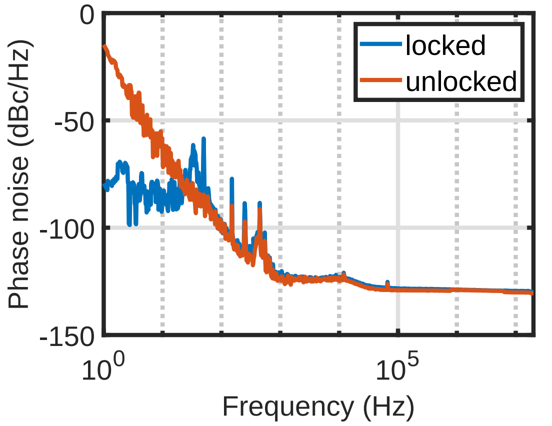

Figure 4.21: Phase noise as a function of the frequency for free-running and f_{rep}-locked MLL.

4.4.2 *Locking the carrier-envelope offset frequency of MLL*

After demonstrating the long-term stabilization of the MLL's f_{rep}, the next step is locking one of the teeth of the MLL with the SL to ensure a f_{CEO} stabilization. This means having a frequency comb.

The locking scheme is depicted in Fig. 4.22.

The locking mechanism consists of two tuning procedures - first, a coarse and slow tuning using an isochroic wedge-pair. Second, a fine and fast tuning by employing an acousto-optic frequency shifter (AOFS).

The isochronic wedge-pair (see Fig. 4.23) has been specially designed using two different materials (N-LASF31A and N-SF6) which have similar group indices but different group delay dispersion.

The wedge-pair is mounted on a motorized translation stage (*V-522.1AA*) into the laser cavity by moving it perpendicular to the optical beam's propagation direction, the ratio of the materials that the beam goes through

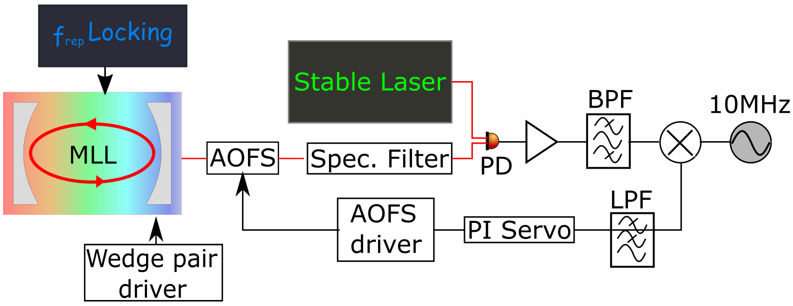

Figure 4.22: Locking the carrier-envelope offset frequency using a stable laser.

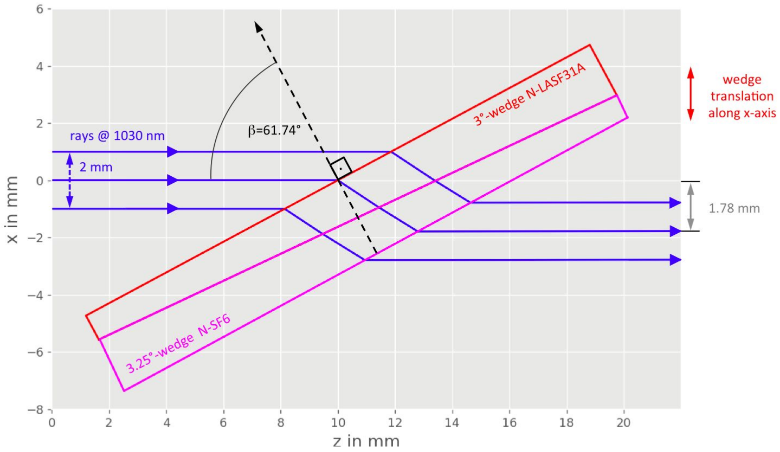

Figure 4.23: Specially designed isochronic wedge-pair [37] for course tuning of f_{CEO} .

changes. Due to the difference in group-delay dispersion of the materials, this imprints a change of the f_{CEO} of the MLL.

Before measuring the wedge pair's influence on the f_{CEO}, the change of f_{rep} due to the relative displacement of the position of the wedge-pair is measured using a signal analyzer (*N9000A CXA*) for *not* f_{rep}-stabilized MLL. The results are depicted in Fig. 4.24a. It stays below 10 Hz/mm, and it remains constant when the f_{rep}-locking is activated.

Afterward, to characterize the influence of the wedge-pair on the f_{CEO}, another scan has been carried out, in which the beat signal between MLL and SL is measured as a function of wedge-pair's position. Since MLL is a broadband laser, its output is filtered by a BPF at 1.03 μm (around the central wavelength of SL) before mixing it with SL. The generated beat signal is monitored by the signal analyzer. In Fig. 4.24b, the peak position of the beat signal is plotted against the wedge-pair's position. MLL runs at a f_{rep} of 70 MHz. Therefore, it is enough the cover half of f_{rep}, namely from 0 to 35 MHz) to move one of the teeth vicinity of SL, which can be achieved by a 1 mm displacement of the wedge-pair.

Direct f_{CEO} locking with the wedge-pair was not possible since the bandwidth due to the stage movement is insufficient to compensate for rapid CEO-frequency fluctuations. However, it moves the beat signal into the operation of the AOFS (*AA.MT110*), which can then be used to lock the f_{CEO}.

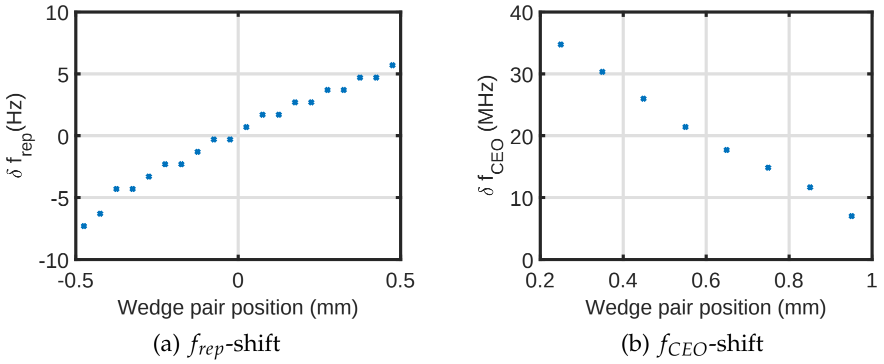

(a) f_{rep}-shift

(b) f_{CEO}-shift

Figure 4.24: Course tuning by the isochronic wedge-pair: (a) repetition rate and (b) beat frequency as a function of position of the isochronic wedge-pair.

In AOFS, a density modulation is generated by acoustic waves in an acusto-optical material, which acts as a grating. So, the diffracted first-order optical beam frequency is shifted by this acoustic carrier frequency [25].

A voltage-controlled oscillator (VCO) is a driver for the AOFS. The frequency shift and the transmission is measured as a function of applied voltage (see Fig. 4.25)

The best operation range of the AOFS at ∼110 MHz ± ∼10 MHz around 3 V.

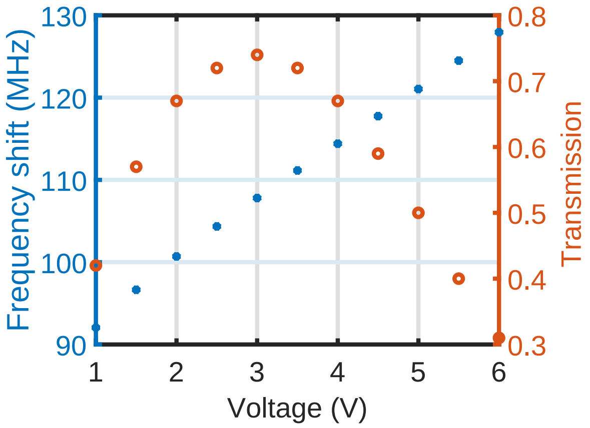

Figure 4.25: The frequency shift and the transmission after AOFS as a function of applied voltage from the VCO.

For the locking, the PI-servo controller's output set around 3 V and generation of the error signal for the PI-servo controller is illustrated in Fig. 4.22. The same OCXO from the previous section [Ref] provides the reference signal at 10 MHz. Firstly, the heterodyne signal is moved to 10 MHz using the wedge-pair. By mixing this signal with the reference signal, an error signal is generated, fed to the PI-servo controller. The output of the PI-servo controller is connected with the driver of the AOFS.

By activating the PI-servo controller, the f_{rep}-stabilized MLL is locked to the SL for 10 min (see Fig. 4.26)

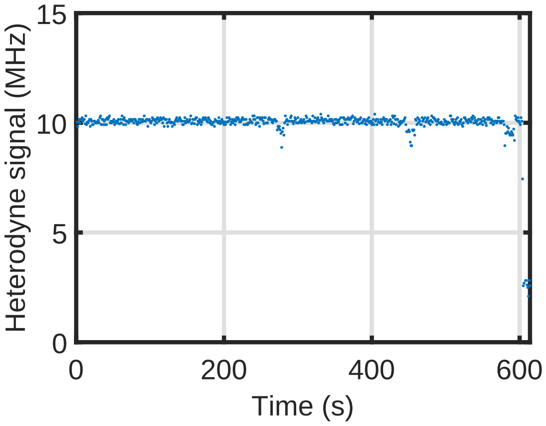

Figure 4.26: The f_{CEO}-stabilized MLL. The heterodyne signal before mixer.

4.4.3 *Locking the tunable laser to the frequency comb*

After stabilizing the f_{rep} and the f_{CEO} of MLL, quasi having a frequency comb, the next step is locking the TL to the frequency comb.

The locking mechanism is shown in Fig. 4.4.2. Notably, it is similar to the case of the f_{CEO}-locking, as described in Section 4.4.2.

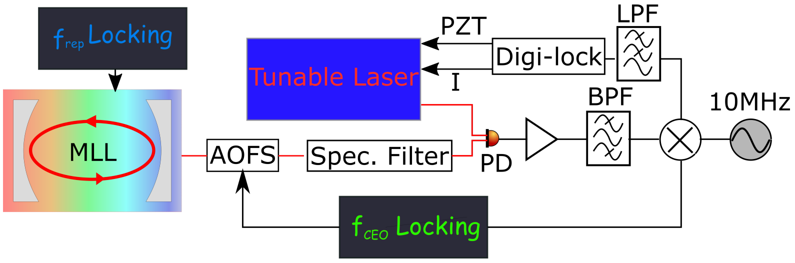

Figure 4.27: Looking of a tunable single frequency laser.

A heterodyne signal between tunable laser and ML-laser must be generated for the locking.

In order to increase the signal to noise ratio, a BPF for the MLL is required. The big difference compared to the f_{CEO}-locking, the central wavelength of the TL is tunable. Therefore a tunable BPF is built, consisting of a grating and an adjustable collimator working a slit. The spectral components of the MLL are spatially separated by the grating, from that an adjustable collimator converts the desired part of the spectrum. By combining this with the TL, a heterodyne signal is generated, mixed with the reference signal from the OCXO to create the error-signal. The TL has a built-in locking module (*Digi-Lock*). It has a coarse and fine-tuning, too. The coarse tuning uses a PZT, which rotates a grating in the laser module, and the fine-tuning changes the current of the pump diode.

In Fig. 4.28 illustrated how first the f_{rep} stabilized MLL to the SL(blue), and subsequently, the TL to the frequency comb (red) is locked.

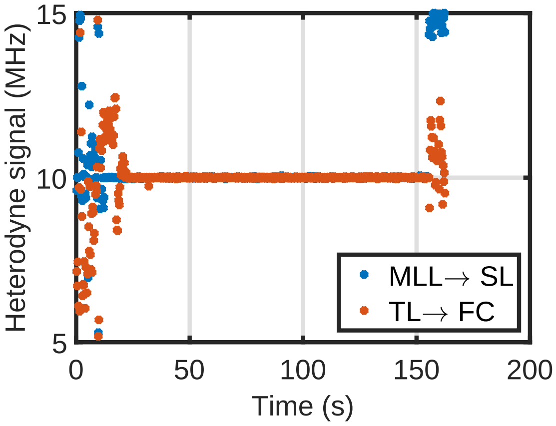

Figure 4.28: Locking the lines: locking of the f_{rep} stabilized MLL to the SL (red) and the TL to the frequency comb(FC) (red), respectively.

In conclusion, first, the long term f_{rep} and f_{CEO}-stabilization of a home-built MLL then using its locking of both CW-lasers have been demonstrated. In the future, the locking performance will be improved.

5

MULTI-LINE THZ EXPERIMENTS

So far, the laser-driven narrowband MC-THz generation based on difference frequency generation (DFG) is one of the most promising approaches to reach the requirements of the MC-THz source for the AXSIS project (Chapter 2). However, the demonstrated optical-to-THz conversion efficiencies (CE) of 0.24% is still too low to be practical, even using high-energy joule-class lasers [21]. Therefore, a so-called multiline laser is specially developed (see Chapter 4), whose spectral and temporal shape can be modified. Numerical simulations using such a driving laser have demonstrated high-efficient MC-THz generation [35, 42]. As explained in detail in Chapter 4, the laser consists mainly of two narrow-spectral lines whose separation can be adjusted for the desired THz-frequency with variable pulse duration from 250 ps and upwards.

In this case, the special tailored optical pulses are sent into a periodically poled nonlinear crystal. When the phase-matching condition is fulfilled (Eq. (2.10)), the THz radiation at the difference frequency of the narrow spectral line is generated. The poling period of the crystal determines the phase-matched frequency (Eq. (2.12)). This process can be understood in both the spectral and temporal domains. In the spectral domain, the optical pulse has only the spectral components that are down-converted to the THz frequency using the quasi-phase-matching technique. In the time domain, the narrow spectral lines generate an optical pulse sequence which drives the coherent THz generation.

In this chapter, for the first time, optical pulses from the multiline laser are used to investigate the performance of MC-THz generation. The initial experiments used the lower pulse energy from the regenerative amplifier at a repetition rate of 1 kHz energy: the investigated parameters include phase matching, THz bandwidth, number of optical spectral lines and optical pulse duration (Section 5.1). In this case, the higher the repetition rate makes it easier and quicker to scan the various parameters. Afterwards, the optical pulses were further amplified in a four-pass-amplifier (Section 4.3) to tens-of-millijoule levels to examine the laser energy-dependent MC-THz generation and the conversion efficiency (Section 5.2) in the various MgO-doped PPLN crystals (see Table 5.1). Next, a Rb:PPKTP crystal is tested as a comparison to MgO-doped PPNL (Section 5.3). Finally, the results are discussed and summarised in (Section 5.4).

Table 5.1: List of the periodically poled nonlinear crystals that were used for the narrowband MC-THz generation at RT and CT. AS - Aperture size, L - length, PP - poling period, ν_0 - phased matched.

No.	Crystal	AS (mm^2)	L (cm)	PP (μm)	ν_0 (THz)
1	MgO:PPLN	4×4	2	400	∼0.29
2	MgO:PPLN	4×4	4	400	∼0.29
3	MgO:PPLN	4×4	2	212	∼0.53
4	MgO:PPLN	3×3	2	212	∼0.53
5	MgO:PPLN	4×4	4	212	∼0.53
6	Rb:PPKTP	1×2	1.55	300	∼0.5

5.1 PRELIMINARY TESTS ON PPLN USING THE LOW ENERGY OPTICAL MULTILINE LASER AT 1 KHZ

A number of critical parameters are investigate on PPLN crystals at CT using the output of the regenerative amplifier (∼1 mJ at 1 kHz, Section 5.1), using crystal No. 2 & 3 (Table 5.1). Since it has a higher repetition rate compared to the final amplification stage, it is more convenient to scan a range of parameters.

5.1.1 *Phase matching frequency and bandwidth*

Since the multiline laser consists of narrow spectral lines, its very crucial to set the wavelength separation correctly to optimize the MC-THz generation. The wavelength separation is adjusted by tuning the central wavelength of the tunable laser (TL). In order to measure the generated MC-THz signal as a function of wavelength separation, the same experimental setup as shown in Fig. 5.4 was utilized. The central wavelengths of both CW seed lasers were measured using an optical spectrum analyzer (OSA; *AQ6315A, YOKOGAWA*). This OSA has a spectral resolution of 50 pm. As an example, the wavelength separation was tuned to match the phase matching condition for crystals No. 3 and No. 2 (Table 5.1). The maximum MC-THz energy was obtained at wavelength separations of 1.88 nm and 1.01 nm with relative acceptance bandwidths (FWHM) of 1.47% and 1.38% for the crystals No. 3 and No. 2, respectively (Fig. 5.1a) and results in Table 5.2). Both relative bandwidths are roughly 38% bigger than the value from Eq. (2.15). A possible reason for this discrepancy would be the inclusion of 3^{rd}-order and higher dispersion of the two-line laser.

At the optimal wavelength separation, a Michelson type THz interferometer was utilized to measure the delay-dependent interferometric autocorrelation trace: as an example, the trace of the crystal No. 2 is given in Fig. 5.1b, from which the Fourier transform was calculated. In this case, the measured central frequency of 286.3 GHz with a bandwidth of 1.5 GHz (∼ 0.5%) com-

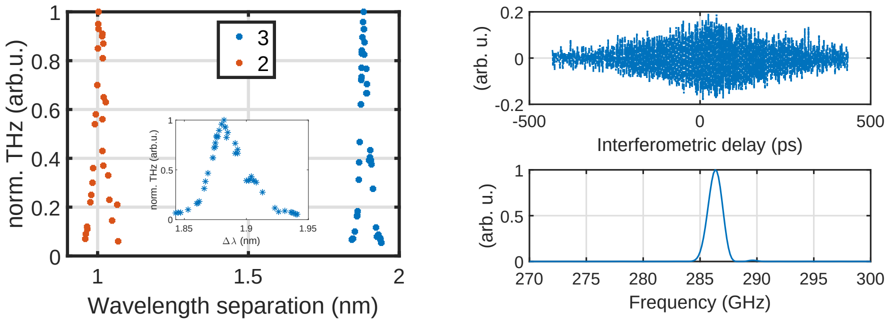

(a) (b)

Figure 5.1: a) MC-THz generation dependence on wavelength separation: crystal No. 3 ($\Lambda = 212\,\mu\text{m}$, $L = 2\,\text{cm}$) (red, dots), and crystal No. 2 ($\Lambda = 400\,\mu\text{m}$, $L = 4\,\text{cm}$) (blue, dots). The insert is crystal No. 2 expanded. b) The measured delay-dependent interferometric autocorrelation trace for crystal No. 2 (top). From this trace the Fourier transform was calculated (bottom). The measured central frequency is 286.3 GHz with a bandwidth of 1.5 GHz.

Table 5.2: Comparison of the expected relative bandwidth $\Delta\Omega/\Omega_0$, Eq. (2.15), with the measured relative acceptance bandwidth at two different phase matched frequencies.

Crystal	$\Delta\Omega/\Omega_0$ (%)	$\Delta\Omega^{Meas}/\Omega_0$ (%)	ν_0 (GHz)
No. 3	1.06	1.47	285.6
No. 2	1	1.38	531.7

pares well with the central frequency (285.6 GHz) of the wavelength tuning curve (Fig. 5.1a, red-curve). Although the central frequency matches well with the result from the wavelength tuning, its bandwidth is narrower. For long pulses, the number of THz oscillation exceeds the poling number of the crystal, which leads to a narrower bandwidth.

5.1.2 *Influence of the number of spectral lines on MC-THz generation*

One of the critical parameters for the multiline-THz experiment is the number of spectral lines of the optical input beam. In this section, the influence of the number of spectral lines on MC-THz generation is investigated.

As explained in detail in Section 4.3, increasing the pump current from 100 mA to 300 mA, in the last amplifier YDFA3 in the front-end of the multiline laser, increases the number of spectral lines (Fig. 5.2(b)). However, the generated MC-THz, measured as a function of laser input energy, was greater for the lower pump current, where effectively only two spectral lines are present (Fig. 5.2(a)). The spectrum of the optical laser was also measured after MC-THz generation (Fig. 5.2(c)). The results are counter-intuitive at first glance since it is expected to have more MC-THz yield when more spectral

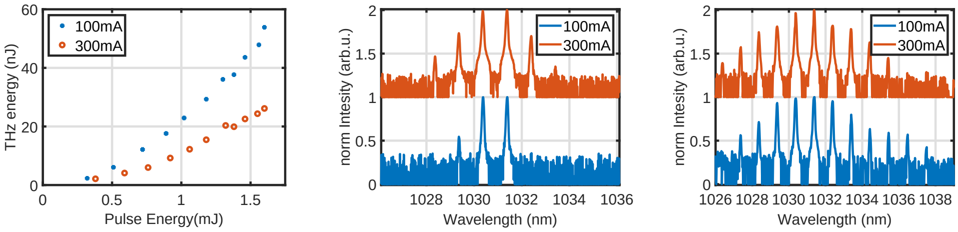

Figure 5.2: a) The input laser energy-dependent MC-THz yield for different starting number of spectral lines. Optical spectrum at (b) before and (c) after the interaction. Low pump current in YDFA3 leads to a fewer number of lines (see (b), which after the interaction gets broader than in the case of higher pump current due to more efficient MC-THz generation.

lines are present, as predicted by Ravi et al. [35]. However, the opposite is true (Fig. 5.2), which is related to the generation process of the new spectral lines in the front-end of the multiline laser. Additional spectral lines were generated in single-mode fibers by the third-order nonlinear effect, namely by the four-wave mixing (FWM), which leads to higher-order spectral phase contribution. This leads to less efficient MC-THz generation. This effect is more critical for longer crystals; the longer the crystal is, the more sensitive the process is to phase-matching narrowing.

The optical spectral results support this evidence, too. As shown in Fig. 5.2 (c), the spectrum of the low pump current gets broader after the interaction compared to the case with the higher pump current, owing to a more efficient THz generation.

These results demonstrate that the generation process of spectral lines is very critical for the MC-THz generation. Having more spectral lines makes the process even less efficient when the spectral lines are generated through the high-order nonlinear effects. The numerical simulations predict that by compensating this higher-order nonlinear spectral phase, the efficiency could be increased with even more than in two lines [42].

5.1.3 *Influence of the pulse duration on the MC-THz generation*

Another critical parameter for the MC-THz generation is the pulse duration of the laser, which allows varying the intensity without changing the fluence. As described in detail in Section 4.1, the laser pulse duration can be varied using the AWG of the EOM with the smallest pulse duration of 250 ps.

The pump current of YDFA3 was kept low at 100 mA to have as less spectral lines, and the laser input energy was fixed to $\sim$1.2 mJ, while the pulse duration was varied from 250 ps to 1 ns. The MC-THz yield was measured as a function of laser pulse duration (Fig. 5.3). On the left side of the y-axis, the MC-THz yield for different pulse durations is plotted. On the right side of the y-axis, the ratio between the temporal walk-off length (Eq. (2.19)) and crystal length is plotted for different pulse durations. The THz yield drops with increasing pulse duration, which means the MC-THz efficiency is intensity-dependent as predicted for $l_{walkoff} > L_{cry}$ in Section 2.3.

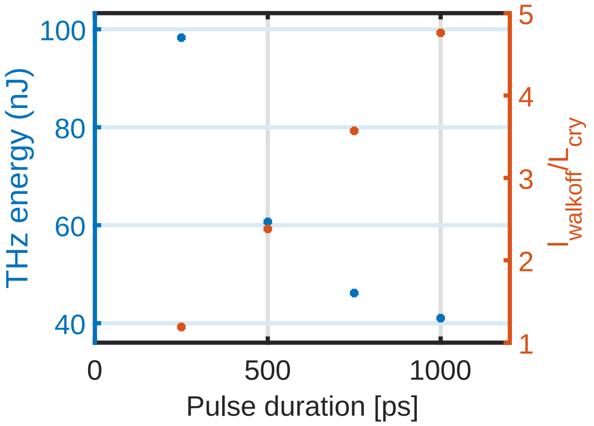

Figure 5.3: The MC-THz yield for different pulse duration at maximum laser energy (left axis). The ratio of walk-off (Eq. (2.19)) to crystal length is also plotted (right axis).

Hence, it is expected to have more MC-THz yield by decreasing the pulse duration further. However, technically, 250 ps was the smallest pulse duration in the current multiline laser source, so further decreases were not possible. Moreover, having shorter pulse durations cause higher nonlinear optical effects such as SPM, which were not taken into account in the analytical model (Section 2.3.2).

5.2 HIGH ENERGY MC-THZ EXPERIMENTS WITH MGO:PPLN USING THE MULTILINE LASER SOURCE

In this section, the output of the four-pass amplifier (FPA) from the multiline laser was used (Section 4.3). The laser system delivers up to 15 mJ pulse energies with a repetition rate of 10 Hz. The MC-THz generation using these pulses was investigated in different periodically poled nonlinear crystals. The experimental setup is illustrated in Fig. 5.4.

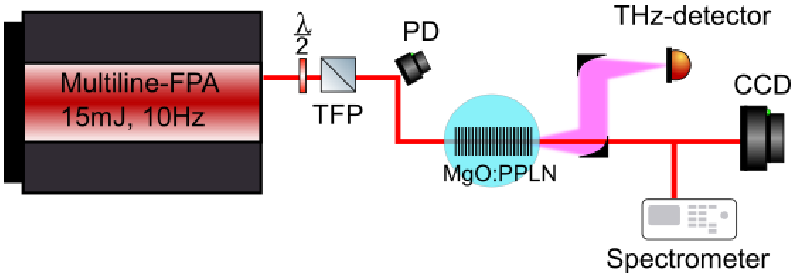

Figure 5.4: Experimental setup for the MC-THz generation using the output of the four-pass-amplifier (FPA) of the multiline laser. TFP - thin film polarizer, PD - photodiode, CCD - Camera.

The laser input energy was adjusted using a half-wave plate (HWP) and a thin-film polarizer (TFP). The HWP is mounted in a motorized stage to control the input energy automatically. Since the output beam size of the

FPA of 0.8×1.1 mm^2 (e^{-2}-radius, Gaussian fit) fits well into the aperture size (4×4 mm^2) of the PPLNs, no beam shaping was required. A photodiode (PD) was used to measure the shot-to-shot pulse energy fluctuations by capturing a small leakage from a mirror. A long-pass filter was mounted on the PD to eliminate any parasitic SHG from the laser. The generated MC-THz was collected and sent onto a pyroelectric THz detector (*Gentec-EO, SDX-1152*) by two 2" gold-coated off-axis parabolic (OAP) mirrors. The MC-THz signal was measured automatically using a DAQ-unit (*NI USB-6229*). The THz detector was covered with a polyethylene (PE) and a teflon shield to protect it from any parasitic radiation, such as residual laser or its 2$^{\text{nd}}$-harmonic.

A small hole in the first OAP mirror allows the separation of the optical laser to be measured using a spectrometer and camera for diagnostic purposes. The crystal's output surface was imaged using a 4 f-imaging system, which increases the laser peak fluences to higher values and stops the scans whenever the photo-reflective effect starts to appear.

For both room temperature (RT) and the cryogenic temperature (CT) scans, the MC-THz radiation takes the same path from the crystal to the detector, so loss sources were as follows: a fused silica vacuum window, two OAP-mirrors, a teflon shield, and a polyethylene cover. The losses vary slightly in both cases because of the temperature-dependent phase-matched THz frequency change. These losses were characterized by a THz-TDS measurement (A.2).

5.2.1 *MC-THz generation at 0.29 THz (crystals No. 1 & 2)*

Measurements were performed using the crystals No. 1 and & 2 (Table 5.1) at RT and CT. These crystals with a poling period of Λ =400 μm is phase-matched for ∼0.29 THz.

After optimizing the wavelength separation (Section 5.1.1) and THz detection, the laser input energy-dependent MC-THz yield is measured in crystal No. 1 at RT for three different pulse durations: 250, 500, and 750 ps. The laser input energy was varied by changing the angle of the motorized rotation stage, and for each angle, 30 data points from the PD, THz detector, and spectrometer were acquired. All results were averaged for each angle and depicted in Fig. 5.5.

All losses from crystal to the detector were considered to calculate the internal THz energy, including the material losses and the Fresnel reflection (43.7%). A maximum internal MC-THz energy of 0.7 μJ was achieved at 250 ps with an input laser energy of 6.2 mJ, which corresponds to an internal optical-to-THz conversion efficiency (CE) of 0.014%. While calculating efficiencies, the Fresnel losses of 13.3% from the laser beam while entering into the crystal were considered. The vacuum windows were AR-coated for NIR. The MC-THz signal below 270 mJ/cm^2 peak fluence was mainly within the detector's noise floor. During the data analysis, the background noise was subtracted from each data point.

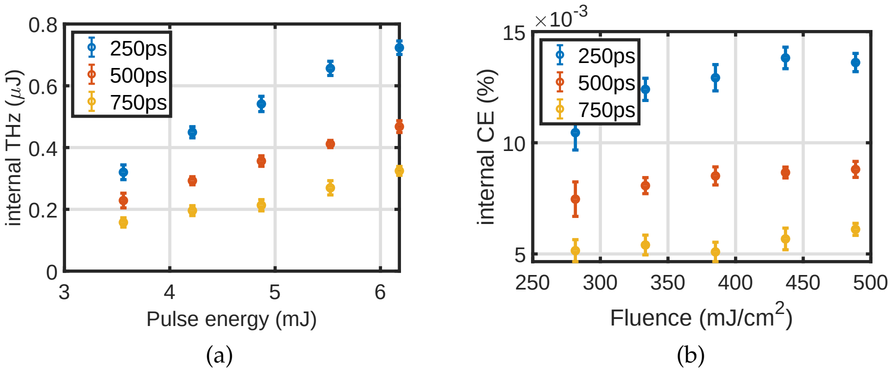

Figure 5.5: RT scans with 2 cm, 400 μm MgO:PPLN (crystal No. 1) using different optical pulse durations: a) The internal MC-THz yield as a function of laser input energy, and b) the internal conversion efficiency as a function of laser peak fluence.

As expected, the achieved efficiencies were low due to the THz absorption. Therefore, the crystal was cooled down using liquid nitrogen ($T \sim 77\,\mathrm{K}$), which reduces the THz absorption coefficient [38]. When the crystal is cooled down, the wavelength separation must be adjusted again to the new phase-matching frequency. The reasons for this change are the temperature-dependent refractive index and the thermal expansion of the crystal, the second effect being a minor effect [27].

After optimizing the wavelength separation, the MC-THz yield was measured as a function of laser input energy (Fig. 5.6). A maximum internal MC-THz of 12 μJ was demonstrated for 250 ps pulse duration, which corresponds to an internal optical-to-THz conversion efficiency of 0.24%. Note: the same CE as reported by Spencer et al. [21].

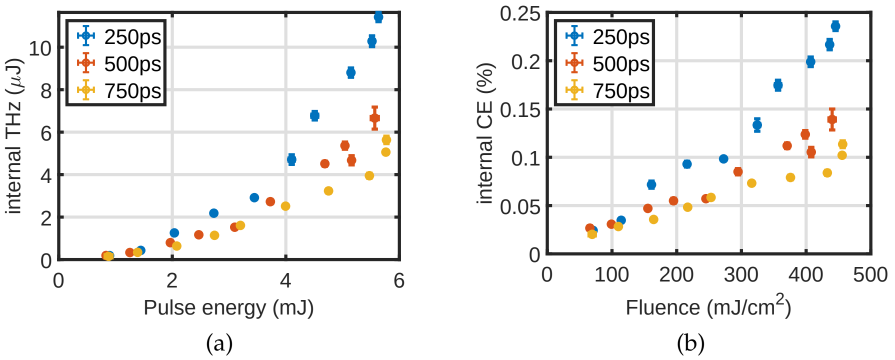

Figure 5.6: CT scans with 2 cm, 400 μm MgO:PPLN (crystal No. 1) using different optical pulse durations: a) The internal MC-THz yield as a function of laser input energy, and b) the internal conversion efficiency as a function of laser peak fluence.

The same scans were repeated with the longer crystal No. 2 to check whether the efficiency could be improved further. The RT results were similarly low, as in the previous case, which supports the argument of a strong limitation due to the high THz absorption in the crystal. Only the results from CT scans were shown in Fig. 5.7. The central wavelength of TL was shifted to 1032.458 nm for the optimal wavelength separation, which means the poling the crystals might be slightly different to crystal No. 1. The conversion efficiencies grow linearly with the intensity as predicted by the analytical description (Eq. (2.20)) and the highest efficiencies of 0.49% was reached for the shortest pulse duration of 250 ps at the maximum laser peak fluence of 390 mJ/cm^2. Note: In Fig. 5.7b, the conversion efficiencies are still growing linearly.

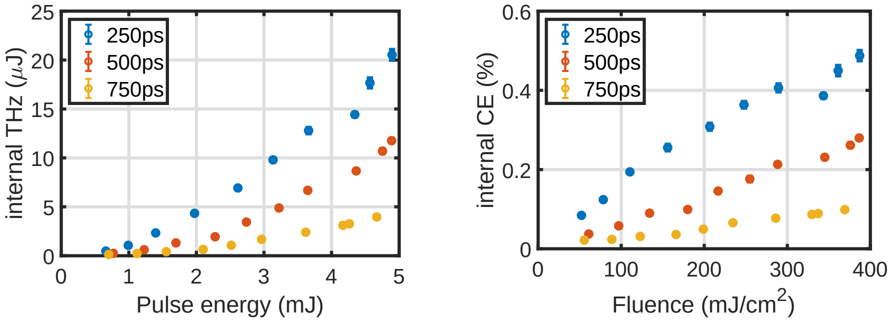

(a) (b)

Figure 5.7: CT scans with 4 cm, 400 μm MgO:PPLN (crystal No. 2) using different optical pulse durations: a) The internal MC-THz yield as a function of laser input energy, and b) the internal conversion efficiency as a function of laser peak fluence.

The analytical solution does not include the effects such as the pump depletion, cascading and SPM. Therefore, a quantitative description requires numerical simulations, which was performed for a similar case for Fourier limited pulses with purely two-spectral lines [42]. The predicted efficiency was around 1%. Possible reasons for the lower efficiency might result from the multiline laser having more than two pure (Fourier limited) spectral lines. In Section 5.1.2, it was demonstrated that more spectral lines reduce the efficiency. Furthermore, the PR-effect, which is not considered in the simulations, also reduces the efficiency.

In addition to the laser input energy-dependent MC-THz yield, the optical spectra were measured after the MC-THz generation. As an example, the result from the crystal No. 2 at CT for the pulse duration of 250 ps are shown in Fig. 5.8a. A clear energy-dependent spectral broadening is visible, which is an indication of cascaded usage of optical pump photons. Since we are dealing with a narrowband multiline laser source, discrete new spectral lines are generated in the broadening process, which differs from the optical rectification with a compressed pulse (see Fig. 6.5c). In the latter case, the broadening happens continuously since all spectral components within its bandwidth can contribute to the THz generation at the time same time. In cascaded effect, the the Manley-Rowe limitation is avoided, as explained in Section 2.5.

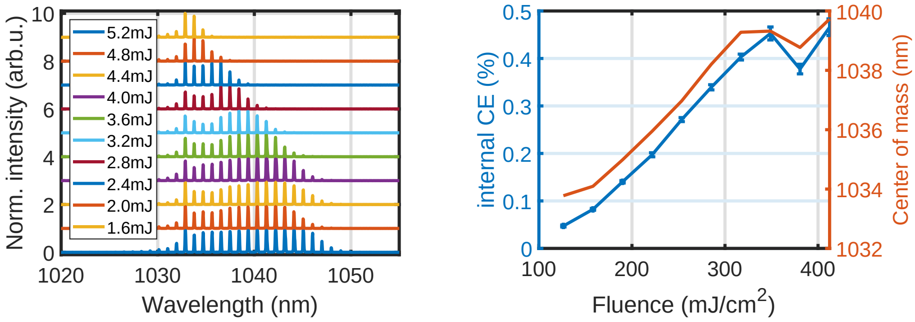

(a) (b)

Figure 5.8: a) Measured, normalized spectra after the MC-THz generation for different optical input energies. b) Peak fluence dependent center-of-mass of spectra and internal efficiency.

Finally, the spectral center-of-mass is calculated for each peak fluence and compared with the fluence dependent internal efficiency (Fig. 5.8b). The trends of both curves match well as predicted [40].

5.2.2 *MC-THz generation at 0.53 THz (crystals No. 3, 4 & 5)*

Measurements were performed now using the crystals No. 3, 4 and & 5 (Table 5.1) at RT and CT. These crystals with a poling period of Λ =212 μm is phase-matched for ∼0.53 THz (Fig. 5.1a).

The first scans have been performed with crystal No. 3 using the same experimental setup as in the previous section (Fig. 5.4) at RT and CT. This crystal was partially damaged before the scans. As expected, the efficiencies stayed low at RT as in the previous case and reached highest value of ∼0.014% for 250 ps (Fig. 5.9).

In the next step, this crystal was cooled down cryogenically to CT and the laser peak fluence increased up to 590 mJ/cm^2, which helped to increase the MC-THz energy ∼ 30 μJ for 250 ps pulse duration (Fig. 5.10a). This is equal to an internal CE of 0.49% (Fig. 5.10b). Only in the case of 250 ps, did the measured MC-THz radiation start to deviate clearly from the linear trend after 400 mJ/cm^2. The linear growth is predicted in analytical consideration for a undepleted pump in the absence of SPM and cascading effects.

As mentioned before, the crystal No. 3 was partially damaged. The next round of experiments was performed with the undamaged crystal No. 4, which has the same length, 2 cm long, and the poling period of 212 μm with a smaller aperture size of 3 × 3mm^2. The optimal wavelength was shifted around 57 pm compared to the previous scan at CT. This might be due to the usage of different masks in the poling procedure with slightly different poling or better cooling of the crystal. The results are summarized in Fig. 5.11a. The maximum internal MC-THz energy of ∼33 μJ was detected for the short-

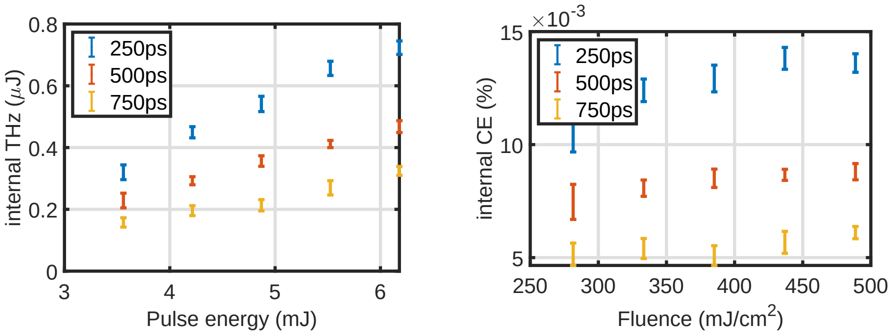

(a) (b)

Figure 5.9: RT scans with 4×4×20 mm^3 MgO:PPLN (crystal No. 3) using different optical pulse durations: a) The internal MC-THz yield as a function of laser input energy, b) the internal conversion efficiency as a function of laser peak fluence.

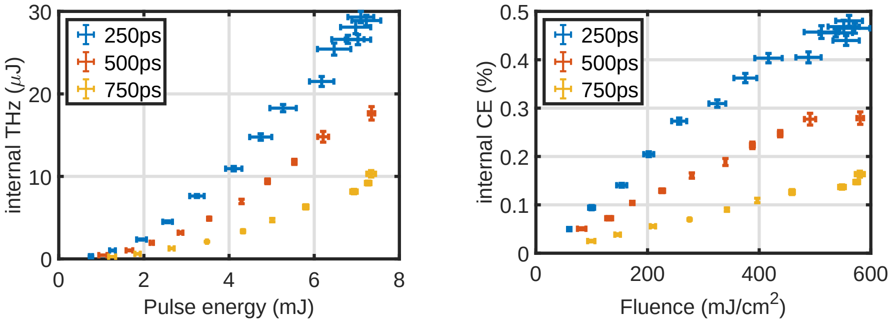

(a) (b)

Figure 5.10: CT scans with 4×4×20 mm^3 MgO:PPLN (crystal No. 3) using different optical pulse durations: a) The internal MC-THz yield as a function of laser input energy, b) the internal conversion efficiency as a function of laser peak fluence.

est pulse duration of 250 ps, which corresponds to an internal CE of ∼0.63%. Possible reasons for better efficiency: simplest one is the crystal being not damaged, another possibility could be that poling quality and cooling work better for smaller aperture size. The efficiency curve starts to deviate from the linear trend again around 400 mJ/cm^2 for 250 ps. Most likely, its an interplay between the aforementioned effects in the previous case. However, in both cases, crystal No. 3 and 4, no saturation visible. Therefore, in the next round of scans, a longer crystal was utilized.

The last scan with commercial MgO:PPLN was performed with the crystal No. 5, which produced the highest efficiency of 0.89% around at 480 mJ/cm^2 (Fig. 5.12), which is the highest recorded efficiency in narrowband MC-THz generation. Although no clear indication of saturation was present, the scans were stopped around 500 mJ/cm^2 because of the appearance of PR-effect (Fig. 5.13a). This effect disappears mainly after bringing the crystal back to RT (Fig. 5.13b), which is a well-know phenomena. The PR effect occurs

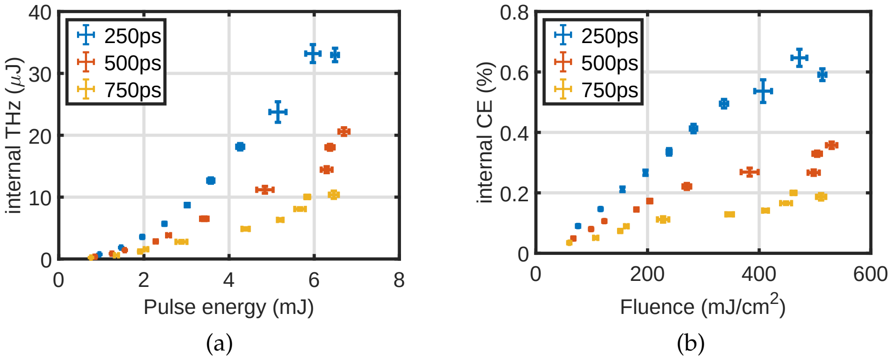

(a) (b)

Figure 5.11: CT scans with $3 \times 3 \times 20\,\text{mm}^3$ MgO:PPLN (crystal No. 4) using different optical pulse durations: a) The internal MC-THz yield as a function of laser input energy, b) the internal conversion efficiency as a function of laser peak fluence.

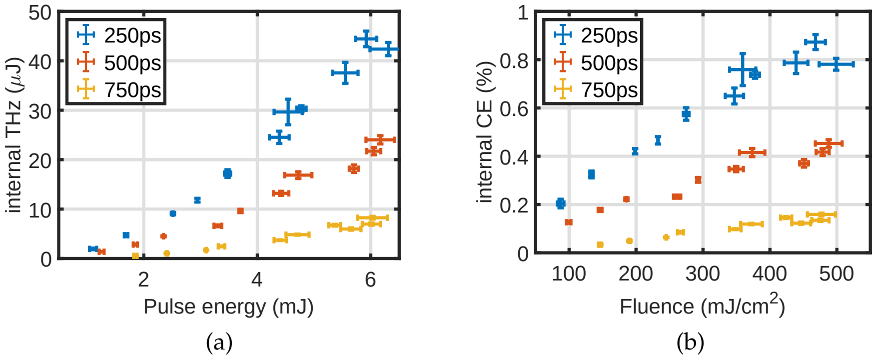

(a) (b)

Figure 5.12: CT scans with $4 \times 4 \times 40\,\text{mm}^3$ MgO:PPLN (crystal No. 5) using different optical pulse durations: a) The internal MC-THz yield as a function of laser input energy, b) the internal conversion efficiency as a function of laser peak fluence.

earlier in the longer crystal. This is why the peak laser fluence is kept lower for 4 cm compared to 2 cm long crystals.

Finally, the spectra from the high-resolution spectrometer are compared for the crystal length of 4 cm (crystal No. 5) at RT and CR in Fig. 5.14a and Fig. 5.14b. Such high efficiency, for example shown in Fig. 5.12b, is supported by strong cascaded broadening of the optical spectrum from 1015-1070 nm when the maximum peak fluence is achieved.

Thus, using the home-built multiline-laser source in commercial MgO: PPLN, efficiencies up to 0.89% have been demonstrated. The initial spectrum with two lines is broadened up to 70 nm, which could be used to seed another stage after compensation of the nonlinear phase. As predicted, having more lines could be increased to several percent levels.

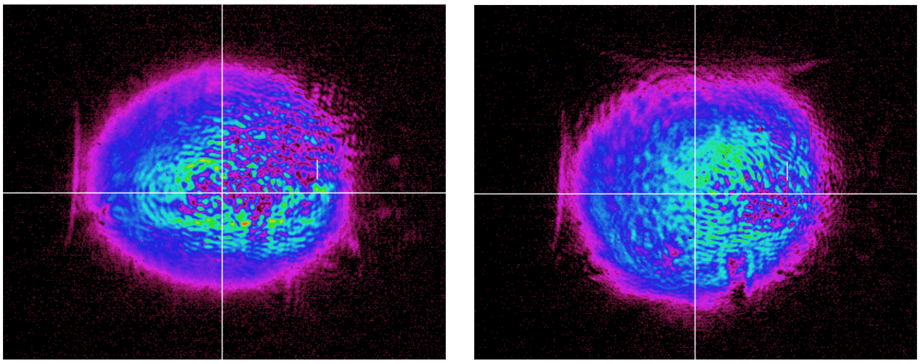

(a) CR (b) RT

Figure 5.13: Photo-refractive (PR) effect: (a) Image of optical beam profile after MC-THz (with crystal No. 5) at maximum fluence of $\sim$500 mJ/cm^2 at CT. (b) Image taken at same fluence, but after the crystal was warmed up to RT. At RT, the PR effect mainly heals itself and disappears.

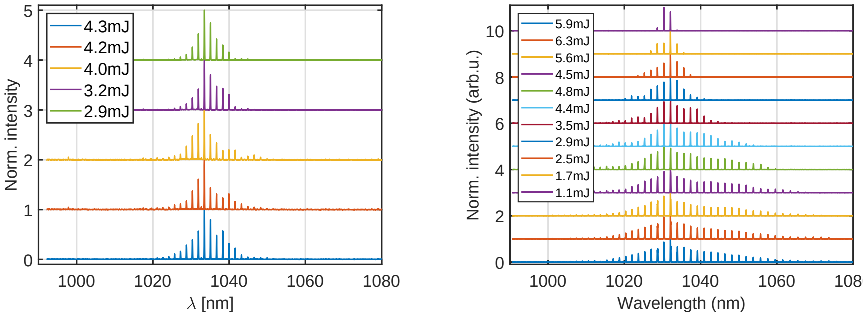

(a) RT (b) CR

Figure 5.14: The spectra of the optical beam after the MC-THz generation in the crystal No. 5 as a function laser input energy at a) RT and b) CR. At a pulse duration of 250 ps.

5.3 MULTILINE-THZ EXPERIMENTS WITH KTP

PPLN crystals with their higher effective nonlinear coefficient (see Table 2.1), are the widely used crystals for the MC-THz generation. So far, the highest efficiencies, including the findings of this work, are achieved using PPLNs. However, one of the biggest drawbacks of the PPLNs is the strong THz absorption at RT, which requires cooling to reduce the absorption coefficient [46], which unfortunately in parallel reduces its damage threshold. As demonstrated by the experimental results in the previous sections, although there was no clear indication of saturation in each case, the fluence could not be increased further due to the PR-effect leading to damage in the crystal [53]. The damage threshold of the PPLN must be investigated very carefully, especially in our case. Still, so far, the experimental evidence shows that the damage occurs at a lower fluence, when the crystal is cryogenically cooled and has a longer length A.1. However, the longer the crystal is, the more critical it will be to reduce the MC-THz absorption, which requires cryogenic cooling for PPLN.

Therefore, in this section, another nonlinear crystal, namely, the potassium titanyl phosphate (KTP), was tested, which is identified as a promising candidate due to its relatively high effective nonlinear coefficient (Tab. 2.1) and notably higher damage threshold A.1.

5.3.1 *MC-THz generation at 0.5 THz (crystal No. 6)*

MC-THz generation measurements were performed on a commercial, 15.5 mm long, periodically poled, Rb-doped potassium titanyl phosphate (Rb:PPKTP) crystal with a poling period of 300 μm and an aperture size of $1 \times 2\,\text{mm}^2$ (crystal No. 6).

The same experimental setup, as in the previous sections, was used. The beam size was reduced down to $0.5 \times 0.6\,\text{mm}^2$ (e^{-2} - radius) using a demagnifying telescope. First, similar to Section 5.1.1, the wavelength separation was optimized and the MC-THz yield was measured as a function of the wavelength separation (Fig. 5.15a). The maximum MC-THz yield was reached when the wavelength separation was set to 1.765 nm. The FWHM of the tuning curve is 38.5 nm, corresponding to 497.7 GHz with an acceptance bandwidth of 10.9 GHz. A comparison between the tuning curves in Fig. 5.15a and Fig. 5.1a (insert) for PPKTP and PPLN, respectively, show similarities. Both plots get broader towards higher wavelengths with a second peak, which supports the argument of higher-order nonlinear effects. Additionally, the delay-dependent THz autocorrelation trace was measured (Fig. 5.15b top). The Fourier transform gives the spectrum centered at 502 GHz with a bandwidth of 3 GHz (FWHM).

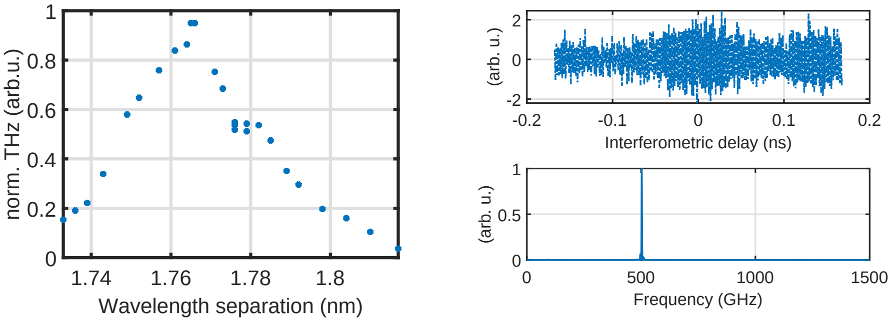

(a) (b)

Figure 5.15: a) Wavelength tuning curve for the 15.5 mm long Rb:PPKTP (crystal No. 6). b) THz interferometry measured THz auto-correlation trace (top), and calculated THz spectrum centered at 502 GHz with a bandwidth of 3 GHz (bottom).

The crystal (No. 6) was cooled down to CT. The peak fluence was increased to $1000\,\text{mJ/cm}^2$ while monitoring the beam profile for distortions. Since KTP has different refractive indices for the optical laser and the THz beam (Table 2.1), the Fresnel losses of 35.7% [29] must be considered. In Fig. 5.16, the results of this scan are summarized.

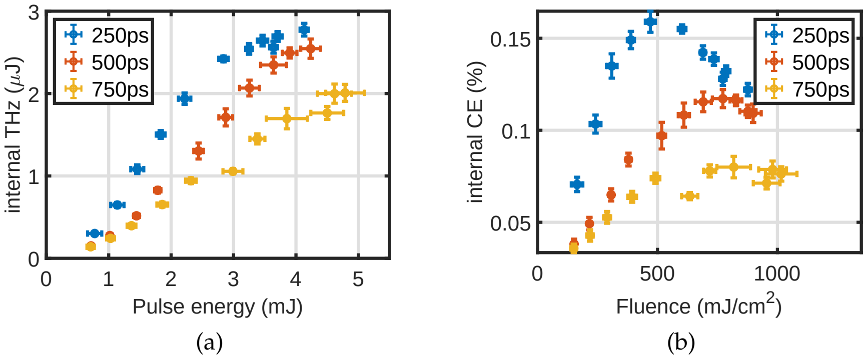

(a) (b)

Figure 5.16: CT scans with 1×2×15.5 mm^3 Rb:PPKTP (crystal No. 6) using different optical pulse durations: a) The internal MC-THz yield as a function of laser input energy, b) the internal conversion efficiency as a function of laser peak fluence.

Since the efficiency curves were saturated for 250 & 500 ps before reaching 1000 mJ/cm^2, both scans were stopped around 900 mJ/cm^2. For 750 ps, it was increased beyond 1000 mJ/cm^2 and no damage was observed. The saturation seems to happen in an intensity-related manner. Namely, the shorter the pulse duration is, the earlier the saturation starts. The maximum efficiency of 0.16% is achieved at around 500 mJ/cm^2 for 250 ps and efficiency drops afterwards.

The optical laser energy-dependent spectral profiles after MC-THz generation are given in Fig. 5.17. The changes in the the spectral broadening resembles changes in the conversion efficiency curves for pulse duration 250 ps (see Fig. 5.16b). The spectrum gets broader and shifts towards longer wavelengths with increasing input energy/fluence up to the point where the

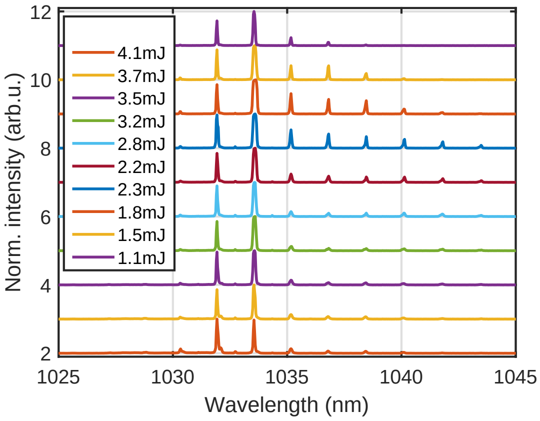

Figure 5.17: The spectra of the optical beam after the MC-THz generation in crystal No. 6 as a function laser input energy at CT. At a pulse duration of 250 ps.

conversion efficiency peaks at 500 mJ/cm^2 (or around 2.2 mJ), after which the spectral broadening and conversion efficiency reduces.

5.4 DISCUSSION OF THE EXPERIMENTAL RESULTS

Finally, the best results at CT for THz frequencies 0.29 THz and 0.53 THz with the crystal MgO:PPLN, and at 0.5 THz with Rb:PPKTP using a two spectral-line pulse with a duration of 250 ps are summarized in Fig. 5.18. In Fig. 5.18, MC-THz conversion efficiency is plotted against fluence. In the case of MgO:PPLN, the fluence was limited by the onset of the photo-refractive effect. In the case of Rb:PPKTP, any beam distortion has been observed, however the efficiency was saturated already therefore the fluence not further increased. In order to get an initial understanding of these results, it is best to begin with the analytical expression for the multiline efficiency developed by Vodopyanov [40], discussed in Section 2.7. Although it neglects, absorption, pump depletion, third-order nonlinear effects and importantly cascading effects, it can be used to provide scaling relations and can be used as a basis to generate a figure-of-merit (FOM) to compare different crystals. A comparison of MgO:PPLN and Rb:PPKTP is already discussed in Section 2.7.

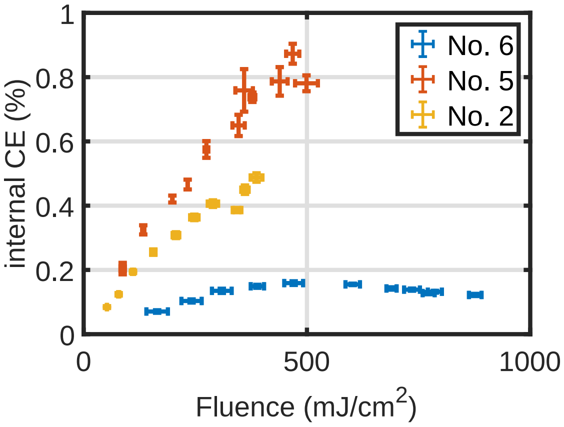

Figure 5.18: The highest achieved efficiencies using the two multiline laser source with a pulse duration of 250 ps for phase matched PM PPLN and Rb:PPKTP are summarized: Crystal No. 2 MgO:PPLN $4\times4\times40\,\text{mm}^3$, ν_0 =0.29 THz; Crystal No. 5 MgO:PPLN $4\times4\times40\,\text{mm}^3$, ν_0 =0.53 THz; and Crystal No. 6 Rb:PPKTP $1\times2\times15.5\,\text{mm}^3$, ν_0 =0.5 THz.

In the long pulse limit ($l_w >> L$, see Section 2.3.2), the conversion efficiency is proportional to the intensity or the fluence divided by pulse duration ($\propto F/\tau$). This scaling relation is generally fulfilled at low fluences in these results: for example, in Fig. 5.10b, the ratios of the initial slopes times the pulse duration for pulse durations 250, 500, 750 ps are 1: 1.12: 0.79, respectively. This would imply that reducing the pulse duration further would increase the efficiency before the onset of the photo-refractive effect. Firstly, this was not implemented because the multiline laser source was technically limited to 250 ps (see Section 4). Secondly, the analytical expression is only valid in the long pulse limit $l_w >> L$. However, a more realistic limit is set by the numerical simulation results of [42], where the peak efficiencies occur at 150 ps. Thus a shorter pulse duration from the multiline laser source would be a good method to improve the conversion efficiencies.

Next, the analytical conversion efficiency scales as the square of the phase-matched THz frequency ($\propto \Omega^2$) and the square of the length of the crystal ($\propto L^2$). Both these scaling relations are complicated by absorption, which is strongly dependent on the THz frequency. Comparing the results from crystals No. 2 and 5 in Fig. 5.18, it would be expected at low fluences an increase of 3.1 ($(0.53/0.3)^2$) using the analytical conversion efficiency. However, the measured values of 1.27 for 4 cm and 1.79 for 2 cm long crystals at 250 ps are much lower, because of the greater THz absorption at higher frequencies [46]. For shorter crystals, the improvement is bigger, which supports the dominance of the absorption. To see the expected improvement, one had to go below L_0 ~1 cm. Again, comparing the different used lengths from the results in Fig. 5.11b with Fig. 5.18, the expected increase in efficiency would be 4 ($(4/2)^2$). However, the experimentally measured increase was only 1.74 for 212 μm and 2.45 for 400 μm at 250 ps, again the absorption at higher terahertz frequencies is bigger and improvement smaller (Table 2.1).

The conversion efficiency magnitudes using the crystal MgO:PPLN, shown in Fig. 5.18, are best compared to numerical simulations that include all the important effects: including absorption, pump depletion, third-order nonlinear, and multi-photon conversion (cascade) effects. In the literature, a number of different optical laser sources are discussed [32, 34–36]; however, for this discussion numerical simulations from [42] are used, because in this paper, an idealized two-line laser source is used with MgO:PPLN generating MC-THz at 0.3 THz.

In this simulation, maximum efficiency of $\sim 1\%$ for MC-THz at 0.3 THz with a pulse duration of 250 ps in MgO:PPLN was achieved [42]. These simulations were performed on idealized periodically poled crystals, with no surface or bulk defects and where the periodic poling is perfectly regular with flat ferroelectric domain walls of zero thickness. In addition, the spatial profile of the optical beam was an effective flat-top (super-Gaussian m=5), which can greatly improve the efficiency up to 30%, compared to the usual experimental Gaussian shape [14]. Additionally, the optical beam was perfectly Fourier limited with initially no high order dispersion: this would not be the case for the experimentally used multiline source. Finally, the simulations were performed at a maximum damage fluence of 1120 mJ/cm^2 at a pulse duration of 250 ps predicted by Ref. [35]. During the experiment on crystal No. 2 at 0.3THz (Fig. 5.18), the fluence was kept below 500 mJ/cm^2, because of the observed onset of the photo-refractive effect. Thus the experimentally achieve efficiency of 0.49% is remarkably good compared to simulations [42].

Most experimental and numerical simulations were performed on MgO: PPLN, and very little work has been carried out on Rb:PPKTP. As shown in Table 2.1, KTP has two FOMs values that are larger than LN, and therefore, it might be worthwhile considering KTP as a serious candidate to replace LN. Additionally, KTP has a much higher damage threshold. Unfortunately, in this work, the maximum conversion efficiency using Rb:PPKTP was only 0.16% at 0.5 THz (Fig. 5.18). A number of factors might have contributed to this low value.

Firstly, except for testing KTP wafers in Section 7, only one Rb:PPKTP crystal was tested, so the quality of this crystal could not be compared to similar crystals. Secondly, the small aperture size of $1 \times 2\,\mathrm{mm}^2$ is too small for MC-THz generation. If it is assumed that the MC-THz is generated with a radius of 0.5 mm, then the Rayleigh length is 2.5 mm, greatly restricting the potential effective length of the crystal. Additionally, the actual crystal length of 15.5 mm (crystal No. 6) is also too short compared the effective length ($L_{\mathrm{eff}} \approx 180\,\mathrm{mm}$ see Eq.2.25). Therefore, further simulations and experiments are required to test the possibilities of this crystal.

6

TESTING LARGE APERTURE PPLN FOR USE IN NEW THZ-BASED ELECTRON ACCELERATORS

Recently, an important advancement was recorded in the THz-based electron accelerators using narrowband MC-THz radiation. The interaction length between the electron and THz radiation could be increased to a few centimeters [52], which is an order of magnitude higher than by the previous single-cycle (SC) THz driven electron acceleration [31]. However, the final energy was low within 1.6 keV due to the low THz energies of 20 nJ. In order to better study the feasibility of this approach, scaling up the final electron energy further, higher MC-THz energies are required. As Spencer et al. have been demonstrated [21], using large aperture MgO(5%):PPLN crystals and a joule-class Ti:sapphire laser, the THz energies could be scaled up to ∼600 μJ at ∼0.36 THz. These crystals have been specially grown in a research group of Prof. Taira [19]. With an aperture size of 10×15 mm^2, they are by far the biggest aperture sized PPLN crystal that has been produced. By contrast, the commercial available PPLNs are limited to ∼4×4 mm^2.

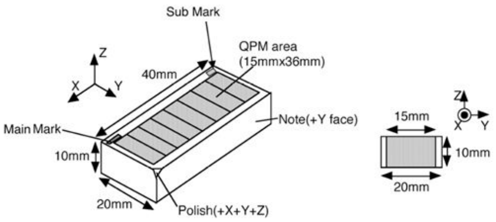

Figure 6.1: Large aperture PPLN for narrowband MC-THz generation.

In this chapter, the MC-THz generation in these largest aperture MgO:PPLNs is tested to be used for the next round of THz-based electron accelerators. As a laser source, the same 1 μm commercial laser as used in Chapter 7 was utilized. It provides pulse energies of 200 mJ at 52 Hz with a Fourier limited pulse duration of ∼500 fs. For the THz generation, the most straightforward method, namely optical rectification (OR), was utilized. Using this OR-approach in commercial MgO:PPLN, efficiencies of around 0.1% at ∼0.5 THz has been demonstrated [6]. Therefore, it is expected to scale up the MC-THz energies three orders of magnitude compared to the aforementioned THz-based electron accelerators [52].

The MC-THz generation was investigated for different crystal lengths at a range of temperature from room temperature (RT) and cryogenic nitrogen temperatures (CT). The available crystal lengths were 12, 16, 20, 24 and 36 mm. The pairs (12-24 mm and 16-20 mm) were cut from two 36 mm long crystals. One 36 mm long crystal was previously used in the C&D experiment [21] and has an anti-reflection (AR) coating at 800 nm. This crystal was the only one among the PPLNs with an AR-coating. In this chapter, the internal optical-to-THz conversion efficiency (CE) was calculated, taking into account the coating or no coating of all crystals. In addition, all crystals had the same poling period of 330 μm.

6.1 DETERMINING THE OPERATION RANGE

Before starting with the narrowband MC-THz generation experiments, the maximum laser peak fluence of ∼280 mJ/cm^2 was tested to see if damage occurs. In the previous measurements, there were some indications that in the case of lithium niobate crystals, the photorefractive (PR) effect starts before the crystal was damaged permanently and that it starts at lower fluences for longer crystals at lower temperatures (Section A.1). Therefore, a measurement was carried out with the 36 mm long MgO:PPLN with a poling periodicity of 212 μm (the highest poling density) first at RT and afterwards at CT.

The NIR laser beam was aligned through the crystal; the transmitted beam was sent onto a Teflon plate, which was then imaged by a CCD camera using an objective. Simultaneously, the back-reflected NIR and its 2$^{\text{nd}}$-harmonic generation were monitored by another camera. The laser beam profile was monitored for around 2 minutes at each laser peak fluence, roughly the time needed for a scan. If no damage appeared, the laser peak fluence was gradually increased until the maximum peak fluence was achieved. No damages to the crystal occurred both at RT and CT. Since large aperture MgO:PPLNs are very expensive, the purpose of a measurement was not to determine the damage fluence, but rather to find out the safe operation range without damaging the crystal.

6.2 THZ GENERATION AT RT AND CT

The experimental setup is illustrated schematically in Fig.6.2. The laser beam was aligned through the crystal, which was mounted on a cold-finger in a vacuum chamber, which in turn was attached to a cryogenic dewar for cooling down using liquid nitrogen. The whole dewar was mounted on an XY-rotation stage, which enabled the alignment of the beam through the crystal

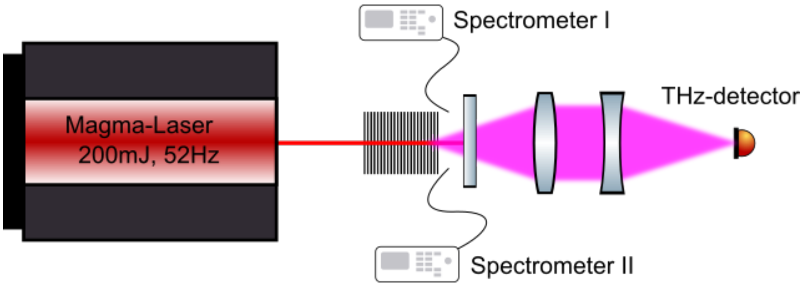

Figure 6.2: Experimental setup: The NIR laser beam is sent into PPLN crystal, which after the stack is blocked using a teflon shield. The MC-THz signal is collected and focused on a THz detector using two TPX-lenses.

by moving it relative to the beam. Using two irises, the beam's position was fixed and used as a reference for the alignment. Since a high energy laser source was used and most of the crystals were not AR-coated, the crystals were inserted with a small angle into the beam so that the back-reflected beam would not send back into the laser system, thus avoiding any damages. The laser beam after the crystal was blocked by a 1 cm thick teflon shield, which simultaneously worked as a diffuser for two spectrometers during the scans.

One of the spectrometers had a spectral resolution of 0.07 nm (*ASEQ*) and was used to detect the spectral broadening due to the interaction between the laser and the THz radiation, while the other one was a broadband spectrometer (200-1100 nm) with a spectral resolution of 0.2 nm (*HR4000CG-UV-NIR*) to monitor any parasitic effects, such as SHG, Raman scattering or any other parasitic phase-matched processes, which can lower the efficiency of THz generation, and may even lead to damages in the crystal [12].

To detect the generated THz radiation, two polymethylpentene (TPX) lenses with focal lengths of ($f_1 = 75$ mm and $f_2 = 50$ mm) were installed. The first TPX-lens collimates the THz radiation, and the second one focuses it onto a pyroelectric THz detector (*THZ9B*). To protect the THz detector from any kind of parasitic radiation such as the laser beam and its 2^{nd} harmonics, a 1 cm thick teflon shield was installed directly after the crystal, as well as two polyethylene shields: one between the two TPX-lenses and the other one in front of the THz sensor. Detection of the THz signal was optimized by adjusting the positions of the TPX-lenses and the position of the THz detector using two manual translation stages. Once the THz signal was maximized, the laser pulse energy-dependent THz generation can be started.

The NIR laser pulse energy was adjusted using a rotation stage mounted HWP and TFP before sending the beam into the compressor after the last amplification stage in the laser system. For each laser pulse energy, 30 datapoints from the THz and both spectrometers were acquired. Each device was triggered by a delay generator synchronized to the laser. This procedure was repeated for each crystal at RT and CT. The laser input energy dependent THz yields in large aperture MgO:PPLN are summarized for RT and CT in Fig. 6.3a and 6.3b, respectively.

To calculate the internal THz energy, all losses between the crystal and the THz detector were considered, such as the Fresnel's loss of the THz by the transmission from the crystal to the air, losses in the teflon shield, in the vacuum window, in both TPX-lenses and polyethylene shields (see Table 6.1). From the NIR laser, the geometrical losses due to the beam clipping and the Fresnel's loss (except the 36 mm crystal AR-coated) were considered. The geometrical loss was calculated by comparing the laser power with and without the crystal under the same conditions.

Knowing the internal THz and the laser input energy, it was possible to to determine the relationship between the laser peak fluence and the optical-to-THz conversion efficiency (CE). The results are summarized in Fig. 6.4a and Fig. 6.4b. Concerning RT scans, the CE decreases with increasing crystal

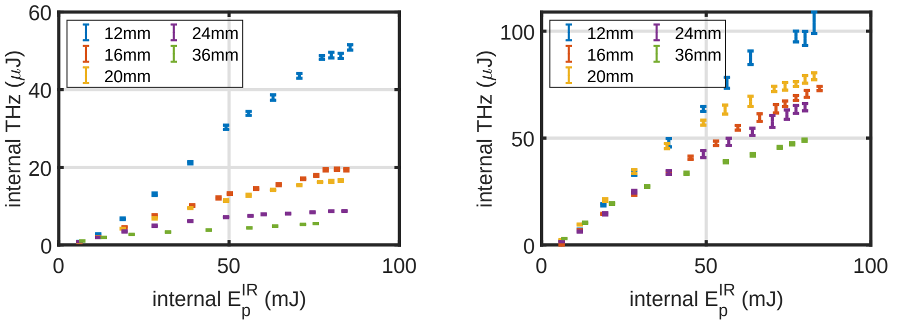

(a) RT

(b) CT

Figure 6.3: Laser pulse energy dependent THz generation in large aperture PPLNs with various lengths: 12, 16, 20, 24 and 36 mm at a) RT and b) CT.

Temp (K)	Teflon(%)	TPX(%)	Polyethylene(%)	Window(%)
RT	6	9	32	36
CT	4	9	37	38

Table 6.1: MC-THz losses in different materials: these values are determined using TDS (see Section A.2)

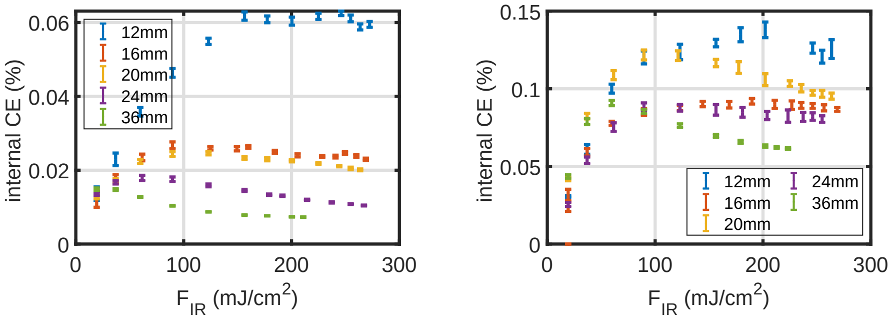

(a) RT

(b) CT

Figure 6.4: Internal CE as a function of laser peak fluence in large aperture PPLNs with various lengths: 12, 16, 20, 24 and 36 mm at a) RT and b) CT.

length due to the higher absorption coefficient at RT. After cooling down the crystals, the CE improves and the shortest crystal still produces the best results. Interestingly, at RT, both 16 mm and 20 mm crystals show similar MC-THz efficiency. This behaviour is mainly due to the crystal absorption. After cooling both crystals down to CT, the 16 mm crystal should perform better than the 20 mm crystal, which is not the case. Note that both crystals were cut from the single crystal into two pieces, thus similar crystal qualities are expected. Considering the relationship between the pulse duration and crystal length described in Section 2.4, the analytical expected $L_0 \approx 1\,\text{cm}$ (Eq. (2.24)). Thus longer crystals do not improve the efficiency and might even decrease due to the accumulating nonlinear effects. This is a possible explanation for the decrease in CE at higher fluence at both RT and CT.

To understand what happens in the NIR optical domain, the energy dependent spectral behaviours of laser beam after the interaction were plotted. These spectra were captured simultaneously with the MC-THz measurements. The results for 12 mm at RT (Fig. 6.5a) and at CT (Fig. 6.5b) and for 36 mm at RT (Fig. 6.5c) and at CT (Fig. 6.5d) are summarized. Comparing the spectra for short and long crystals, stronger spectral broadening is observed for the longer crystal. However, surprisingly, the spectral broadening for both crystal lengths at CT scans are smaller than at RT.

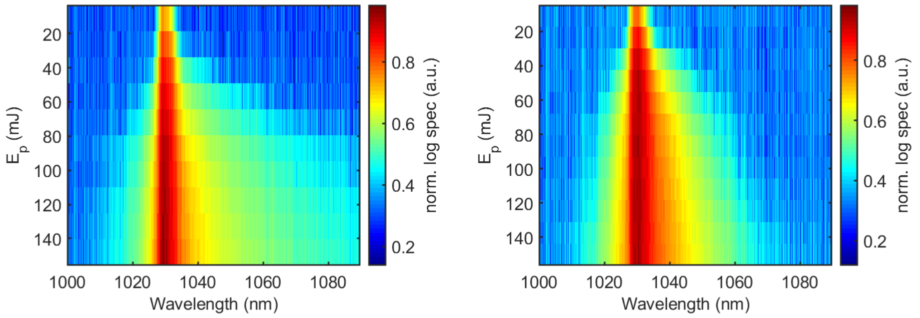

(a) 12 mm at RT

(b) 12 mm at CT

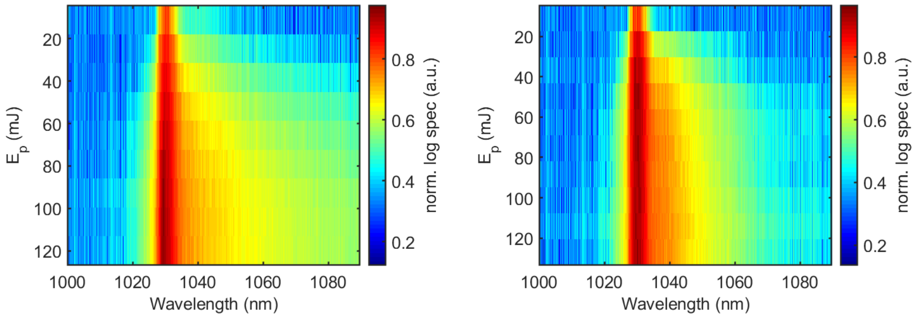

(c) 36 mm at RT

(d) 36 mm at CT

Figure 6.5: Energy dependent NIR optical spectral broadening in the MC-THz generation process for the cases: a)12 mm PPLN at RT, b) 12 mm PPLN at CT, c) 36 mm PPLN at RT and d) 36 mm PPLN at CT.

6.3 TEMPERATURE SCANS FOR MAXIMIZING THE EFFICIENCY

In order to optimize MC-THz generation, an additional measurement was performed, where the laser input energy was fixed to a certain value, and the MC-THz signal was acquired while cooling down the crystal from RT to liquid nitrogen cooled temperatures. The same experimental setup, as in the previous section, was utilized. The temperature was read out from a thermometer for each shot, which was attached to the copper cold finger - not on the crystal. For each data-point, the MC-THz signal, the photodiode-signal for the NIR pulse energy, and the spectrum after the interaction were captured in an automated fashion using a LabVIEW code.

The first scan has been performed using the shortest crystal (12 mm), the laser pulse energy was set to 130 mJ, and the data acquisition program was started. The scan was started at RT, and slowly the temperature was cooled down. The internal MC-THz energy is calculated by considering the THz losses in material (see Table 6.1) and Fresnel's losses at CT. Since all losses are frequency and, in turn, also temperature dependent, it is a possible error source in this scan. The result of this scan is summarized in Fig.6.6. This scan shows that the optimal temperature is actually not the lowest. When the temperature of the cold finger is around 140 K, the internal THz energy reaches 161 μJ that corresponds to an internal CE of 0.23%, which is by far the highest demonstrated value using the compressed pulse.

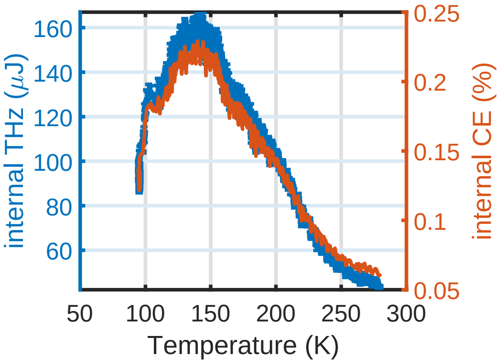

Figure 6.6: Temperature dependent MC-THz energy and CE with 12 mm MgO:PPLN: maximum THz energy of $\sim$ 160 μJ which corresponds to an internal CE of 0.23% has been achieved for fixed input energy of 130 mJ when the temperature of the cold finger was around 140 K.

This scan has been repeated using the 16 mm crystal. Two temperature dependent energy scans with input energies of 60 mJ and 115 mJ have been performed and the results are summarized in Fig. 6.7a and Fig. 6.7b. Similar to the previous case, the best results were achieved at around 140 K. The CE was almost doubled and reached a value of >0.1% for 115 mJ.

The next scan used a crystal of length 20 mm. This crystal was more intensively investigated, for four different input energies of 35, 60, 90 and 115 mJ and the temperature dependent MC-THz yields were measured. The results of these scans are plotted in Figs. 6.8a and Figs. 6.8b. In this case, saturation effects were visible both at low and high temperatures. At approximately 145 K, the highest CE of 0.175% was achieved for the input energy of 90 mJ.

The next round of scans were performed with a crystal length of 24 mm crystal. The results are summarized in Fig. 6.9a and Fig. 6.9b. The efficiencies for different input energies of 60, 90, and 115 mJ were converged throughout the temperature range. In this case, a maximum CE of 0.1% was reached at around 140 K.

The last scan has been performed with the 36 mm long crystal at an input energy of 60 mJ. This crystal is AR coated for 800 nm on both surfaces. The

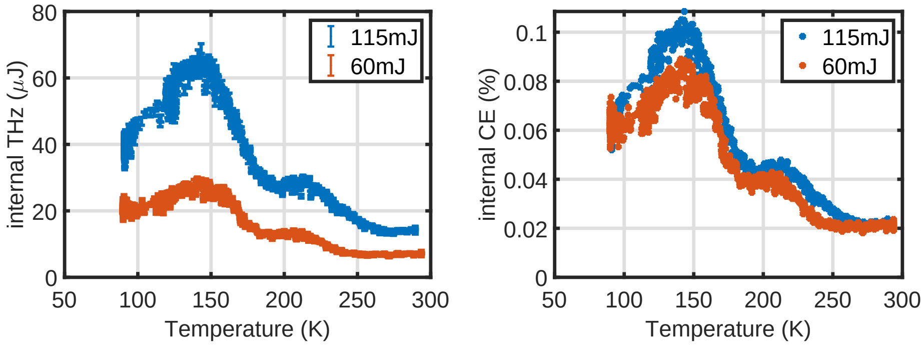

(a) THz vs. Temperature (b) CE vs. Temperature

Figure 6.7: Temperature dependent MC-THz energy (a) and CE (b) in 16 mm MgOPPLN: scans have been performed for two different input energies of 60 and 115 mJ. The maximum internal CE of ∼ 0.1% has been achieved at around 140 K.

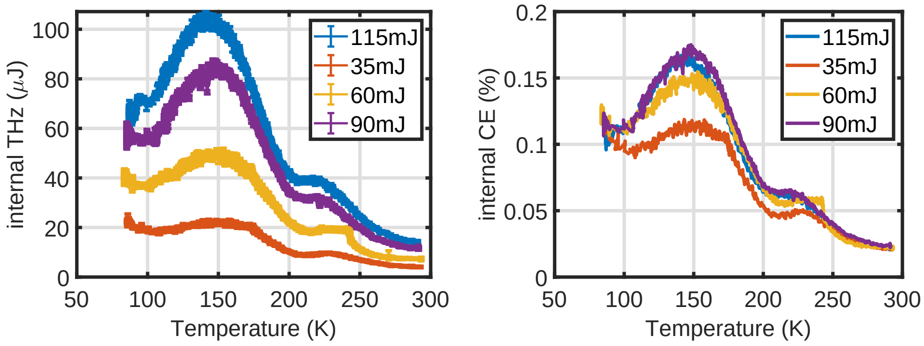

(a) THz vs. Temperature (b) CE vs. Temperature

Figure 6.8: Temperature dependent THz energy (a) and CE (b) in 20 mm MgOPPLN: scans have been performed for four different input energies of 35, 60, 90 and 115 mJ. The maximum CE of 0.175% has been achvied around 140 K for second highest input energy of 90 mJ.

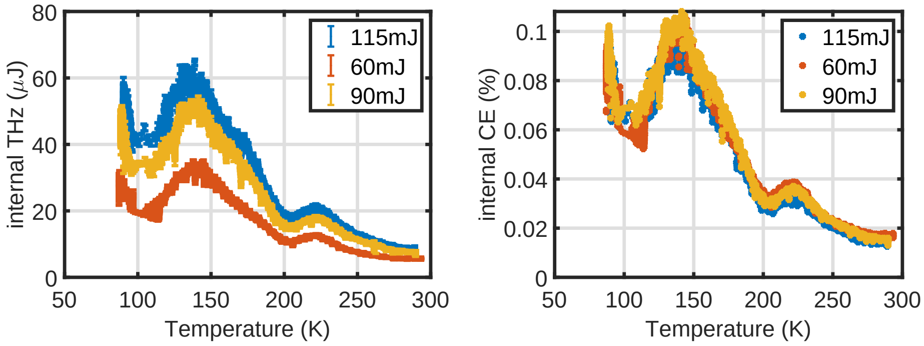

(a) THz vs. Temperature (b) CE vs. Temperature

Figure 6.9: Temperature dependent MC-THz energy (a) and CE (b) in 24 mm MgOPPLN: scans have been performed for three different input energies of 60, 90 and 115 mJ. In all three cases, the CE is in similar range.

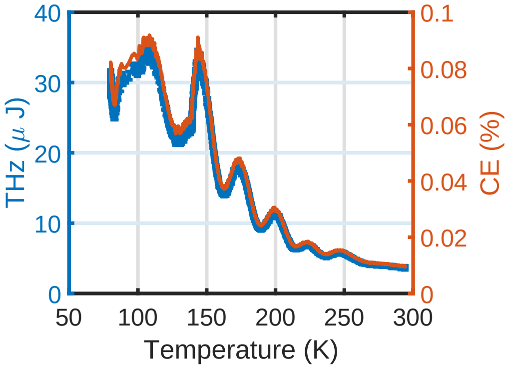

Figure 6.10: Temperature dependent THz energy and CE in 36 mm PPLN: the number of bumbs increase up to six and narrower than before.

behavior is significantly different compared to the other crystal lengths: the temperature scan has a number of peaks. The origin of the peaks is unknown. However, a maximum CE of 0.09% is achieved at around 107 K, which is slightly above the usual maximum for other crystal lengths, which is around 144 K.

Besides measuring the temperature dependent MC-THz energy, the spectrum of the NIR laser after the crystal was observed at the same time. As an example, the result with the 16 mm crystal is plotted in Fig. 6.11. The spectral intensity and the broadening of the spectrum decreases at around 140 K, which is an indicator of NIR absorption of the laser beam.

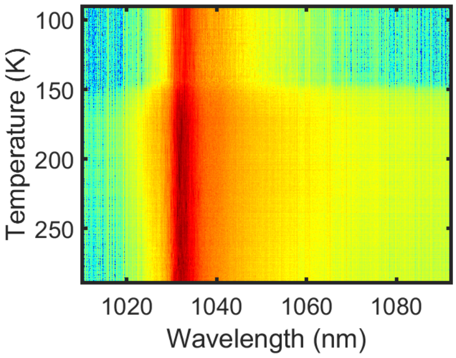

Figure 6.11: Temperature dependent spectra of the NIR beam after 16 mm long MgOPPLN.

The spectra in Fig. 6.11, for each temperature step are integrated over the wavelength, then normalized and plotted against temperature for all measured crystal lengths. The spectral behaviour is similar in all cases independent of the crystal length (Fig. 6.12a). The spectral intensity increases slightly in the cooling process from RT to 140 K, and falls during further cooling. In order to check whether this phenomenon is intensity related, the results with 24 mm crystal with different input energies are summarized in figure 6.12b. The general behavior follows a similar trend in all three cases. At cryogenic temperature, 115 mJ with the highest input energy shows the lowest level,

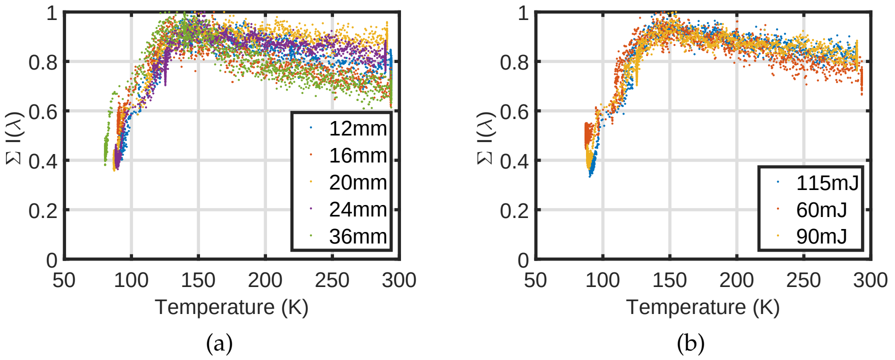

Figure 6.12: Temperature dependent over wavelength integrated spectra for a) different crystal lengths b) different intensities in 24 mm long PPLN.

and the lowest input energy of 60 mJ remains the highest. It seems to be slightly intensity-dependent, which is more a minor effect.

6.4 OPTIMIZING THE EFFICIENCY

From the previous Section 6.3, the best efficiency of 0.23% was obtained with the 12 mm long crystal at around 140 K at a laser peak fluence of 240 mJ/cm^2. The efficiency is just below the current highest value in narrowband MC-THz generation using the chirp and delay concept [21], which was 0.24%. Therefore, it was decided to increase the laser input energy further to 160 mJ, corresponding to a peak laser fluence of 280 mJ/cm^2, to see if the efficiency can be improved further.

The temperature of the cold finger was set to the desired value of approximately 140 K, the angle of the motorized rotation stage was set to the correct value, which was determined beforehand using the power meter. Both the THz signal and the temperature of the cold finger were observed while rotating the rotation stage. The results of this temperature scan are depicted in Fig. 6.13.

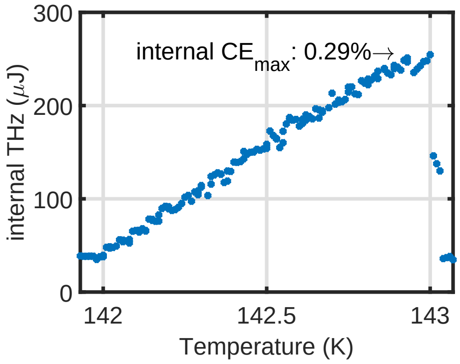

Figure 6.13: At ~143 K in 12 mm long MgOPPLN, the peak fluence is gradually increased up to 280 mJ/cm^2 and the THz yield is measured. The maximum internal efficiency of 0.29% is reached.

The efficiency reached to 0.29% for the laser peak fluence of 280 mJ/cm^2 when the temperature of the cold finger was at around 143 K. This is so far the highest efficiency achieved using the OR technique.

6.5 TEMPERATURE DEPENDENCE OF THE CENTRAL FREQUENCY OF THE MC-THZ

From the application point of view, it is crucial to determine the central frequency of MC-THz and the bandwidth. Therefore, a THz interferometer was utilized to measure them at RT and CT.

The delay dependent interferometric autocorrelation traces were plotted for RT and CT in the upper parts of Fig.6.14a and Fig. 6.14b, respectively. Using a FFT, the corresponding spectra were calculated and plotted in lower parts of the figures, which are centered at 322 GHz with a bandwidth of ~2.2% at RT and 355 GHz with a bandwidth of ~1.6% at CT. The shift in the central frequency happens due to the temperature dependent refractive index. The bandwidth narrowing indicates that some of the MC-THz gets absorbed by the crystal, and therefore, number of cycles in MC-THz are higher at CT.

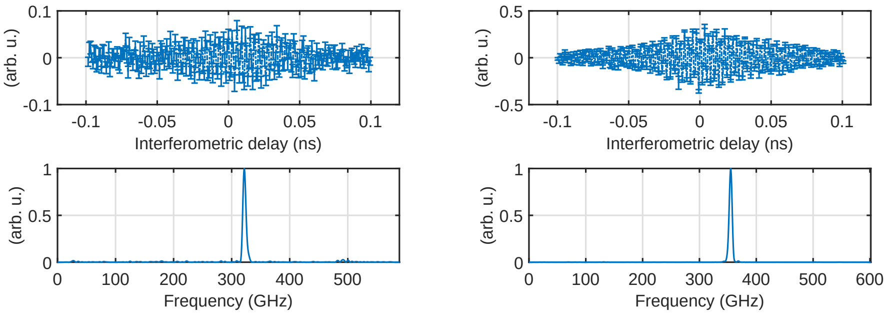

(a) RT

(b) CT

Figure 6.14: Interferometric correlation of the in 12 mm long MgOPPLN generated MC-THz pulses (top) and its frequency spectrum (bottom) at RT (a) centred at 322 GHz with a bandwidth of ~2.2% and at CT (b) centred at 355 GHz with a bandwidth of ~1.6%.

Another measurement was carried out with the longest crystal of 36 mm length. The signal at RT was very weak, and in order not to damage the crystal, it was decided not to push laser peak fluence to higher values. The results of the CT measurement are illustrated in Fig. 6.15. The central frequency at CT is slightly shifted compared to the 12 mm crystal at CT and was 348 GHz, with a bandwidth of ~0.5%, which is around three times narrower than that of the 12 mm PPLN, which is consistent with the theory ($\delta\nu \propto 1/N$), (see Eq. (2.15)).

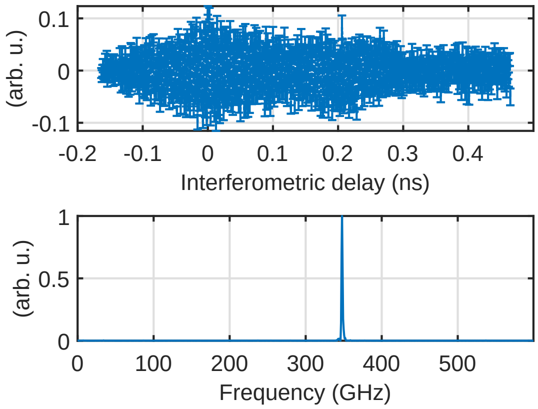

Figure 6.15: The interferogram of the in 36 mm long PPLN generated THz pulses and its frequency spectrum at CT, which is centered at 348 GHz with a bandwidth of ∼0.5%.

6.6 DISCUSSION

The largest aperture, commercially available, periodically poled LN crystals are $\sim 4 \times 4\,\text{mm}^2$, and presently, the largest available crystals ($10 \times 15\,\text{mm}^2$) come from the group of Prof. Taira [19]. These crystals are periodically poled from a single grown crystal with the desired electrostatic field applied externally to achieve the desired periodic pole structure. There could be a natural limit to this process and as the aperture size grows, the flatness of the domain walls between each period should decrease. Therefore, in this Chapter 6, a range of large aperture crystals ($10 \times 15\,\text{mm}^2$) with various lengths were tested at relative high NIR pulse energy. Since pulse energies of the developed two-line laser (15 mJ), discussed in Chapter 4, was limited, it was decided to use a commercial laser (200 mJ) using optical rectification (OR) to generate MC-THz. Although this method is not as efficient as the method discussed in Chapter 5, with this MC-THz generation system, it is possible to test these large aperture crystals, and in addition, have large energy MC-THz to be used in the next generation of THz-based electron accelerators [52].

In this chapter, the length-dependent THz generation by optical rectification (OR) in large aperture ($10 \times 15\,\text{mm}^2$) MgO:PPLN crystals at RT and CT was investigated. Using the shortest crystal length (12 mm), the highest efficiencies of 0.06% and 0.14% at 322 GHz and 355 GHz were achieved with a relative bandwidth of 2.2% and 1.6% for RT and CT, respectively. Further increase in crystal length resulted in a drop in the efficiencies for both cases, especially at CT, where the absorption of the NIR increases with increasing fluence, and it is expected that nonlinear effects such as self-phase modulation are present at high fluences [40].

Finally, the temperature-dependent MC-THz generation experiment has shown that the absorption of NIR increases when the temperature of cold finger drops below ∼140 K, and efficiencies are maximized at around this temperature range. Thus the maximum efficiency of 0.29% was obtained at a peak fluence $\sim$280 mm/cm^2 in the shortest crystal.

7

THZ GENERATION USING WAFER STACK

As demonstrated in Chapter 5, the optical-to-THz CE can be increased to the percentage level using an adequate laser source, which is one of the most crucial determinants to achieve the required narrowband THz source in the AXSIS project. Basically, using a commercially available joule-class laser, the MC-THz energies could be scaled up to the millijoule level. However, in addition to the choice of the laser source, there are limitations from the conversion material. Especially, the damage threshold of the material limits the laser energy, which can be shone onto the crystal. In order to surpass this limitation for a given material and pulse duration, the beam size must be increased while keeping the laser peak fluence constant ($F < F_{damage}$). Therefore, methods to increase the aperture size must be discussed.

Since the standard mechanism behind narrowband MC-THz generation is the optical DFG by QPM in a periodically poled nonlinear crystal, this is not only an issue for crystal growth but also the poling mechanism. As described in Chapter 6, there is a limitation on the electric field in the commonly used poling method, which can be applied to the crystal to achieve periodically poling by aligning or flipping the ferroelectric polarization domains [48]. Presently, commercially available PPLNs are limited to an aperture size of $4 \times 4\,\mathrm{mm}^2$. The group of Prof. Taira has grown and poled LN crystals with an aperture size in centimeter-scale ($1 \times 1.5\,\mathrm{cm}^2$) [20], which was used to demonstrate record-level THz energies of $600\,\mu$J by the C&D technique [21]. Similar size crystals have been tested in this thesis in Chapter 6. These sizes are still not large enough for the requirements of the AXSIS project, given the new requirements discussed at the end of Chapter 5. Therefore, another strategy must be developed; one of the possibilities is the wafer concept.

As aforementioned, the optical MC-THz generation suffers from low efficiency owing to the large photon energy difference between optical and THz. This effect could indeed help to solve the problem from the technical point of view since the required poling periodicities for the aimed THz frequencies are then in several hundreds of micrometers range. Therefore, instead of using the standard technique for poling, thin crystal slides with a known *c*-axis can be used, which can be manually stacked with alternating *c*-axis orientation.

Fortunately, LN growth of large crystals is a well-established technology, thanks to its widespread usage in the telecommunications industry. LN wafers with an aperture size of up to 2" are commercially available for a reasonable price. Thus, by combining differently poled single crystal wafers, the aperture size can be increased, and the crystals' length can be arbitrarily varied. This method also offers a unique possibility to investigate the length-dependent MC-THz generation continually. As analytical [40] and numerical

[42] works show, the crystal length is one of the critical parameters for the MC-THz generation. Besides this, it defines the phase-matching bandwidth, which is crucial for accelerator technologies.

Another advantage of this concept is that basically any crystal could be stacked periodically poled. Current results show that potassium titanyl phosphate (KTP), especially with its higher damage threshold, is a promising candidate for the high energy MC-THz generation besides lithium niobate (LN). As demonstrated in Chapter 5, using a commercial Rb:PPKTP with an aperture size of only $1 \times 2\,\mathrm{mm}^2$, efficiencies of 0.16% have been demonstrated. The height of this crystal, along which the poling field applied, was limited to only 1 mm. Therefore, testing the wafer concept with KTP is very worthwhile.

In this chapter, using the wafers listed in Table 7.1, the following issues will be addressed:

- In Section 7.1, general tests of LN wafers (No. 1) at RT are considered, including damage threshold of single wafers, stack length-dependent MC-THz generation, and thereby testing the general concept of stacking of AR-coated wafers.

- In Section 7.2, series of stacks of LN wafers (No. 1) at RT, similar to that simulated in Ref. [42] are considered (also see Fig. 2.7). Thereafter, the back-reflected seeded MC-THz generation will be investigated. In both cases, an increase in the total efficiency is observed.

- In Section 7.3, an LN wafer stack (No. 2) is cooled down to CT to test the improvement of the efficiency at CT.

- In Sections 7.4 and 7.5, KTP wafers (No. 3 & 4) are tested at RT and CT.

Table 7.1: List of the wafers that were used for the narrowband MC-THz generation at RT and/or CT. All wafers are AR-coated for NIR. LN and LN* are purchased from different manufacturers, and KTP and KTP* were also purchased from different manufacturers.

No. Wafer	Shape	Aperture	Thickness (μm)	Experiment
1. LN	circular	1"	300	RT
2. LN*	rectangular	$25 \times 26\,\mathrm{mm}^2$	200	RT&CT
3. KTP	square	$10 \times 10\,\mathrm{mm}^2$	250	RT
4. KTP*	square	$10 \times 10\,\mathrm{mm}^2$	250	RT&CT

7.1 WAFER STACK TESTS USING WAFER NO. 1

The initial tests were carried out on wafers No. 1 (Table 7.1) at RT. These lithium niobate wafers are 300 μm thick with a circular shape and a diameter

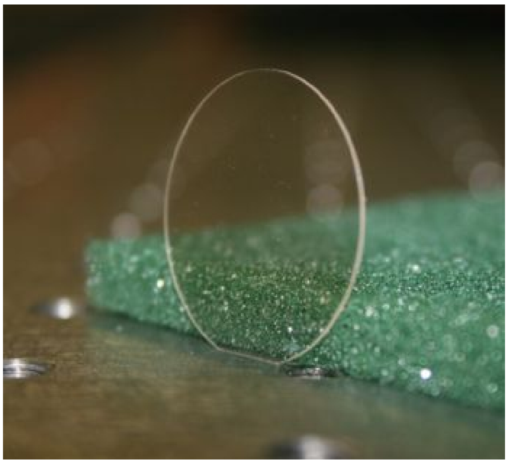

Figure 7.1: Wafer No. 1: 300 μm thick lithium niobate wafer.

of 1" (Fig. 7.1). One side of the wafer is marked to indicate the direction of the crystal's c-axis, along which the E-field of the laser must be applied to reach the strongest nonlinear polarization. Both surfaces of the wafers are polished and AR-coated.

7.1.1 *Damage Threshold of a single LN wafer (No. 1) at RT*

One of the most important limitations for the MC-THz generation is the damage threshold of the nonlinear crystals, limiting the laser fluence that can be irradiated on the crystal. Therefore, it is very critical to characterize it before starting any MC-THz generation experiments. The basic idea was to slowly increase the laser peak fluence and observe the laser beam profile to detect any distortions related to damage. The laser peak fluence can be varied either by changing the pulse energy or beam size. The laser system, which was used to generate the MC-THz radiation, is a commercial high energy laser system that can deliver ~500 fs compressed pulses at a repetition rate of 52 Hz with a pulse energy of 200 mJ. A single focusing lens was used, and by varying the crystal position along the beam propagation direction, the fluence can be varied. This is a convenient approach, considering the high laser pulse energy and related B-integral in transmissive optics. Additionally, the crystal thickness is only 300 μm, the fluence change within the crystal stays minor when a loose focusing lens with a relatively long focal length is employed.

The laser pulse energy was set to 20 mJ, and a lens with a focal length of 1000 mm was used. Considering the material properties and the thickness of the lens, the B-integral contribution of the lens stays below 0.7. The wafer was mounted in a lens holder and fixed to a manual translation stage. The crystal was inserted at a slight angle to avoid back-reflection into the camera (*Spiricon SP620U*). For different stage positions and fluences, the reflected beam was monitored for 20 min. The beam profiles after 20 min are shown in Fig. 7.2.

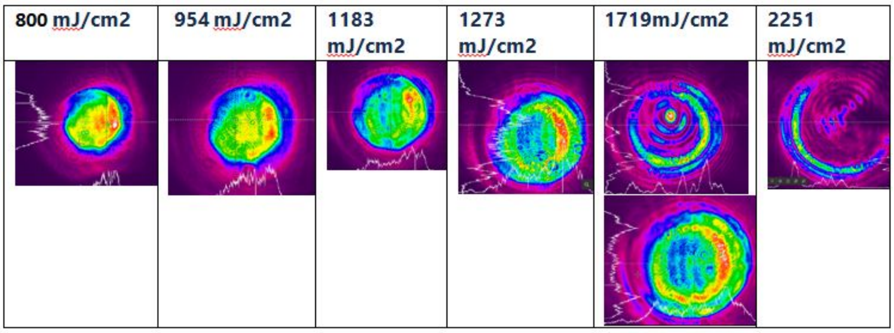

Figure 7.2: The reflected laser beam profiles from wafer No. 1 using various fluences at RT. The image is taken after 20 min measurement.

A closer look reveals that the beam profile starts to change at a fluence of 0.9 J/cm^2. This effect becomes more dominant around 1.2 J/cm^2, but no damage was observed after blocking the laser beam. This is a known phenomenon in LN crystals, called the photo-refractive (PR) effect, which can be reduced by magnesium oxide (MgO) doping in LN [13].

The fluence was further increased to 1.7 J/cm^2, the PR-effect appears immediately, and the crystal was damaged within five minutes. In order to repeat this measurement under the same fluence, the crystal was moved sideways. This time stays, the crystal remained undamaged for 20 minutes. However, PR-effect was very strong in both cases. So usage of the crystal at this fluence is not possible. In the last step the fluence is further increased to 2.2 J/cm^2, which damages the crystal immediately as shown in Fig.7.3.

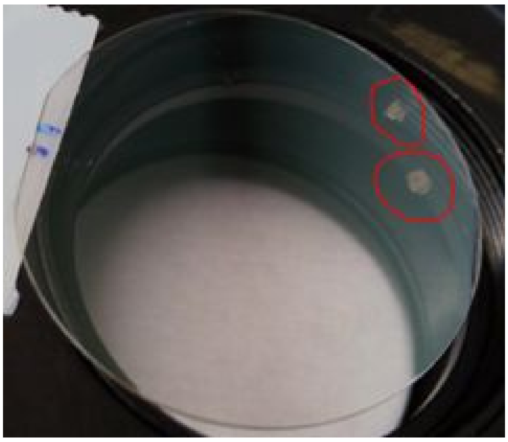

Figure 7.3: Damage of wafer No. 1 at RT with fluence of 2.251 J/cm^2 at two positions (red circles).

In conclusion, for a wafer at RT, the laser peak fluence can be increased up to 0.8 J/cm^2 without observing any degradation in the beam quality. However, the previous damage threshold measurements showed that the photorefractive effect occurs at lower fluence for longer crystals (Section A.1). Consequently, it was decided to carry out the first series of MC-THz generation experiments without changing the laser beam size, which means the maximum laser peak fluence stayed below 400 mJ/cm^2.

7.1.2 *Length dependent MC-THz generation at RT using wafers No. 1*

One of the most critical parameters for the MC-THz generation is the length of the crystal. Within the analytical plane-wave approximation (Eq. (2.21)), linear growth of efficiency is predicted within the crystal length. However, the efficiency growth rate drops after a certain length (see Section 2.4). There might be several reasons for that: MC-THz absorption, pump depletion, walk-off, spectral broadening, or SPM. The wafer concept gives us a unique possibility to investigate the length-dependent MC-THz generation.

The 300 μm LN-wafers (No. 1) were installed in a holder, which enables stacking them together with alternating c-axis orientation. They are pressed together. The experimental setup is shown schematically in Fig. 7.4. The compressed output of the laser was sent into the wafer-stack. The wafer-stack was inserted into the beam with a slightly tilted angle to prevent any back-reflections into the laser. After the interaction, the NIR laser beam was filtered out using a 1 cm thick teflon plate, which was then monitored by two spectrometers. One of them is measuring a smaller spectral range from 980-1090 nm, with a spectral resolution of 0.07 nm (*ASEQ*) to investigate spectral changes due to the MC-THz generation. The other one measures a broader range from 200- 1100 nm, with a spectral resolution of 0.2 nm. The second spectrometer enables detecting any possible parasitic effects, such as SHG, Raman-scattering, or any unwanted parasitically phase-matched process.

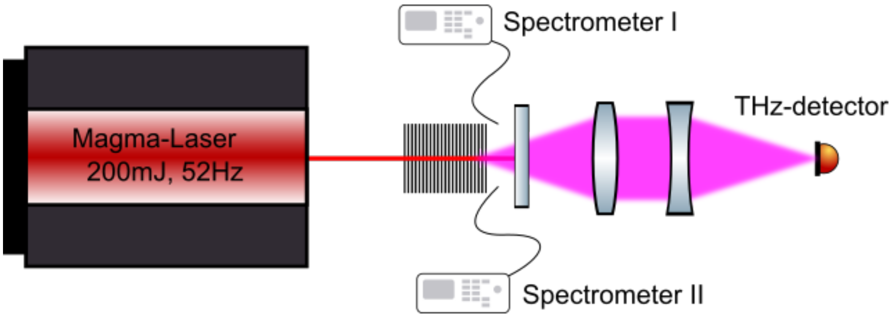

Figure 7.4: Experimental setup: The NIR laser beam is sent into a wafer stack, which after the stack is filtered out using a teflon shield. The MC-THz signal is collected and focused on a THz detector using two TPX-lenses.

The generated MC-THz signal was detected using a pyroelectric detector via an imaging system consisting of two polymethylpentene (TPX) lenses. To ensure that no NIR laser beam or its 2^{nd}-harmonic reaches the THz detector, two more polyethylene shields were installed, in addition to the 1 cm teflon beam block - one directly in front of the THz detector and the other between the two TPX lens pair.

The number of wafers was increased from 1 to 31 wafers in steps of 1. The generated MC-THz was measured both as a function of the laser pulse energy and wafer number. Taking into account the THz losses from the stack to the detector, such as material losses (see Table 7.2) and the Fresnel losses of 44.4% under the assumption that the THz beam hits perpendicular to the transmission surface, the internal MC-THz pulse energy is calculated.

Table 7.2: THz losses in different materials at 160 GHz: these values are measured using THz-TDS (see Section A.2).

Frequency (GHz)	Teflon (%)	TPX (%)	Polyethylene (%)
160	7	23	31

The input energy and length dependent MC-THz yields are depicted in Fig. 7.5a. To calculate the laser peak fluence dependent internal optical-to-THz conversion efficiency, the laser beam size at the wafer position was measured, whose beam waist was 6.3x5.7 mm^2 (*radius at* e^{-2}), and assumed that the laser is transmitted into the stack without losses due to the AR-coating. The herewith calculated CE is shown in Fig. 7.5b in dependence of the number of wavers and the laser peak fluence.

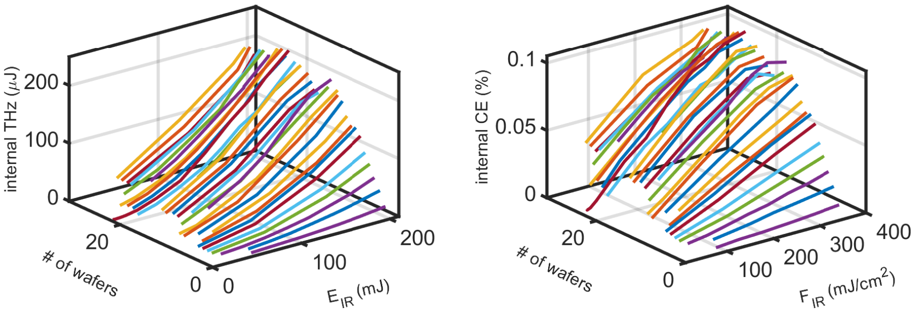

(a)

(b)

Figure 7.5: a) The evolution of internal MC-THz energy depending on NIR optical energy and on different wafer numbers at RT. b) The dependence of the internal CE on NIR optical fluence and number of wafers at RT.

To summarize these results, the wafer number dependent internal MC-THz energy and CE for the maximum laser peak fluence are plotted in Fig. 7.6. According to these data, the MC-THz yield increases up to 13 wafers and starts to saturate with increasing wafer's number. The best results are achieved at 22 wafers with more than 200 μJ, which corresponds to ∼0.1% internal CE.

The NIR optical spectra after MC-THz generation passing through 2 and 31 wafers are shown in Figs. 7.7a and 7.7b, respectively. Clearly, spectral broadening becomes very apparent for 31 wafers. The intensity is plotted on a logarithmic scale to see the effects aside from the central wavelength.

Finally, the central frequency of the generated MC-THz signal was determined for 31 wafers using a THz interferometer. The measured delay-dependent interferogram is shown in the upper diagram of Fig. 7.8, and by taking the Fourier transform of it, the corresponding spectrum is calculated. The generated THz was centered at 159.4 GHz, which a bandwidth of 1.7 GHz. As can be seen, no higher harmonics of the THz frequency are visible.

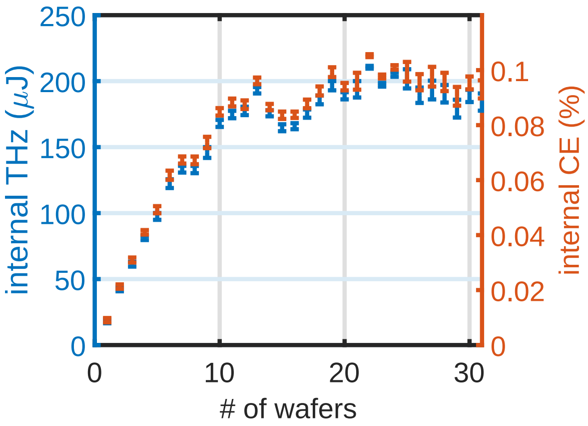

Figure 7.6: Length dependent THz yield and corresponding internal CE at max peak fluence.

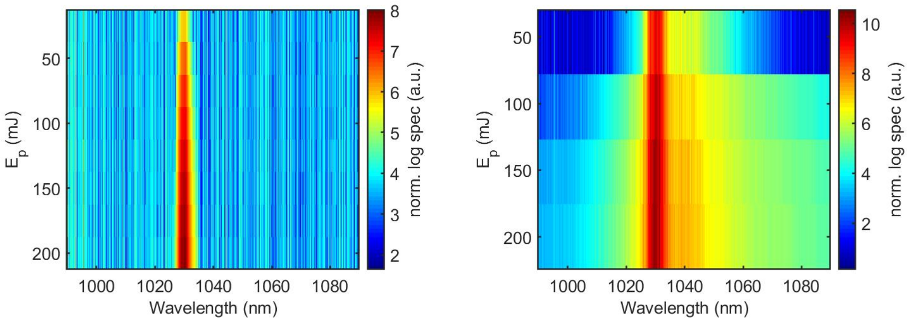

(a)

(b)

Figure 7.7: Input energy dependent NIR optical spectra taken after MC-THz generation in a stack with a) 2 wafers and b) 31 wafers.

7.1.3 *Does poling work?*

In order to prove that the poling concept is working and to give a qualitative impression of the uniformity of the ferroelectric wafers, two cases were compared: alternating and non-alternating. In the non-alternating case, the orientation of the c-axis for all wafers was pointing in the same direction; hence, no quasi-phase-matching should be present. The same experimental setup as the previous scans was utilized. The laser input energy-dependent MC-THz yield was measured for the following wafer numbers: 1, 2, 3, 4, 6, 8, 10, and 16. The results at the same maximum peak fluence were summarized and compared for the alternating and the non-alternating cases (Fig. 7.9). The number of wafers was increased up to 16 wafers. The measured MC-THz yield decreases/increases for the non-alternating/alternating case with increasing wafer number. In the case of the alternating wafers, the MC-THz energy is around 45 times greater than for the non-alternating case with 16 wafers.

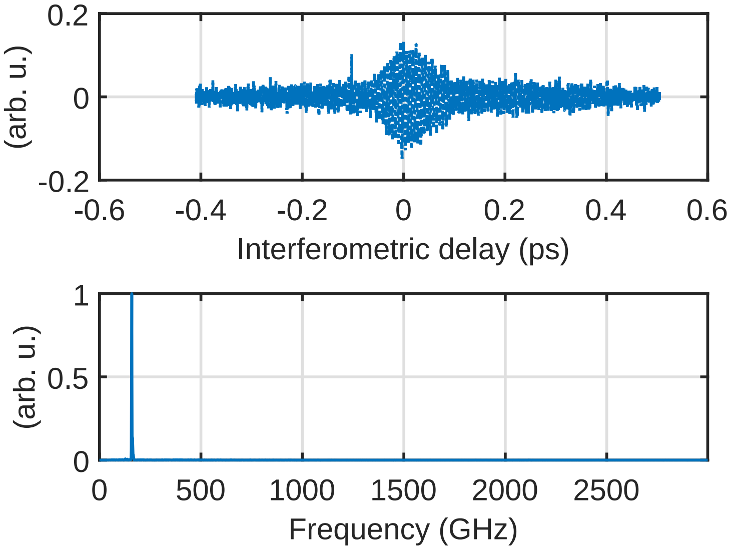

Figure 7.8: Top: Delay-dependent interferogram from an MC-THz generation using a stack of 31 wafers (No. 1). Bottom: the Fourier transform of the interferogram. The central frequency of the THz is 159.4 GHz with a bandwidth of 1.7 GHz.

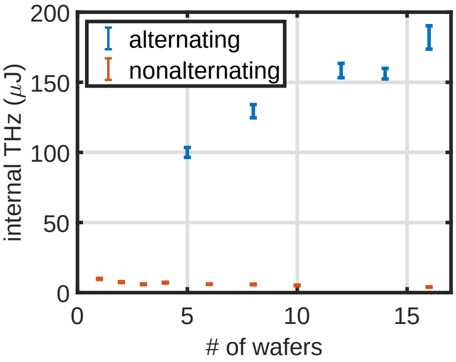

Figure 7.9: Comparing the length-dependent MC-THz generation in two different configurations with alternating and non-alternating c-axis orientation.

The mechanism behind in alternating case is the QPM, which provides narrowband phase-matched. In the non-alternating case, some signal is generated when the crystal length is shorter than the coherence length.

Additionally, the NIR spectra after MC-THz generation for 16 wafers were observed and are given in Fig. 7.10a for the non-alternating case and in Fig. 7.10b for the alternating case. As expected, there is a clear spectral broadening due to the THz generation for the alternating case.

7.2 PUMP RECYCLING EXPERIMENTS AT RT USING WAFERS NO. 1

Although, so far, the best results for the required narrowband MC-THz generation were achieved by the optical DFG; however, the efficiencies are still

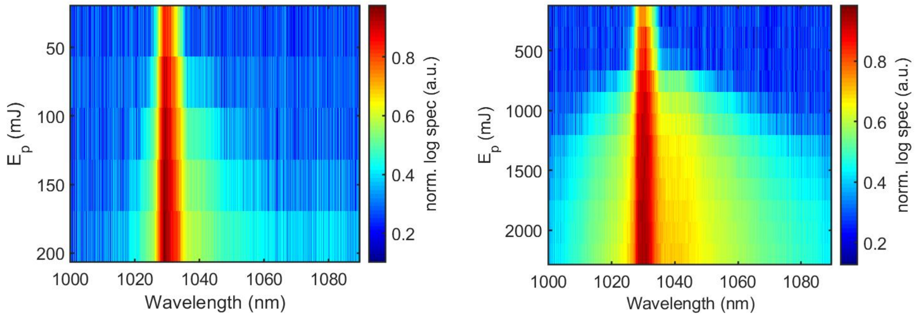

(a) non-alternating (b) alternating

Figure 7.10: Input energy dependent NIR optical spectra taken after MC-THz generation with a) non-alternating wafers and b) alternating wafers.

below percent level. This means the driving NIR laser still has plenty of energy after the MC-THz generation, which is confirmed with laser transmission measurements (e.g., see Fig. 7.14). Taking into account that the laser system can deliver up to 200 mJ pulse energy, it is very attractive to reuse the laser beam after the MC-THz generation.

In this section, two different approaches were tried to target exactly this issue:

- Placing multiple wafer-stacks in series and characterizing the MC-THz generation after each stack as well as at the end of the series (Section 7.2.1).
- Reflecting the laser beam back into a single wafer-stack (Section 7.2.2).

Note: In every experimental setup, only the THz beam generated from the last stack is imaged, using two TPX-lenses, into the detector.

7.2.1 *Stacks in series*

In the first approach, the wafer stacks were placed in a serial arrangement, through which the NIR laser beam was sent and consecutively reused. First, the MC-THz generation was investigated in a 14 wafer stack. This is exactly the same configuration as the previous experiments as illustrated in Fig. 7.11(a). In this case, the input NIR energy dependent MC-THz yield is shown in Fig. 7.12a (blue) and the correlated peak fluence dependent efficiency in Fig. 7.12b (blue). A maximum CE of 0.08% was achieved using a maximum peak fluence of 350 mJ/cm^2.

In the next step, the first 14 wafers-stack was moved 33 cm towards the laser source, and a second 10 wafers-stack was mounted at the THz detection position. The MC-THz yield was measured for the same NIR input energies from the previous scan. The results are plotted in Fig. 7.12a (red). By calculating the internal CE, the losses in the first stack are taken into account and shown in Fig. 7.12b (red). In this case, the efficiency of two stacks in series

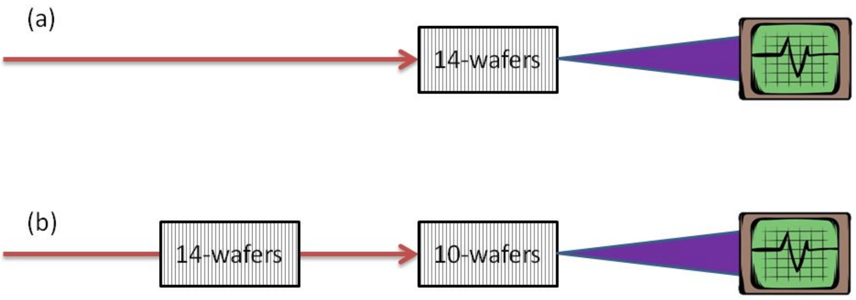

Figure 7.11: Schematic drawing of stacks in series experiments: a) standard MC-THz generation with 14 wafer in single stack, b) two stacks in a row. Note: In every experimental setup, only the THz beam generated from the last stack is imaged, using two TPX-lenses, into the detector.

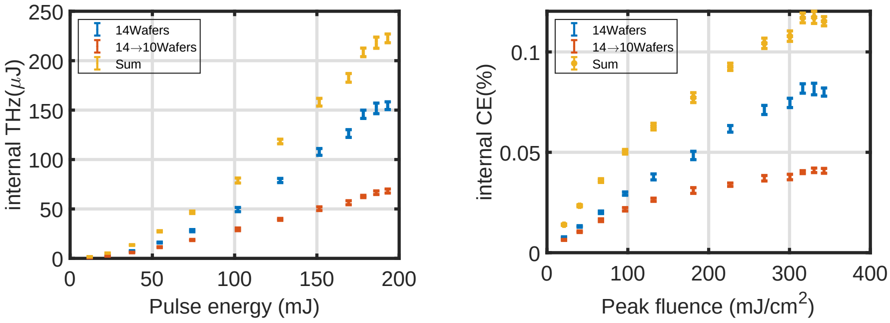

(a) (b)

Figure 7.12: a) The NIR input energy dependent MC-THz yields after a single stack of 14 wafers (blue), after two stacks (with 14 then 10 wafers, red) and arithmetic sum of both (yellow) at RT. b) Corresponding peak fluence dependent internal efficiency at RT.

was lower than in the case of a single stack due to the accumulated linear and nonlinear spectral phase in NIR pulse [42].

These results are similar to the theoretical predictions given by Ref. [42], also discussed in Section 2.6. If the MC-THz could be extracted after each stack, as discussed in Ref. [42] and Section 2.6, then the total amount of generated MC-THz could be improved around 45% compared to the single stack. In this case the total efficiency was increased from 0.08% to 0.12% at the maximum peak fluence of 350 mJ/cm^2 (Fig. 7.12b (yellow)). Note: The generated MC-THz from the first stack is not imaged into the second stack.

7.2.1.1 *Varying the distance between two stacks*

During the above experiments, the distance between two stacks was set 33 cm (Section 7.2.1). Now, another measurement has been performed to investigate the influence of the distance between the stacks on MC-THz generation. The laser pulse energy was fixed to 95 mJ, and the separation of both stacks were varied by moving the second stack towards the laser source. The results of this measurement are depicted in Fig. 7.13

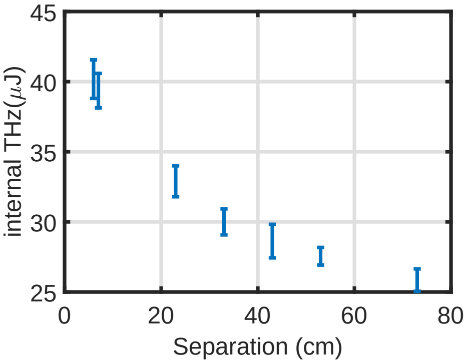

Figure 7.13: Generated MC-THz energy after two stacks (14 and 10 wafers) as a function of stack separation.

The minimum distance was set roughly to 7 cm, which should be enough to separate the THz and the laser beam by a THz output-coupler, as suggested in Ref. [42] before sending the laser into the next stack. By decreasing the distance from 33 cm down to 7 cm, the THz signal could be increased 34%. A possible reason might be, as the distance between the stacks decreases, more THz is coupled into the second stack. This will be investigated in Section 7.2.2.1.

7.2.1.2 *Three wafer-stacks in series*

Even after the 2nd-stack, the NIR laser beam was only 15% reduced (see Fig. 7.14 (blue)), at the maximum input energy of 180 mJ. Hence, it was decided to increase the number of stacks to three. Since the number of wafers were limited, the following wafer numbers were chosen: 12, 12 and 10 wafers. As illustrated in Fig. 7.15, three different measurements were performed.

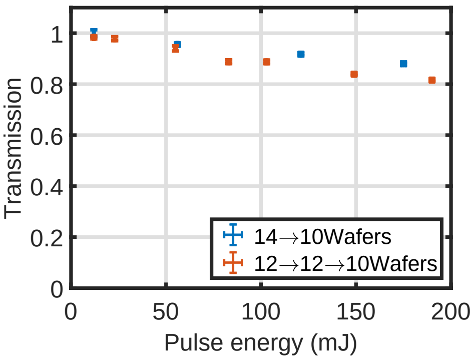

Figure 7.14: Input energy dependent NIR transmission after two stacks (blue) and three stacks (red).

(a) Single stack: the conventional approach, one stack with 12 wafers.

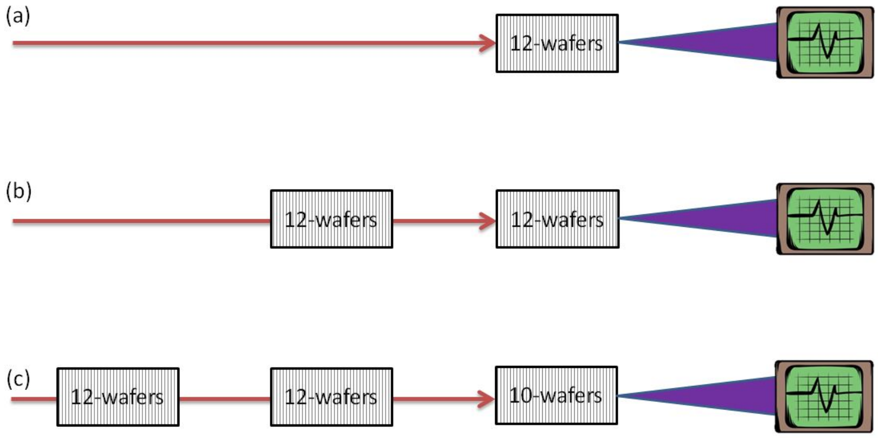

Figure 7.15: Schematic drawing of stacks in series experiments: a) standard (12 wafers) b) two stacks (12 wafers and 12 wafers) in a row c) three stacks (12 wafers, 12 wafers and 10 wafers) in a row. Note: In every experimental setup, only the THz beam generated from the last stack is imaged, using two TPX-lenses, into the detector.

(b) Two stacks: two stacks have the same wafer numbers of 12. The distance between the stack was set around 10 cm, which is enough to install a THz output-coupler.

(c) Three stacks: two stacks with 12 wafers are moved towards the laser source, and the 3rd stack with 10 wafers was installed at THz detection position. The distances between the stacks were set around 10 cm.

The results of these measurements are summarized in Fig. 7.16a & 7.16b. The MC-THz yield decreased with increasing stack number. However, the total MC-THz energy could be doubled compared to the single stack and

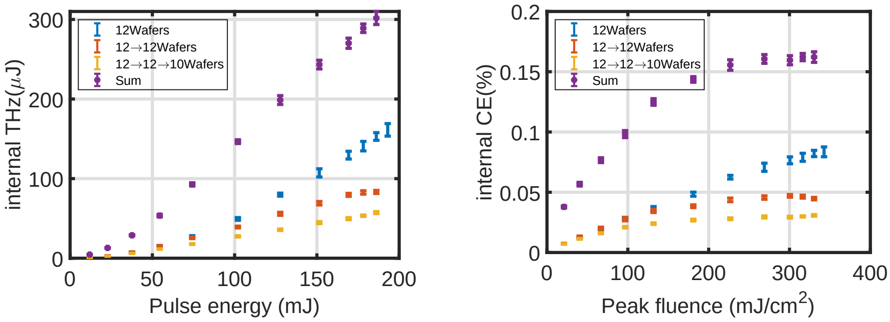

(a) (b)

Figure 7.16: a) The NIR input energy dependent MC-THz yields after a single stack with 12 wafers (blue), after two stacks (with 12 then 12 wafers, red), after two stacks (with 12 then 12 then 10 wafers, yellow) and arithmetic sum of them (dark purple) at RT. b) Corresponding peak fluence dependent internal efficiency at RT.

reached a final value of 0.3 mJ, which corresponds to an internal CE of 0.16% (Fig. 7.16a and Fig. 7.16b, dark purple).

The approach reusing the pump gives the possibility of increasing the total conversion efficiency from optical-to-THz and was theoretically discussed in [42]. By designing an appropriate MC-THz output coupler, the MC-THz and optical pulse can be separated after each stage, and the generated MC-THz can be either added up coherently or used directly. For example, there is a linac design, which has more than one MC-THz input. Another approach would be to use a THz parabolic mirror with a hole in the middle, separating the MC-THz from the NIR optical beam. In this way, the MC-THz could be separated from each stack.

In the future, after each stack, the dispersion of the NIR laser can be characterized and compensated before sending it into the next stack, which would increase the efficiency of the THz generation as predicted in the numerical simulations [42].

7.2.2 *Back-reflected* seeded *MC-THz generation*

Since the wafers have no anti-reflection coating for the THz frequency, the generated MC-THz is partly reflected from the last wafer due to the refractive index changes from the stack into the air (Fresnel reflection). Thus, the back-reflected MC-THz can be used as a seed for the recycled optical beam. This phenomenon was investigated in three experiments, for three stacks with different wafer numbers of 10, 20, 30, which is illustrated in Fig. 7.17. The same THz-detection-system, as in previous experiments, was utilized.

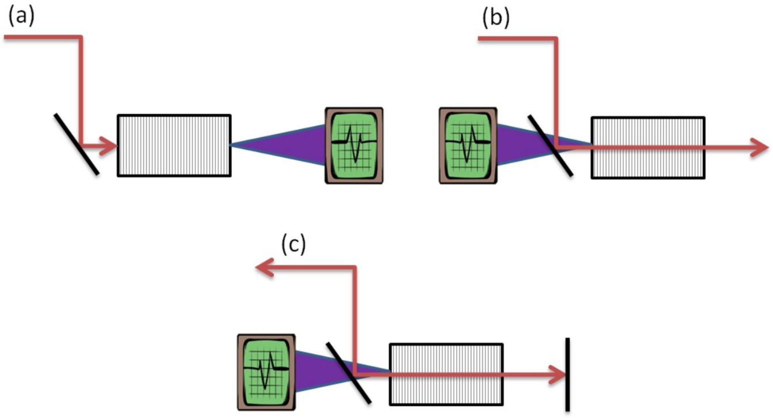

Figure 7.17: a) Standard MC-THz generation with a single stack. b) Measuring the amount of MC-THz in backward direction after a single pass of the NIR optical beam. c) Measuring the amount of MC-THz in the backward direction after reflecting the NIR optical and MC-THz beams back into the stack.

The results of the three experiments are described below:

(a) Standard MC-THz generation procedure (Fig.7.17a): the energy dependent MC-THz (Ω_{forwd}) yield was measured for three stacks with different wafer numbers. Using the same material losses from the Table 7.2, the internal THz energies (see Fig. 7.18a) and from them calculated the internal efficiencies (see Fig. 7.18b) are determined.

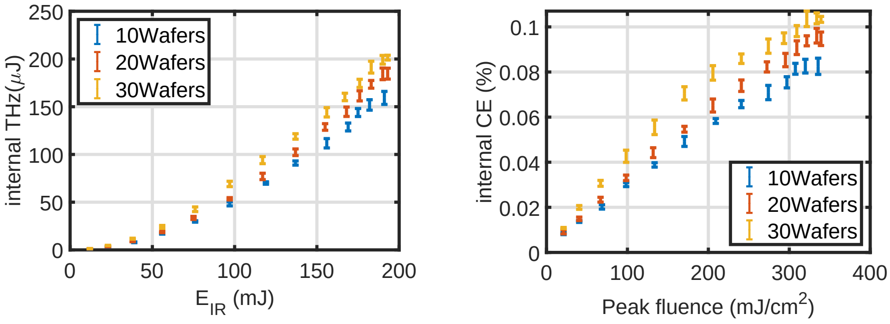

(a) (b)

Figure 7.18: Standard MC-THz generation procedure: the laser input energy dependent MC-THz yields in stacks with different wafers numbers at RT. b) Corresponding peak fluence dependent internal efficiency at RT.

(b) Determining the amount of backward-generated MC-THz ($\Omega_{bckwd}/2\pi \sim$ 60 GHz) (Fig.7.17b): the THz imaging system and the THz detector were mounted behind the HR-45° mirror. The MC-THz signal was measured as a function of NIR laser pulse energy (Fig. 7.19a). This MC-THz signal consists of back-reflected ($\Omega_{forwd}/2\pi \sim$ 160 GHz) and backward-generated MC-THz ($\Omega_{bckwd}/2\pi \sim$ 60 GHz). Since they differ in frequency, due the sign change in the phase matching condition, the results are not calibrated. Using the Fresnel's reflection of 44.4% and the absorption losses given by Beer–Lambert law ($\alpha \sim$2.5 cm^{-1} [46]), the back-reflected signal (Ω_{forwd}) is calculated. By subtracting this value from the measured values in Fig. 7.19a, the Ω_{bckwd} is calculated (Fig. 7.19b).

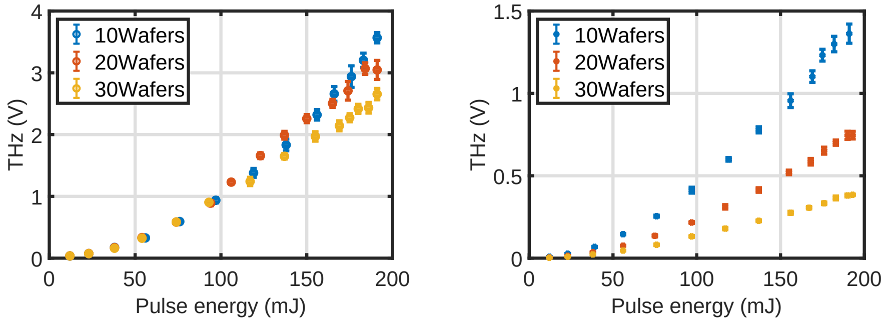

(a) (b)

Figure 7.19: a) The backward-generated MC-THz (both Ω_{forwd} and Ω_{bckwd}) as a function of input NIR energy using the experimental setup Fig. 7.17(b)) at RT. b) From Fig. 7.19a the calculated reflected MC-THz energy (Ω_{bckwd}) at RT.

Additionally, in this configuration, the NIR laser transmission was measured as a function of the input energy for the three wafer-stacks (see Fig. 7.20), which was used by calculating the internal CE for the recycling case (Fig. 7.17(c)).

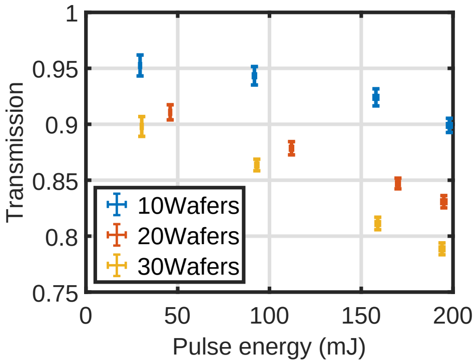

Figure 7.20: Input energy dependent NIR transmission after the stacks with different wafer numbers (see label).

(c) Reflecting the NIR and MC-THz beams back into the stack (Fig.7.17c): The laser beams were reflected back into the wafer-stack using a HR-0° mirror. After subtracting the calculated backward-generated MC-THz (Ω_{bckwd}), the energy dependent MC-THz yield is determined (Fig. 7.21a). This is a quasi-seeded MC-THz generation process. In this case, the amount of generated MC-THz is maximum for 10 wafers and for 30 wafers the energy drops to less than half of the single pass forward case (see Fig. 7.18a). However, the recycled NIR laser input energy dropped as well as shown in Fig. 7.20. Therefore, the internal CE for the recycled beam stays similar at around 0.09%. For 20 wafers, it reaches value of up to 0.19%. For the results with 10 wafers, the MC-THz energy was

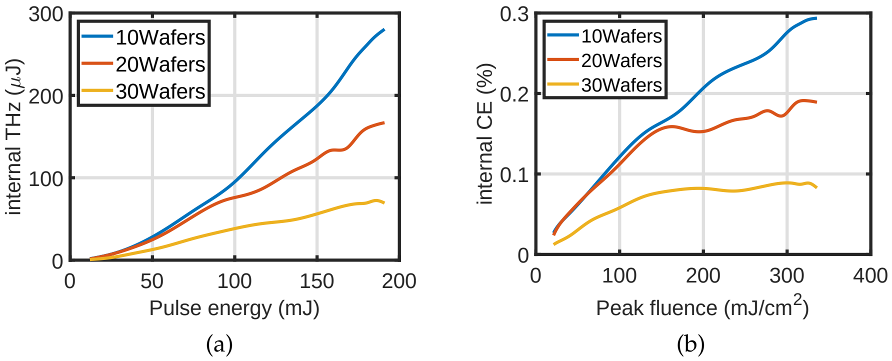

(a) (b)

Figure 7.21: Seeded MC-THz generation (Fig. 7.17(c)): a) the NIR laser input energy dependent MC-THz yields in stacks with different wafer numbers (see label) at RT b) Corresponding peak fluence dependent internal efficiency at RT.

almost doubled compared to results from the single pass forward case (Fig. 7.18a) and the internal CE reached a value of up to 0.29%.

In summary, the results of the seeded MC-THz generation using 10 wafers provide the best conversion efficiency (experiment Fig. 7.17c). However, one question remains, MC-THz is reflected from both the last wafer and from the mirror (see Fig 7.17c); which source is more important? Because the MC-THz has a much larger refractive index inside the stack compared to air, the MC-THz beam divergence is much lower inside the stack. Therefore, it would be expected that the "seeded" MC-THz is largely generated from the back reflection on the last wafer in comparison to the more divergent MC-THz generated from the back reflection of the mirror. In the next section, it will be experimentally confirmed that the seeded MC-THz is generated from the last wafer air surface.

7.2.2.1 *Experimental determination of the origin of the* seeded *MC-THz*

To characterize the amount of back-coupled MC-THz energy from the mirror compared to back reflections from the last wafer in experiment Fig 7.17c, another measurement was carried out. Three different configurations were compared as depicted in Fig. 7.22 and summarized below (a-c).

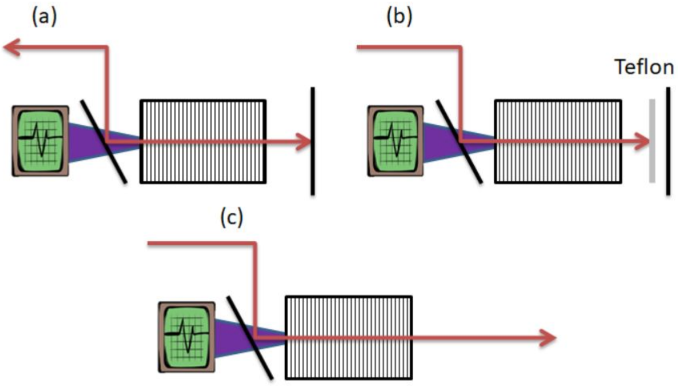

Figure 7.22: A schematic drawing for the three different measurements: a) reflection and recoupling of both NIR optical and MC-THz beams b) reflection and recoupling of mostly the MC-THz beam using a teflon NIR beam blocker c) no reflection or recoupling.

(a) Reflecting both the NIR laser and MC-THz beams (Fig. 7.22a): The THz signal was detected behind the HR-45° mirror, which is the case in all three configurations. The input energy-dependent MC-THz signal was measured for two stack-mirror separation distances of 3, and 13 mm.

(b) Blocking the NIR laser beam and reflecting mostly the MC-THz beam (Fig. 7.22b): In this case, a 1.6 mm teflon shield was inserted between the stack and the mirror to block the NIR laser beam. The MC-THz signal was measured for the same input energies and stack-mirror distances chosen in the previous case (a). Note: The measured THz loss in transmission for the teflon was around 7.5% (Table 7.2).

(c) Both NIR laser and MC-THz beams are not reflected (Fig. 7.22c): In this case, the HR-0° mirror was removed.

The results of these three measurements are summarized in Fig.7.23. As expected, the highest values were achieved for measurement (a), where both NIR and MC-THz were reflected back; and the lowest values were detected for measurement (c), where there was no reflection. In measurement (b), the values were also low, within 10% of the values in measurement c. Thus, it is confirmed, in the case of back-reflected seeded MC-THz generation. The seeded MC-THz is generated mostly from the less divergent MC-THz back reflection from the last wafer, and the back reflection of the NIR beam comes from the adjustable mirror.

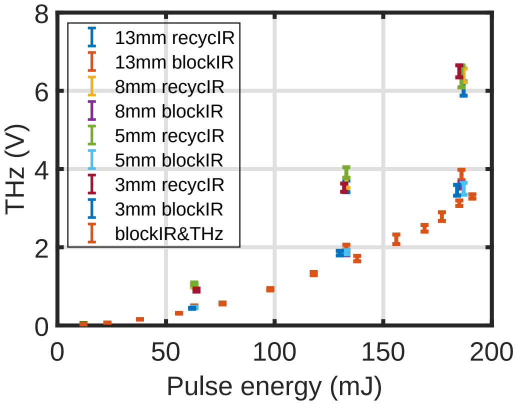

Figure 7.23: Backward direction detected MC-THz for the three different measurements.

7.2.2.2 *Timing between the NIR and MC-THz beams for the back-reflected* seeded *MC-THz generation*

The results from the back-reflected *seeded* MC-THz generation (Section 7.2.2) demonstrate an improvement in the conversion efficiency. This is caused by seeding the MC-THz generation (see Fig. 7.17c). In this case, the NIR laser's group velocity is faster than the MC-THz in the stack. This velocity difference leads to a temporal walk-off, limiting the coherent building up of MC-THz radiation. Therefore, it is critical to optimize the timing between the back-reflected MC-THz and the NIR laser beam. This is achieved by mounting the HR-0° mirror on a motorized translation stage, which enables it to vary the distance between the stack and the mirror.

In these experiments, the NIR laser input energy was fixed to 80 mJ, and the MC-THz was measured as a function of the stage position. The scan was repeated with three different stacks with the following wafer numbers of 10, 20 and 30. The results are not calibrated, and the intensities of the MC-THz are given in arbitrary units (Fig. 7.24(top)). Additionally, increasing the delay to positive values was mechanically not possible.

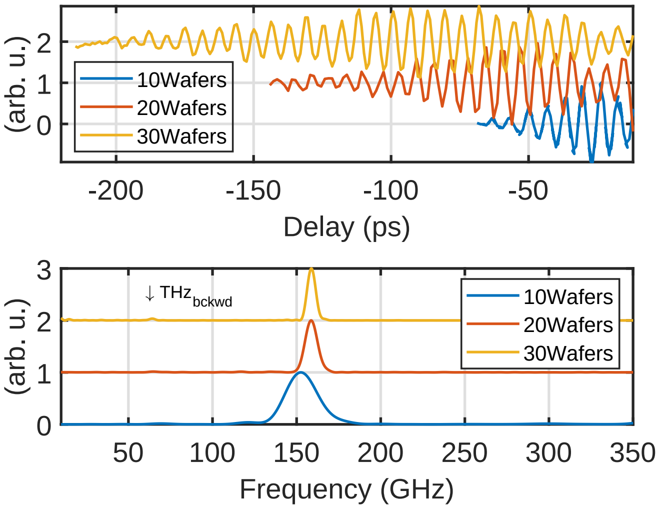

Figure 7.24: Top: The non-calibrated MC-THz signal in arbitrary units as a function of delay between the MC-THz and NIR optical beams for different wafer numbers. Bottom: its Fourier transform. An arrow indicates a small amount of backward-generated MC-THz at ∼ 63 GHz.

By a Fourier transformation, the frequency of the modulation of the MC-THz intensity is determined for each case Fig. 7.24(bottom). This setup acts as a THz interferometer, generating the same central frequency as in the forward direction. The central frequencies of the intensity modulation and its bandwidth (FWHM) are determined and listed in Table 7.3. Interestingly, a small signal from the backward-generated MC-THz signal at 63 GHz is observed (Fig. 7.24(bottom)). As expected, the intensity modulation frequency matches exactly with the frequency of the MC-THz radiation and the bandwidth narrows down with increasing number of wafers.

Table 7.3: The central frequency and bandwidth for different wafer numbers for the scans given in Fig 7.24.

Wafer Number	10	20	30
Central freq. (GHz)	152.5	158.6	158.8
Bandwidth (GHz)	22.1	8.6	5.9

Note: the maximum value of the delay-dependent MC-THz signal shifts with increasing number of wafers (Fig. 7.24(top)). The delay at peak intensity for each wafer number compares very well with the calculated expectation (Table 7.4).

Table 7.4: The measured delay at maximum intensity from Fig 7.24(top)) is compared to the calculated expectation.

Wafer Number	10	20	30
measured (ps)	-27.4±0.4	-56.1±0.4	-89.3±0.4
calculated (ps)	-28.4±0.9	-56.9±1.9	-85.3±2.8

7.2.3 *Characterization of parasitic second-harmonic*

One of the parasitic effects generated in the crystal stack is the 2nd-harmonic of the NIR laser. To characterize the amount of generated 2nd-harmonic, a HR-45° mirror for 1030 nm was used to separate the NIR and its 2nd-harmonic. The energy-dependent 2nd harmonic generation in a stack with 16 and 20 wafers is plotted in Fig. 7.25. The amount of the generated second-harmonic is higher throughout the measurements with 20 wafers. In summary, the amount stays below 2 mJ, which makes roughly 1% of the laser energy.

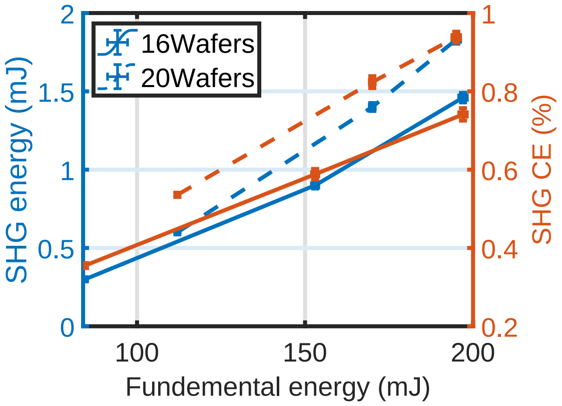

Figure 7.25: The NIR laser input energy dependent generated second-harmonic in a stack with different wafer numbers.

7.3 TESTS OF RECTANGULAR, 200 μM THICK LN WAFERS NO. 2

Tests of LN wafers 200 μm thick (No. 2) are now performed at RT and CT. Since they are thinner than No. 1 wafers, they generate a higher THz frequency and consequently more THz is absorbed within the stack [46]. Thus for good performance, the wafers should be cooled down to reduce the absorption and increase efficiency [38]. In addition, in the previous section, there were technical problems cooling the circular shape of No. 1 wafers. All No. 2 wafers are polished on both surfaces and AR-coated at 1030 nm. The same experimental setup as in the previous measurement was used with the wafers being mounted with alternating c-axis orientation in a custom wafer holder.

7.3.1 *Tests at RT*

The initial tests were performed at RT. The MC-THz yield was measured as a function of laser input energy for different stacks with varying wafer numbers, which was increased in steps of 4 wafers. From the MC-THz yields, the internal CEs were calculated and the results of these scans are depicted in Fig. 7.26. The THz losses from the stack to detector are quantified in Table 7.5, which are determined for different materials using the commercial software THz-TDS. Additionally, the Fresnel losses of 44.4% for the MC-THz radiation were considered.

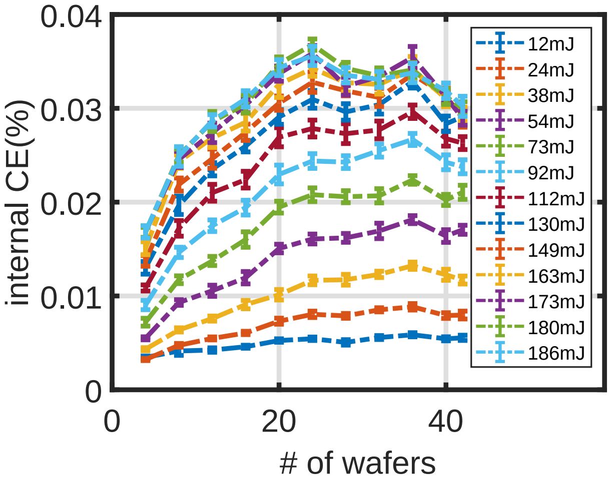

Figure 7.26: The internal conversion efficiency as a function of wafer numbers for different input energies at RT.

Table 7.5: THz losses in different materials: these values are determined using THz-TDS (see Section A.2)

Frequency (GHz)	Teflon (%)	TPX (%)	Polyethylene (%)	Window(%)
250	9	20	32	33
270	2	15	27	33

These results show the length-dependent saturation starts earlier for higher NIR input energy. As an example, in the case of 12 mJ, any saturation is visible throughout the length (42 wafers). At higher input energies, it starts around 24 wafers, where also the highest efficiency of 0.036% was achieved at 180 mJ input energy. In addition to the length-dependent saturation, the fluence dependent saturation is also visible. All the curves, from the three highest input energies from 173 to 186 mJ, produce similar results over all wafer number. One reason for this behavior might be nonlinear effects such as SPM.

7.3.2 *Tests at CT (cryogenic cooling using liquid Nitrogen)*

As expected, due to the higher absorption at higher THz frequencies, the achieved efficiencies at RT (see Fig. 7.26) stayed lower compare to the previous 300 μm No. 1 wafers in Section 7.1.2. In the next step, a stack of 40 wafers (No. 2) was mounted in a vacuum chamber and cooled down cryogenically to liquid nitrogen temperatures. The additional losses from the vacuum window were taking into account for the calculation of the internal MC-THz energy. First, the NIR laser energy-dependent MC-THz yield was measured at RT (Fig. 7.27a) and afterwards at CT (Fig. 7.27b). In both figures,

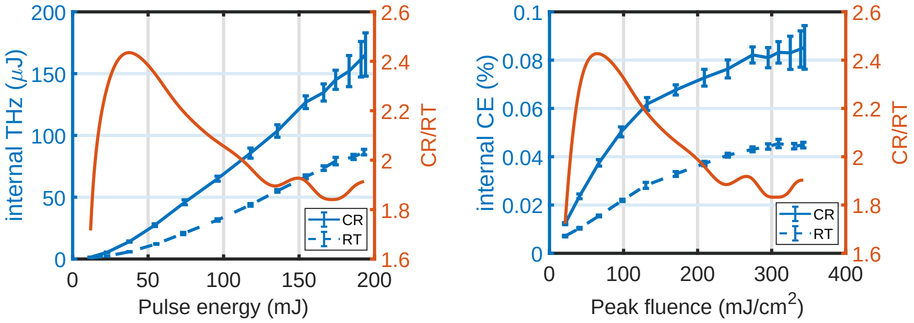

(a) (b)

Figure 7.27: a) The NIR laser input energy-dependent MC-THz yields in a stack of 40 LN-wafers (No. 2) at RT (blue, dashed) and CT (blue, solid), and the CR/RT yield radio (red). b) Corresponding peak fluence dependent internal conversion efficiency.

the dashed and solid blue lines represent the results at RT and CT, respectively. The red solid line shows the improvement factor by the cooling (ratio between CT and RT). At CT, the efficiency could be doubled; the maximum CE increased from 0.045% to 0.086%. The improvement reaches its maximum value of 2.4 around 70 mJ/cm^2 and drops with increasing fluence down to 1.9 and stagnates after 230 mJ/cm^2, where yields saturate at both RT and CT.

Additionally, spectra of the NIR after MC-THz generation were recorded at RT and CT (Fig. 7.28). Both spectra are strongly broadened at higher fluences, which is likely the reason for the observed saturation in the THz generation efficiency.

In addition to the MC-THz generation, the NIR transmission was measured in both cases for different input NIR energies (Fig. 7.29). The results in both cases indicate an energy-dependent reduction of the transmission. So in both cases, the NIR laser beam got absorbed stronger with increasing input energy. Both behave similarly at lower energies, and around 70 mJ/cm^2 the deviation starts to grow and stagnates around ~250 mJ/cm^2. These results show a similar trend as the cooling improvement (CT/RT) factor.

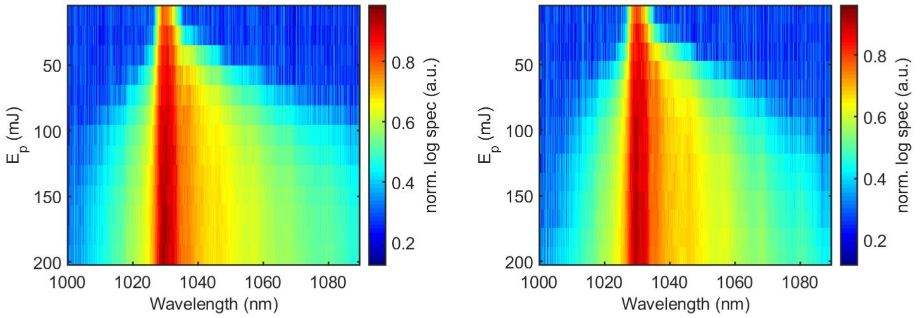

(a) (b)

Figure 7.28: The NIR pulse energy dependent spectra captured after the MC-THz generation at a) RT and b) CT.

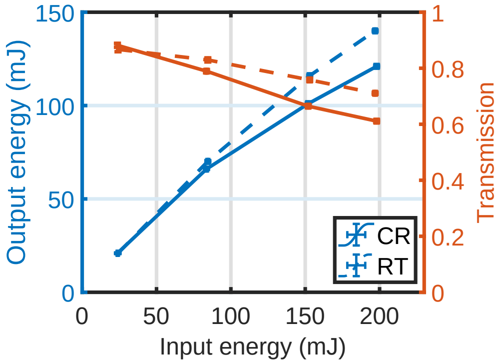

Figure 7.29: Input energy-dependent transmission after the stacks with 40 LN-wafers (No. 2) at RT (dashed) and CT (solid).

7.3.3 *Central frequency of generated THz*

The MC-THz central frequency was determined for both cases at RT and CT using a THz interferometer. The results of these measurements are shown in Figs. 7.30a and 7.30b for RT and CT, respectively. The analysis of data shows

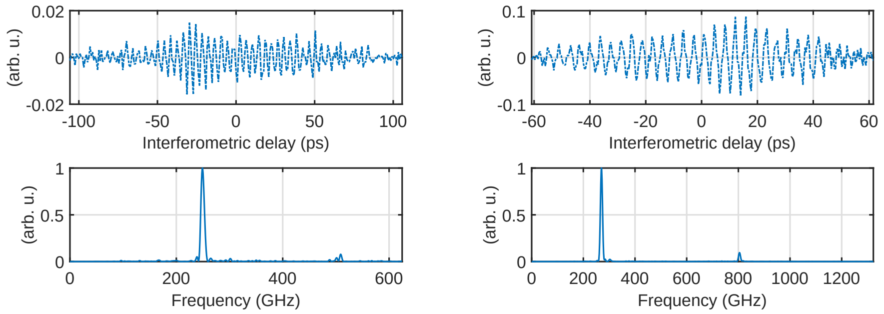

(a) RT (b) CT

Figure 7.30: The results of THz interferometry in LN-wafer stack measured at a) RT ($\nu_0 = 250\,\text{GHz}$) and b) CT ($\nu_0 = 270\,\text{GHz}$).

that the central frequency of the generated MC-THz is around 250 GHz and 270 GHz for RT and CT, respectively. Due to the temperature-dependent THz refractive indices, the phase-matched frequency changes. The frequency shift due to the cooling is similar to the case of large aperture single-crystal MgO:PPLN (Fig.6.14), which shows that the stack could be cooled down similarly.

7.4 TESTS ON KTP WAFERS (NO. 3) AT RT

The advantages of the wafer concept are introduced at the beginning of this chapter. In summary, it allows extending the aperture size of the crystals to the scales, which is not possible to achieve using the conventional poling method [48].

LN crystal has several advantages, such as high nonlinear coefficient, well-established production process, and its large availability due to extensive usage in telecommunications. However, it has a crucial drawback for the MC-THz generation, namely its high absorption coefficient in the THz range [46]. Typically, it is cooled down to reduce absorption [38], which unfortunately lower its damage threshold as well. Recent results have shown that Potassium titanyl phosphate (KTP) seems to be a promising alternative to LN due to its crystal properties listed in Table 2.1 and higher damage threshold (× 3 more than LN) [45] (also see Section A.1).

Unfortunately, getting a PPKTP with an aperture size of larger than 1 mm^2 is currently very difficult. The manual stack wafers concept can solve this issue, allowing the aperture size to scale up to several centimeter ranges. Moreover, its low refractive index ratio between the NIR and THz (Table 2.1) allows for a greater wafer thickness, which in turn simplifies production. For example, in the case of LN, 200 μm is the smallest achievable thickness of many manufacturers.

In this section, the wafer concept will be tested for the first time using KTP. The dimension of the wafers are as follows: $10 \times 10 \times 0.25\,\text{mm}^3$. Both surfaces of the wafers are polished and AR-coated at 1030 nm. Two corners of the wafers are slightly cut to indicate the direction of the c-axis of the crystal. The wafer shape was chosen to be square, specifically to achieve a better cooling using a home-built wafer-stack-holder.

7.4.1 *MC-THz generation at RT*

After confirmation of the orientation of the c-axis of the wafers, the wafers were manually stacked with alternating c-axis orientation into the wafer holder. The alternation of the wafers was double-checked using a microscope. The same experimental setup was utilized as in the previous MC-THz experiments. The number of wafers was increased from 4 to 22 wafers. For each wafer number, data were acquired for four different input energies.

The results of the scans are summarized in Fig. 7.31a. The internal MC-THz energies were calculated using the material and the Fresnel losses (see

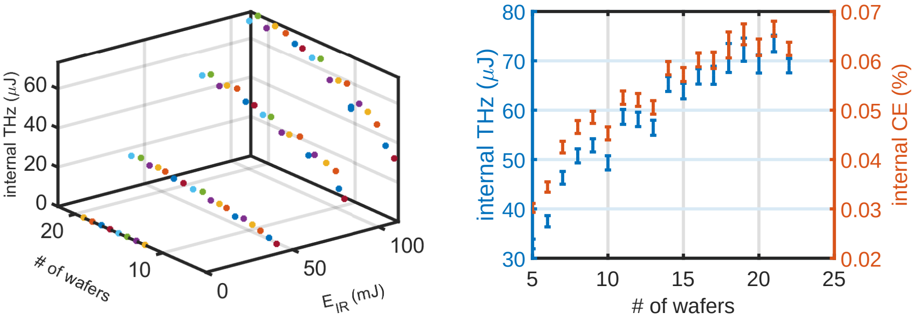

(a) (b)

Figure 7.31: a) MC-THz yield as a function of laser input energy (E_{IR}) and wafer numbers at RT. b) Summarized results: MC-THz yield and conversion efficiency at maximum laser peak fluence as a function of wafer number.

Table 7.6) based on the THz interferometry (see Section 7.4.2). In Fig.7.31b, the internal MC-THz energy reaches a value of up to ~75 μJ that corresponds to an internal CE of 0.067%. This scan was stopped at that point because the number of available wafers was 22. It is important to note that these results the highest efficiencies at RT compared the results to LN-wafers as well as large aperture PPLN.

Table 7.6: THz losses in different materials: these values are determined using THz-TDS (see Section A.2)

Frequency (GHz)	Teflon (%)	TPX (%)	Polyethylene (%)
355	4	9	37

7.4.2 *Length-dependent central Frequency*

The frequency of the MC-THz radiation was determined by THz interferometry, using the same setup as in the previous sections. The interferograms were measured for different number of wafers: 5, 10, 15 and 22 (Fig.7.32a); their corresponding spectra are shown in Fig.7.32b. The central frequencies and the relative bandwidth are summarized in Table7.7. As expected from theory (see Eq. (2.15)), the relative bandwidth decreases with increasing stack length.

7.4.3 *Outlook based on the initial tests of KTP wafers No. 3*

The results of this Section 7.4 appear very promising. Using the available 22 wafers, a maximum internal CE of 0.067% is reached, which is the highest results obtained at RT, and there was no clear indication that saturation at this length was achieved.

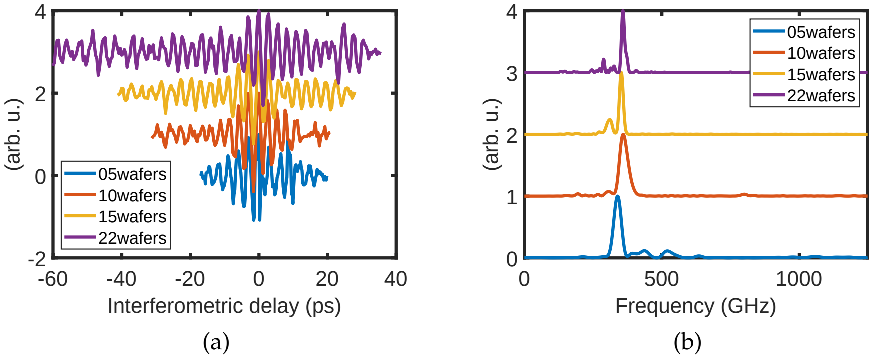

(a) (b)

Figure 7.32: a) Delay-dependent THz interferometer trances from stacks with different wafer numbers, b) corresponding spectra.

Table 7.7: The central frequency and relative bandwidth from wafer stacks with different wafer numbers.

Wafer Number	5	10	15	22
Central freq. (GHz)	338.8	358.3	354.1	358.3
rel. Bandwidth (%)	9.4	10	4.8	3.7

Unfortunately, during the preparation of the CT measurements, the AR coating of the wafers was damaged. Therefore, measurements with these wafers could not be continued.

7.5 TESTS ON KTP WAFERS (NO. 4) AT RT & CT

In this last section, other KTP wafers from another manufacturer were utilized. Dimensions of these wafers are the same as the previous KTP wafers: $10 \times 10 \times 0.25\,\mathrm{mm}^3$, and both surfaces are polished and AR coated. The same experimental setup was utilized as with the previous wafers. A new waferholder for the CT scans was designed, which can be attached to the coldfinger in the vacuum chamber.

All available 38 KTP wafers, stacked with alternating poling in the wafer holder, were attached to the cold finger in the vacuum chamber. The chamber was pumped down to 10^{-5} mbar level. First, the laser peak fluence is increased slowly at RT while observing the beam on teflon shield with a camera. The laser peak fluence is increased up to $330\,\mathrm{mJ/cm^2}$ and efficiency of 0.045% was reached (Fig. 7.33a). No beam distortion was observed at this peak fluence. Afterwards the stack was cooled down to CT, using liquid nitrogen. Similarly, as at RT, the peak fluence was slowly increased while observing the beam profile. Again, no beam distortion was observed. By calculating the values of the frequency-dependent material losses (see Table 7.8), the CE was calculated, and the maximum CE at CT was almost tripled compared to RT and reached a value of 0.13% (Fig. 7.33b).

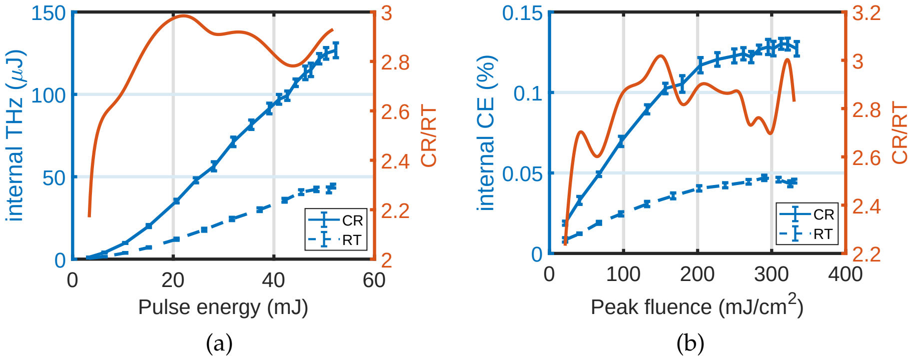

(a) (b)

Figure 7.33: a) The NIR laser input energy-dependent MC-THz yields in a stack with 38 KTP-wafers at RT (blue, dashed) and CT (blue, solid), and ratio (CT yield/RT yield, red). b) Corresponding NIR laser peak fluence dependent internal conversion efficiency.

Table 7.8: THz losses in different materials: these values are determined using THz-TDS (see Section A.2)

Frequency (GHz)	Teflon (%)	TPX (%)	Polyethylene (%)
324	6	9	32
302	2	9	37

In addition, the energy-dependent NIR optical spectra after the interaction were measured at RT and CT (Fig. 7.34). In both cases, the spectra are broadened with increasing input NIR energy, as in the previous cases. However, a difference is observed compared to LN wafers, especially at CT; the spectrum is most broaden around 70 mJ and starts to narrow with higher input energies. Similar behavior was observed with commercial Rb:PPKTP in the multiline MC-THz experiment (see Fig. 5.17).

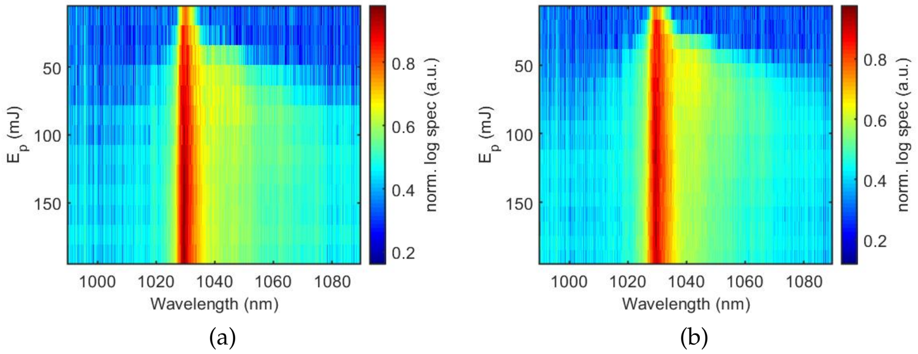

(a) (b)

Figure 7.34: The NIR pulse energy-dependent spectra taken after the MC-THz generation at a) RT and b) CT.

7.5.1 *Determining the central frequency of MC-THz at RT and CT*

Finally, using the THz interferometry, the central frequencies both at RT and at CT were determined. The measurements were with 38 wafers performed at RT (Fig.7.35a) and at CT (Fig.7.35b). The central frequency of 302 GHz at RT shifts to 324 GHz at CT. The relative bandwidths are 5% and 3.5% at RT and CT, respectively.

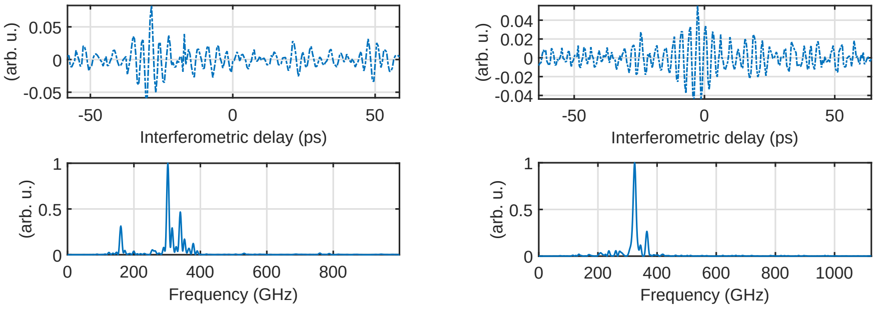

(a) (b)

Figure 7.35: Upper: The measured delay dependent interferometric autocorrelation trace measured in a stack with 38 KTP wafers at a) RT b) CT. Lower: From interferometric trace, the calculated THz spectra at a) RT ($\nu_0 = 302\,\mathrm{GHz}$) and b) CT ($\nu_0 = 324\,\mathrm{GHz}$).

7.6 DISCUSSION OF RESULTS

In this chapter, the wafer concept with manually stacked wafers for both LN and KTP wafers was investigated. Firstly, MC-THz pulse energies of ~200 μJ and efficiencies of ~0.1% at a central frequency of 160 GHz have been demonstrated at RT (Fig. 7.6). As expected, the efficiency dropped to the ~0.04% level at RT by increasing phase-matched THz frequency to 250 GHz, due to the increase of the absorption coefficient (see Section 7.3). Thereafter, in order to again prove the wafer-stack concept using LN wafers, in Fig. 7.9, a comparison in MC-THz generation between alternating and non-alternating wafers demonstrated an improvement factor of 45 using 16 LN wafer pieces.

Next, in Section 7.2, two different techniques of using wafer stacks were implemented: (i) wafer stacks in a serial configuration, and (ii) a single wafer stack in a back-reflected seeded configuration. Both methods improved conversion efficiency. In the serial stack configuration, the number of stacks increased up to three (12-12-10, wafer number), and the total summed efficiency of ~0.16% was demonstrated (Fig. 7.16b). This result is confirmed using numerical simulations, predicted by [42]. After each wafer stack, the efficiency drops, due to the spectral broadening and accumulation of nonlinear spectral phase, as shown by [42] (as discussed in Section 2.6 of this thesis). Using a single wafer stack, in a back-reflected seeded configuration (Fig. 7.17(c)), a conversion efficiency of ~0.3% was reached for a single stack of 10 wafers (Fig. 7.21b). This remarkable result is generated through THz seeding, as demonstrated in Section 7.2.2. An even higher conversion efficiency could be achieved, if the spectral broadening and accumulating nonlinear phase of the NIR pump pulse could be compensated, again theoretically demonstrated by [42].

Cooling of a single wafer stack was demonstrated in Section 7.3, providing 150 μJ of MC-THz energy at 0.27 THz, at CT (Fig. 7.27a). In this case, an increase of the efficiency by 1.9 was achieved after cooling the stack from RT to CT (Fig. 7.27b).

Finally, KTP wafers are tested in Sections 7.4 and 7.5. Efficiencies up to $\sim$0.07% were demonstrated at 350 GHz with 22 KTP wafers at RT (Fig 7.31b). The length dependent THz-interferometry shows a bandwidth narrowing with increasing wafer number (Table 7.7). Although the KTP has a higher damage threshold than LN, the AR-coating on these wafers was damaged. Therefore, no cryogenic measurements on these wafers were performed. Especially for the stacked wafer concept, the AR-coating for NIR plays a crucial role since the stack consists of several surfaces; each of them introduces Fresnel losses. Thereafter, KTP wafers (also AR coated from another manufacturer) were cooling to CT and the conversion efficiencies tripled compared to the RT result, and the maximum efficiency was $\sim$0.13% (Fig. 7.33b). Similar conversion efficiencies are obtained with PPLN using optical rectification [6]; thus, the stacking of AR-coated KTP wafers provides a good method for increasing the aperture of periodically poled KTP.

8

CONCLUSION AND OUTLOOK

In order to fulfill the MC-THz requirements of the AXSIS project high repetition rate, 20 mJ at 0.3 THz with hundreds of picosecond pulse duration, (see Introduction 1), high efficient laser-driven MC-THz sources were developed and investigated.

Prior to this work, the highest conversion efficiency (CE) of 0.24% was reached using a chirped and delay (C&D) technique with a Ti:sapphire laser system [21]. In this case, the laser system was a high energy Ti:sapphire laser. These types of lasers are limited to a few Hz in repetition rate, which would basically limit the operation rate of the whole AXSIS system, and consequently, the final photon flux of x-rays. Additionally, to achieve this relatively high CE, phase compensation was required to extend the spectral contribution to the CE.

Recently, numerical simulations by Ref. [42] predicted percent level CE with MgO:PPLN using a pump-laser at 1 μm with a two-spectral-line spectrum, where the separation of the two lines is given by the THz frequency. Therefore, the main aim of this thesis was to build such a laser and test the CE on MgO:PPLN and Rb:PPKTP. In Chapter 4, a Yb-based two-line laser for efficient THz generation was designed and build. It was seeded by two CW-lasers; the front-end part of the laser provides optical pulses with tens-of-nanojoule pulse energies and tunable pulse durations and shape consisting of two or more spectral narrow lines. These pulses were successively amplified to 20 mJ by a regenerative (Section 4.2) and four-pass-amplifier amplifier (Section 4.3). The quantum defect of Yb-based lasers is much smaller than Ti:sapphire laser systems, thereby generating less heat, and subsequently can be scaled to the much higher powers and repetition rates required by the AXSIS project. Although the final pulse energy of the developed system needs to be scaled to higher energies, the degree of scaling depends on the achieved CE, which was investigated in the next chapter.

In Chapter 5, the CE experiments were performed on MgO:PPLN and Rb:PPKTP, exploring the parameter space such as intensify, poling period, temperature, THz wavelength and phase matching sensitivity. Many of these parameters scale according to the analytical description in Section 2.3, even though this description does not include parametric cascading effects (Section 2.5). The key results of this chapter was summarized in Section 5.4: world record CEs were achieved using MgO:PPLN of 0.49% at 0.29 THz and 0.89% at 0.53 THz with this two-line laser system (Fig. 5.18). These results compare remarkably good compared to numerical simulations of Ref. [42] (see Section 5.4 for a detailed comparison between experiment and simulation).

Based on these record CE values, scaling of these results requires not only scaling up a high energy, Yb-based, driving-laser, but also exploring the possibility of large aperture crystals. Therefore in Chapters 6 and 7, large aperture crystals for both MgO:PPLN and Rb:PPKTP were investigated using a high energy, commercial laser, producing 200 mJ with a pulse duration of 500 fs at 1030 nm. Using this driving laser, it was only possible to use the older method of optical rectification (see Section 2.3.1 for details), which should have a lower CE compared to the multiline laser source.

In Chapter 6, large aperture MgO:PPLN crystals were used with a size of $10 \times 15\,\mathrm{mm}^2$. They were produced by the group of Prof. Taira [19]. With these crystals and the above mentioned commercial laser, a CE of 0.29% at 0.35 THz was achieved with a pulse energy of 260 μJ at 143 K. This is the highest known CE value using OR. Here, the maximum CE was not achieved at liquid nitrogen temperature (77 K), but at 143 K (Fig. 6.10). Usually, in MC-THz experiments, the absorption at THz wavelength dominates, but in these crystals, significant absorption of the optical laser was also observed below 150 K (Fig. 6.11), therefore the maximum CE peaked at 143 K. Finally, as a reminder, the largest commercial available PPLN crystals have an aperture size of only $4 \times 4\,\mathrm{mm}^2$. Both commercial and the crystals from Prof. Taira require the application of static electric fields in their production to reverse ferroelectric domains in a periodic fashion on a single crystal. This method becomes increasingly difficult for large aperture crystals. However, the AXSIS project might require apertures of even greater size, so the next step is to investigate stacked wafers.

In Chapter 7, stacks of individually anti-reflection coated wafers were tested with aperture sizes of 1″ for LN and $10 \times 10\,\mathrm{mm}^2$ for KTP. The advantage of this process is that some crystals can be grown and cut into the required thickness (half a poling period length) and can be stacked to a periodically poled "crystal". Both LN and KTP wafer stacks were successfully tested. In the case of LN wafers, pulse energies of 200 μJ with a CE of 0.1% at 0.16 THz (Fig. 7.6), and in the case of KTP, pulse energies of 130 μJ with a CE of 0.13% at 0.34 THz (Fig. 7.33) were achieved. In both case, CE growth is linear in both fluence and crystal length (as expected from analytical expressions, see Section 2.3.1, Eq. (2.17)).

Stacks of wafers were also used to explore some new approaches to MC-THz generation. In particular, with LN wafers, two novel experiments were performed: multi-stage wafer-stacks in a serial configuration with multi-output THz radiation (Fig. 7.15(c)), and back-reflected seeded MC-THz generation (Fig. 7.17(c)). Both methods improved the efficiency of the MC-THz generation, compared to a single stack.

In the serial stack configuration, the number of the stacks increased up to three (12-12-10, wafer number) with the corresponding three outputs, and a total summed efficiency of ~0.16% was demonstrated (Fig. 7.16b). The basic trend of this result is confirmed using numerical simulations, predicted by [42]. After each wafer stack, the output efficiency drops, due to the spectral broadening and accumulation of nonlinear spectral phase, as shown by [42] (see Section 2.6 for more details).

Next, a single stack of 10 wafers in a back-reflected seeded configuration (Fig. 7.17(c)) achieved a conversion efficiency of $\sim 0.3\%$ (Fig. 7.21b). This remarkable result is generated through THz seeding, as demonstrated and discussed in Section 7.2.2. Even more efficiencies could be achieved, if the spectral broadening and the accumulation of nonlinear phase of the optical pump pulse could be compensated. Finally, a redesign of the original setup (Fig. 7.17(c)), which exploits the advantages of a back-reflected seeded configuration is given in Fig. 8.1. Compared to a single pass through a single wafer stack, which achieves a CE of 0.1%, a back-reflected seeded configuration has the potential to triple the CE, demonstrating the potential of seeded MC-THz generation.

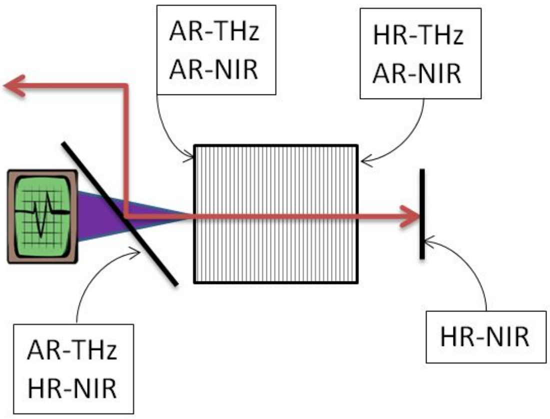

Figure 8.1: Modified back-reflected seeded configuration (see Fig. 7.17, for older version): AR-THz – terahertz anti-reflection; AR-NIR - near infrared anti-reflection; HR-THz – terahertz high reflective; HR-NIR – near infrared high reflective.

8.1 OUTLOOK: ROADMAP TOWARDS HIGH MC-THZ ENERGY USING HIGH EFFICIENCY SOURCES

Based on the world record achieved CE (see Section 5.4), a roadmap for the AXSIS project is developed, requiring 20 mJ of MC-THz at 0.3 THz for the electron accelerator [22]. Thus the driving optical laser with a two-line spectrum must be amplified to a pulse energy of $E_o \sim 4\,\text{J}$, assuming the demonstrated efficiency of 0.5% at 0.3 THz. For this given high energy laser with a Gaussian shape, the required laser radius waist (w_0) is $\sim 2.2\,\text{cm}$ (for $F_o = 2E_o/(\pi w_0^2)$, assuming $F_o = 500\,\text{mJ/cm}^2$). As a result of these considerations, a MgO:PPLN crystal with an aperture size of $\sim 7\,\text{cm}$ is required, assuming dia. $= \pi w_0$ [39].

Within the scope of the experimental results of this work, a less conservative estimate would be to assume that a seeded MC-THz configuration (see Fig. 8.1) might improve the efficiency by three times. Additionally, a spatial flat-top is implemented for the optical pump, which would also increase the efficiency [14]), but the efficiency increase will be neglected here. With these two assumptions, the driving optical laser with a two-line spectrum must be amplified to a pulse energy of $E_o \sim 1.33\,\mathrm{J}$, assuming an efficiency of $(0.5\times3)\%$ at 0.3 THz. For a spatial flat-top, the required laser diameter is 1.8 cm (for $F_o = 4E_o/(\pi d^2)$, assuming $F_o = 500\,\mathrm{mJ/cm^2}$). Note: The diameter d must be a little bigger to include the diffraction effects of the THz beam.

As a final outlook, a summary of CE improvements will be listed from both literature and using ideas experimentally explored from this work:

- Instead of a two-line spectrum, the pump spectrum and phase can be designed so that only down-conversion is preferred (see Ravi and Kärtner [32] and references within).
- Instead of periodically poled crystals, aperiodically poled crystals allow for modifications of the phase-matching as the pump pulse is red-shifted (see Ravi and Kärtner [32]).
- Improving the CE by THz seeding was experimentally investigated using a back-reflected configuration. In the example shown in this work, CE might be improved by three times compared to the unseeded configuration (Section 7.2.2).
- Compared to LN, KTP has good FOM values (Table 2.1). Although the KTP experimental results, in this work, were disappointing (Section 5.3.1), it might prove more efficient than LN under the corrected conditions (as discussed in Section 5.4).
- In Chapter 7, anti-reflection coated wafers were simple stacked. Optical-bonding of wafers [41] might be a superior method to stack wafers.
- Instead of the usual a Gaussian-shaped spatial pump beam. Flat tops are known to improve the conversion efficiency [14].

In summary, these achievements are an important next step for the realization of the next generation of THz-driven electron accelerators.

Part II

APPENDIX

A

APPENDIX

A.1 DAMAGE THRESHOLD

In order to determine the beam distortion effects in both LN and KTP crystals, a measurement was performed with the multiline laser at a repetition rate of 10 Hz and a pulse duration of 250 ps. The experimental setup is illustrated in Fig. A.1. The multiline laser beam was aligned through the crystal, which afterwards was sent into a CCD camera for long-term measurement. Another CCD camera was utilized to image the output surface of the crystal. In the first round of experiments, the influence of the crystal length on the beam distortion was investigated at cryogenic temperature (CT), for which lithium niobate (LN) bulk crystals with different lengths of 5, 10, 20, 40 mm were utilized. The laser peak fluence was fixed to $210\,\mathrm{mJ/cm^2}$ and the final beam profile was monitored for 45 minutes. The beam profiles for various crystals lengths are shown in Fig. A.2. The results demonstrate that the beam distortion after 45 min increases with the length of the crystal.

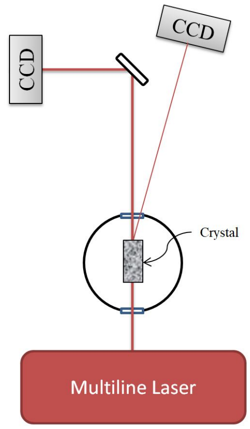

Figure A.1: The experimental setup for testing beam distortion effects for LN and KTP crystals using the multiline laser (experiment performed by Wenlong Tian and Giovanni Cirmi).

Length	**5mm**	**10mm**	**20mm**	**40mm**
$210mJ/cm^2$	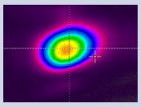	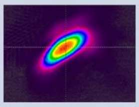	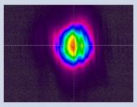	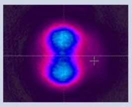

Figure A.2: The beam profiles in different length LN crystals recorded after 45 min at cryogenic temperature.

In the next round of experiments, 5 mm long LN and 6 mm KTP bulk crystals were used at RT and CT. The beam distortion profiles after 45 minutes are summarized in Fig. A.3.

	6 mm KTP	**5 mm LN**
RT	$> 1.6\, J/cm^2$ 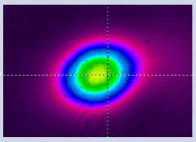	$> 1.4\, J/cm^2$ 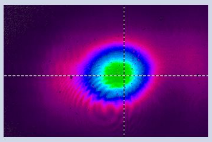
CT	$> 1.2\, J/cm^2$ 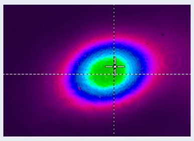	$< 0.42\, J/cm^2$ 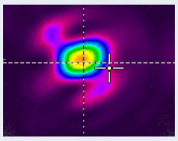

Figure A.3: The beam profiles in 5 mm LN crystal and 6 mm LN crystal recorded after 45 min at RT and CT.

The laser peak fluence was increased above 1.4 J/cm^2 in both crystals at RT, and no beam distortion observed in KTP. However, a significant beam distortion was observed in LN even below 0.42 J/cm^2 at CT. KTP can handle at least three times more laser peak fluence without observing any significant changes in the beam profile.

A.2 TERAHERTZ TIME DOMAIN SPECTROMETER

A commercial Terahertz time-domain spectrometer (THz-TDS) was utilized to characterize the terahertz properties, such as absorption and refractive index from various materials in the terahertz range from 0.2 to 2 THz.

Using the THz-TDS, the temperature dependent refractive index and absorption coefficient along the c-axis for a MgO:PPLN and a Rb:KTP are depicted in Fig. A.5 and Fig. A.5, respectively. The dimensions of the crystals were as following: 10.08×3.98×5.04 mm^3 for MgO:PPLN and 9.67×5.19×1.35 mm^3 for Rb:KTP.

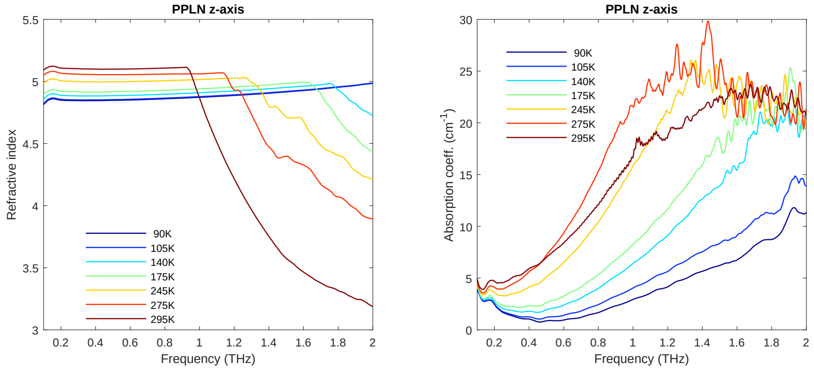

Figure A.4: The terahertz frequency dependent a) refractive index and b) absorption coefficient in MgO:PPLN at different temperatures (experiment performed by Elias Kueny).

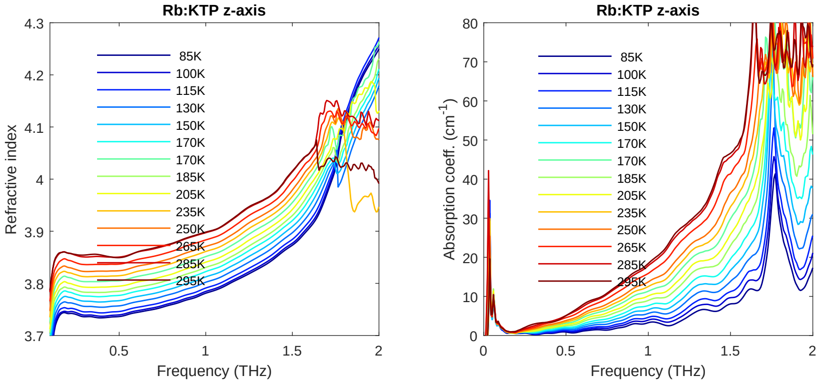

Figure A.5: The terahertz frequency dependent a) refractive index and b) absorption coefficient in Rb:KTP at different temperatures (experiment performed by Elias Kueny).

In addition, the terahertz losses in different materials, which were utilized in terahertz generation and detection, were characterized using the THz-TDS. As an example, the result obtained with a polyethylene shield is shown in Fig. A.6. The polyethylene shield was used to cover the THz-sensor during the THz generation experiment.

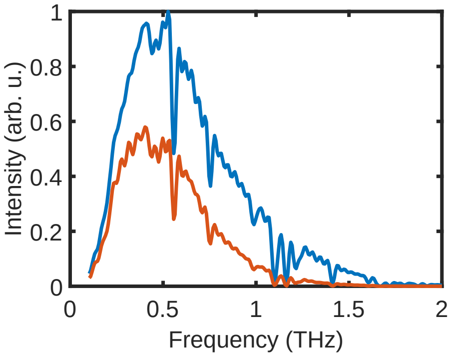

Figure A.6: THz-TDS with polyethylene: detected signal with (red) and without (blue) the polyethylene shield.

The ratio between the two curves in Fig. A.6 (signal with (red) vs. reference without polyethylene shield (blue)) gives the frequency-dependent losses for that specific material, including the Fresnel and absorption losses.

BIBLIOGRAPHY

[1] Robert Adair, LL Chase, and Stephen A Payne. "Nonlinear refractive index of optical crystals." In: *Physical Review B* 39.5 (1989), p. 3337.

[2] Frederike Ahr et al. "Narrowband terahertz generation with chirped-and-delayed laser pulses in periodically poled lithium niobate." In: *Optics Letters* 42.11 (2017), pp. 2118–2121. DOI: 10.1364/OL.42.002118. URL: http://ol.osa.org/abstract.cfm?URI=ol-42-11-2118.

[3] Cory Baumgarten, Michael Pedicone, Herman Bravo, Hanchen Wang, Liang Yin, Carmen S. Menoni, Jorge J. Rocca, and Brendan A. Reagan. "1 J, 0.5 kHz repetition rate picosecond laser." In: *Optics Letters* 41.14 (2016), pp. 3339–3342. DOI: 10.1364/OL.41.003339. URL: http://ol.osa.org/abstract.cfm?URI=ol-41-14-3339.

[4] J. D. Bierlein and C. B. Arweiler. "Electro-optic and dielectric properties of KTiOPO4." In: 49 (1986), pp. 917–919. ISSN: 0003-6951. DOI: 10.1063/1.97483.

[5] Robert W. Boyd. *Nonlinear Optics, Third Edition*. 3rd. USA: Academic Press, Inc., 2008. ISBN: 0123694701.

[6] Sergio Carbajo, Jan Schulte, Xiaojun Wu, Koustuban Ravi, Damian N. Schimpf, and Franz X. Kärtner. "Efficient narrowband terahertz generation in cryogenically cooled periodically poled lithium niobate." In: *Optics Letters* 40.24 (2015), pp. 5762–5765. DOI: 10.1364/OL.40.005762. URL: http://ol.osa.org/abstract.cfm?URI=ol-40-24-5762.

[7] Richard DeSalvo, Ali A Said, David J Hagan, Eric W Van Stryland, and Mansoor Sheik-Bahae. "Infrared to ultraviolet measurements of two-photon absorption and n/sub 2/in wide bandgap solids." In: *IEEE Journal of Quantum Electronics* 32.8 (1996), pp. 1324–1333.

[8] Umit Demirbas, Huseyin Cankaya, Yi Hua, Jelto Thesinga, Mikhail Pergament, and Franz X. Kärtner. "20-mJ, sub-ps pulses at up to 70 W average power from a cryogenic Yb:YLF regenerative amplifier." In: 28 (2020), p. 2466. ISSN: 1094-4087. DOI: 10.1364/oe.384968.

[9] Valentin G. Dmitriev, Gagik G. Gurzadyan, and David N. Nikogosyan. *Handbook of Nonlinear Optical Crystals*. 1999. DOI: 10.1007/978-3-540-46793-9.

[10] R. W. P. Drever, J. L. Hall, F. V. Kowalski, J. Hough, G. M. Ford, A. J. Munley, and H. Ward. "Laser phase and frequency stabilization using an optical resonator." In: 31 (1983), pp. 97–105. ISSN: 0721-7269. DOI: 10.1007/bf00702605.

[11] P. A. Franken, A. E. Hill, C. W. Peters, and G. Weinreich. "Generation of Optical Harmonics." In: 7 (), pp. 118–119. ISSN: 0031-9007. DOI: 10.1103/physrevlett.7.118.

[12] Y. Furukawa, K. Kitamura, A. Alexandrovski, R. K. Route, M. M. Fejer, and G. Foulon. “Green-induced infrared absorption in MgO doped LiNbO3.” In: 78 (2001), pp. 1970–1972. ISSN: 0003-6951. DOI: `10.1063/1.1359137`.

[13] Y. Furukawa, K. Kitamura, A. Alexandrovski, R. K. Route, M. M. Fejer, and G. Foulon. “Green-induced infrared absorption in MgO doped LiNbO3.” In: 78 (2001), pp. 1970–1972. ISSN: 0003-6951. DOI: `10.1063/1.1359137`.

[14] MJ Guardalben, J Keegan, LJ Waxer, V Bagnoud, IA Begishev, J Puth, and JD Zuegel. “Design of a highly stable, high-conversion-efficiency, optical parametric chirped-pulse amplification system with good beam quality.” In: *Optics express* 11.20 (2003), pp. 2511–2524.

[15] M. Hemmer, L. E. Zapata, Y. Hua, and F. X. Kärtner. *Addressing Spectral Narrowing in Cryogenic Yb:YAG: a 10 mJ Cryogenic Yb:YLF Regenerative Amplifier*. 2016. DOI: `10.1364/assl.2016.ath4a.3`.

[16] Matthias C Hoffmann and József András Fülöp. “Intense ultrashort terahertz pulses: generation and applications.” In: *Journal of Physics D: Applied Physics* 44.8 (2011), p. 083001. DOI: `10.1088/0022-3727/44/8/083001`. URL: `https://doi.org/10.1088%2F0022-3727%2F44%2F8%2F083001`.

[17] Y. Hua, G. Chang, F. X. Kärtner, and D. N. Schimpf. “Pre-chirp managed, core-pumped nonlinear PM fiber amplifier delivering sub-100-fs and high energy (10 nJ) pulses with low noise.” In: 26 (2018), p. 6427. ISSN: 1094-4087. DOI: `10.1364/oe.26.006427`.

[18] Yi Hua et al. “87-W 1018-nm Yb-fiber ultrafast seeding source for cryogenic Yb: yttrium lithium fluoride amplifier.” In: 43 (2018), p. 1686. ISSN: 0146-9592. DOI: `10.1364/ol.43.001686`.

[19] Hideki Ishizuki and Takunori Taira. “Improvement of laser-beam distortion in large-aperture PPMgLN device by using X-axis Czochralski-grown crystal.” In: *Optics express* 22.16 (2014), pp. 19668–19673.

[20] Hideki Ishizuki and Takunori Taira. “Improvement of laser-beam distortion in large-aperture PPMgLN device by using X-axis Czochralski-grown crystal.” In: 22 (2014), p. 19668. ISSN: 1094-4087. DOI: `10.1364/oe.22.019668`.

[21] Spencer W. Jolly, Nicholas H. Matlis, Frederike Ahr, Vincent Leroux, Timo Eichner, Anne-Laure Calendron, Hideki Ishizuki, Takunori Taira, Franz X. Kärtner, and Andreas R. Maier. “Spectral phase control of interfering chirped pulses for high-energy narrowband terahertz generation.” In: 10 (2019). ISSN: 2041-1723. DOI: `10.1038/s41467-019-10657-4`.

[22] Franz X Kaertner, Frederike Ahr, A-L Calendron, H Çankaya, S Carbajo, G Chang, G Cirmi, K Dörner, U Dorda, A Fallahi, et al. "AXSIS: Exploring the frontiers in attosecond X-ray science, imaging and spectroscopy." In: *Nuclear Instruments and Methods in Physics Research Section A: Accelerators, Spectrometers, Detectors and Associated Equipment* 829 (2016), pp. 24–29.

[23] F X Kärtner et al. "AXSIS: Exploring the frontiers in attosecond X-ray science, imaging and spectroscopy." In: *Nuclear instruments & methods in physics research. Section A, Accelerators, spectrometers, detectors and associated equipment* 829 (2016), pp. 24 –29.

[24] Kiyoshi Kato and Eiko Takaoka. "Sellmeier and thermo-optic dispersion formulas for KTP." In: 41 (2002), p. 5040. ISSN: 0003-6935. DOI: 10.1364/ao.41.005040.

[25] Sebastian Koke, Christian Grebing, Harald Frei, Alexandria Anderson, Andreas Assion, and Günter Steinmeyer. "Direct frequency comb synthesis with arbitrary offset and shot-noise-limited phase noise." In: 4 (2010), pp. 462–465. ISSN: 1749-4885. DOI: 10.1038/nphoton.2010.91.

[26] Y.-S. Lee, T. Meade, V. Perlin, H. Winful, T. B. Norris, and A. Galvanauskas. "Generation of narrow-band terahertz radiation via optical rectification of femtosecond pulses in periodically poled lithium niobate." In: 76 (2000), pp. 2505–2507. ISSN: 0003-6951. DOI: 10.1063/1.126390.

[27] Yun-Shik Lee, Timothy Meade, and Theodore B. Norris. "Tunable Narrowband Terahertz Generation From Periodically Poled Lithium Niobate." In: 12 (2001), p. 46. ISSN: 1047-6938. DOI: 10.1364/opn.12.12.000046.

[28] Theodore H Maiman. "Stimulated optical radiation in ruby." In: *nature* 187.4736 (1960), pp. 493–494.

[29] Alexander Mamrashev, Nazar Nikolaev, Valery Antsygin, Yury Andreev, Grigory Lanskii, and Arkady Meshalkin. "Optical Properties of KTP Crystals and Their Potential for Terahertz Generation." In: 8 (), p. 310. ISSN: 2073-4352. DOI: 10.3390/cryst8080310.

[30] JM Manley and HE Rowe. "Some general properties of nonlinear elements-Part I. General energy relations." In: *Proceedings of the IRE* 44.7 (1956), pp. 904–913.

[31] Emilio A Nanni, Wenqian R Huang, Kyung-Han Hong, Koustuban Ravi, Arya Fallahi, Gustavo Moriena, RJ Dwayne Miller, and Franz X Kärtner. "Terahertz-driven linear electron acceleration." In: *Nature communications* 6.1 (2015), pp. 1–8.

[32] Koustuban Ravi and Franz X. Kärtner. "Raman Shifting Induced by Cascaded Quadratic Nonlinearities for Terahertz Generation." In: (), p. 2000109. ISSN: 1863-8880. DOI: 10.1002/lpor.202000109.

[33] Koustuban Ravi and Franz X. Kärtner. "Terahertz-induced cascaded interactions between spectra offset by large frequencies." In: 27 (2019), p. 19254. ISSN: 1094-4087. DOI: 10.1364/oe.27.019254.

[34] Koustuban Ravi and Franz X. Kärtner. "Terahertz-induced cascaded interactions between spectra offset by large frequencies." In: 27 (2019), p. 19254. ISSN: 1094-4087. DOI: 10.1364/oe.27.019254.

[35] Koustuban Ravi, Damian N. Schimpf, and Franz X. Kärtner. "Pulse sequences for efficient multi-cycle terahertz generation in periodically poled lithium niobate." In: 24 (2016), p. 25582. ISSN: 1094-4087. DOI: 10.1364/oe.24.025582.

[36] Koustuban Ravi, Michael Hemmer, Giovanni Cirmi, Fabian Reichert, Damian N Schimpf, Oliver D Mücke, and Franz X Kärtner. "Cascaded parametric amplification for highly efficient terahertz generation." In: *Optics letters* 41.16 (2016), pp. 3806–3809.

[37] D. N. Schimpf, H. T. Olgun, A. Kalaydzhyan, Y. Hua, N. H. Matlis, and F. X. Kärtner. "Frequency-comb-based laser system producing stable optical beat pulses with picosecond durations suitable for high-precision multi-cycle terahertz-wave generation and rapid detection." In: *Optics Express* 27.8 (2019), pp. 11037–11056. DOI: 10.1364/OE.27.011037. URL: http://www.opticsexpress.org/abstract.cfm?URI=oe-27-8-11037.

[38] Jun ichi Shikata, Manabu Sato, Tetsuo Taniuchi, Hiromasa Ito, and Kodo Kawase. "Enhancement of terahertz-wave output from $LiNbO_3$ optical parametric oscillators by cryogenic cooling." In: 24 (1999), p. 202. ISSN: 0146-9592. DOI: 10.1364/ol.24.000202.

[39] A.E. Siegman. *Lasers*. University Science Books, 1986. ISBN: 9780685055953. URL: https://books.google.de/books?id=qBBaDQEACAAJ.

[40] Konstantin L. Vodopyanov. "Optical generation of narrow-band terahertz packets in periodically-inverted electro-optic crystals: conversion efficiency and optimal laser pulse format." In: 14 (2006), p. 2263. ISSN: 1094-4087. DOI: 10.1364/oe.14.002263.

[41] Konstantin L Vodopyanov. "Optical THz-wave generation with periodically-inverted GaAs." In: *Laser & Photonics Reviews* 2.1-2 (2008), pp. 11–25.

[42] Lu Wang, Arya Fallahi, Koustuban Ravi, and Franz Kärtner. "High efficiency terahertz generation in a multi-stage system." In: *Optics express* 26.23 (2018), pp. 29744–29768.

[43] A. S. Weling, B. B. Hu, N. M. Froberg, and D. H. Auston. "Generation of tunable narrow-band THz radiation from large aperture photoconducting antennas." In: 64 (1994), pp. 137–139. ISSN: 0003-6951. DOI: 10.1063/1.111543.

[44] Liang Jie Wong, Arya Fallahi, and Franz X Kärtner. "Compact electron acceleration and bunch compression in THz waveguides." In: *Optics express* 21.8 (2013), pp. 9792–9806.

[45] Ming-Hsiung Wu, Yu-Chung Chiu, Tsong-Dong Wang, Gang Zhao, Andrius Zukauskas, Fredrik Laurell, and Yen-Chieh Huang. "Terahertz parametric generation and amplification from potassium titanyl phosphate in comparison with lithium niobate and lithium tantalate." In: 24 (2016), p. 25964. ISSN: 1094-4087. DOI: 10.1364/oe.24.025964.

[46] Xiaojun Wu, Chun Zhou, Wenqian Ronny Huang, Frederike Ahr, and Franz X. Kärtner. "Temperature dependent refractive index and absorption coefficient of congruent lithium niobate crystals in the terahertz range." In: 23 (2015), p. 29729. ISSN: 1094-4087. DOI: 10.1364/oe.23.029729.

[47] Xiaowei Wu, Jiaru Shi, Huaibi Chen, Jiahang Shao, Tetsuo Abe, Toshiyasu Higo, Shuji Matsumoto, and Walter Wuensch. "High-gradient breakdown studies of an X -band Compact Linear Collider prototype structure." In: 20 (). ISSN: 2469-9888. DOI: 10.1103/physrevaccelbeams.20.052001.

[48] M. Yamada, N. Nada, M. Saitoh, and K. Watanabe. "First-order quasiphase matched LiNbO3waveguide periodically poled by applying an external field for efficient blue second-harmonic generation." In: 62 (1993), pp. 435–436. ISSN: 0003-6951. DOI: 10.1063/1.108925.

[49] Fei Yang, Lijuan Huang, Xiaoyu Zhao, Ling Huang, Daojiang Gao, Jian Bi, Xin Wang, and Guohong Zou. "An energy band engineering design to enlarge the band gap of KTiOPO 4 (KTP)-type sulfates via aliovalent substitution." In: *Journal of Materials Chemistry C* 7.26 (2019), pp. 8131–8138.

[50] Amnon. Yariv. *Quantum electronics*. eng. 3rd ed. New York: Wiley. ISBN: 0471617717.

[51] David E Zelmon, David L Small, and Dieter Jundt. "Infrared corrected Sellmeier coefficients for congruently grown lithium niobate and 5 mol.% magnesium oxide–doped lithium niobate." In: *JOSA B* 14.12 (1997), pp. 3319–3322.

[52] Dongfang Zhang, Moein Fakhari, Huseyin Cankaya, Anne-Laure Calendron, Nicholas H. Matlis, and Franz X. Kärtner. "Cascaded Multicycle Terahertz-Driven Ultrafast Electron Acceleration and Manipulation." In: *Physical Review X* 10.1 (2020). ISSN: 2160-3308. DOI: 10.1103/physrevx.10.011067. URL: http://dx.doi.org/10.1103/PhysRevX.10.011067.

[53] Gi-Guo Zhong. "Measurement of optically induced refractive-index damage of lithium niobate doped with different concentrations of MgO." In: *Proceeding of the 11th International Quantum Electronics Conference (Institute of Electrical and Electronics Engineers, New York, 1980)*. 1980.